

NUCLEAR SPECTROSCOPY STUDIES OF ^{82}Sr

BY

PENELOPE SKORDAS HASKINS

A DISSERTATION PRESENTED TO THE GRADUATE SCHOOL
OF THE UNIVERSITY OF FLORIDA IN
PARTIAL FULFILLMENT OF THE REQUIREMENTS
FOR THE DEGREE OF DOCTOR OF PHILOSOPHY

UNIVERSITY OF FLORIDA

1984

Dedication

To Bernie, Jennifer and Stephanie

ACKNOWLEDGEMENTS

I would like to express my deepest appreciation to my cochairman Dr. A. C. Rester who provided me the opportunity to fulfill my dream and become a nuclear physicist. Without his leadership, guidance and encouragement it would not have been possible.

I am grateful to my chairman, Dr. F. E. Dunnam for his encouragement and for managing to smooth the path when I needed help. The careful attention that he and Dr. Rester gave to my dissertation enabled me to do a much better job than I could have done without their help.

Special thanks are due to Dr. R. B. Piercey for having the patience to answer so many of my questions and for sharing his enthusiasm for experimental nuclear physics.

The contributions of Dr. R. L. Coldwell to this work are many. The spectral analysis was done under his guidance using computer programs which he wrote specifically for this project. I have learned a great deal from him about numbers and statistics, but most of all, I have learned patience and an attitude towards computers that should be invaluable. His time, efforts, patience and good humor have been greatly appreciated.

My thanks go to Dr. M. L. Muga for the encouragement and help he has given as a member of my committee and a member of our team.

Dr. J. D. Fox and his staff at the Nuclear Lab at Florida State University have been a great help during our experiments. My thanks are

due Dr. Fox for providing us whatever support we needed to get the job done. His commitment to the success of our project is greatly appreciated. Special thanks go to Dr. A. D. Frawley for his wizardry with the Tandem. He is responsible for the 80 MeV ^{16}O beam that finally gave us the statistics we needed for the coincidence experiment on which so much of our results are based. Additional thanks are due to the graduate students at Florida State University who gave so much of their time and energy to our project, especially Dr. C. B. Saw.

I would like to thank Dr. A. V. Ramayya for the use of the polarimeter belonging to Vanderbilt University. The assistance of Dr. S. Robinson, Dr. M. A. Herath-Banda, and W. A. Ma with the polarization experiment was appreciated.

Both my typist, Sharon Bullivant, and my illustrator, Katarzyna Piercey, exhibited great patience and good humor throughout the many changes and revisions I required. It was a pleasure to work with both of them. They both did an excellent job!

And last, but by no means least, I am grateful to my family for their patience and endurance through the past eight years.

This work was supported in part by the U.S. Department of Energy under Contract No. DE-FG05-84ER40149. However, the opinions, findings, conclusions or recommendations expressed herein are those of the author and do not necessarily reflect the views of DOE.

TABLE OF CONTENTS

	Page
ACKNOWLEDGEMENTS.....	111
LIST OF TABLES.....	vi
LIST OF FIGURES.....	vii
ABSTRACT	x
CHAPTER	
I. INTRODUCTION.....	1
II. EXPERIMENTAL METHODS.....	7
Excitation Functions.....	7
Coincidence Experiment.....	9
Determination of Spins and Parities.....	15
Polarization.....	32
Data Analysis.....	52
III. NUCLEAR MODELS.....	66
The Shell Model.....	68
Nilsson Model.....	73
Collective Models.....	74
Quasiparticles.....	105
IV. RESULTS AND DISCUSSION.....	112
Level Scheme.....	112
Two-Quasiparticle-Plus-Rotor Calculations.....	127
Positive Parity Band.....	134
Negative Parity Band.....	145
Systematics.....	156
Unidentified Nucleus.....	167
V. SUMMARY.....	169
BIBLIOGRAPHY.....	173
BIOGRAPHICAL SKETCH.....	177

LIST OF TABLES

TABLE	Page
II-1. Coincidence Chart.....	20
II-2. Results of the Angular Distribution (12).....	33
II-3. Additional Angular Distribution Results.....	34
II-4. Properties of the Individual Germanium Detectors in the Polarimeter.....	39
II-5. Results of the Polarization Experiment.....	49
II-6. Energies and Relative Intensities of the Gamma-Rays in ^{82}Sr	58
II-7. Energy Sums.....	61
II-8. Comparison of Level Energies to Previously Reported Data.....	64
III-1. Comparison of Vibrational Model Predictions to ^{82}Sr Experimental Data.....	79
III-2. Experimental and Theoretical Energies of the Ground State Band of ^{82}Sr for a Generalized VMI Model.....	94
III-3. Comparison of the Predictions of the Asymmetric Rotor Model to ^{82}Sr Data.....	98
IV-1. Parameters Used to Calculate Nilsson Levels.....	128
IV-2. Nilsson Configurations Chosen for the Basis States of Negative Parity.....	128
IV-3. Energies and Intensities of Transitions in the Negative Parity Band.....	146
IV-4. Parameters from VMI Fit to Sr Nuclei.....	164

LIST OF FIGURES

FIGURES		Page
1-1	Decay of the compound nucleus.....	3
2-1	Excitation function.....	8
2-2	Singles spectrum: $^{70}\text{Ge}(^{16}\text{O}, \text{pxn})$ with $E_{\text{Beam}} = 68 \text{ MeV}$...10	
2-3	Coincidence geometry.....	12
2-4	Electronic setup for coincidence experiment.....	13
2-5	Coincidence gates set on members of the ground state band.....	16
2-6	Sum-projected spectrum at 90°	18
2-7	Alignment of angular momenta in the compound nucleus (10).....	19
2-8	Dependence of $\alpha_\lambda(J)$ on the distribution parameter σ/J	27
2-9	Experimental α_2 's vs. spin.....	29
2-10	Experimental α_2 's vs. level energy.....	30
2-11	Experimental setup for angular distribution measurements (12).....	31
2-12	Geometry of the scattering process (10).....	37
2-13	Experimental setup for polarization experiment.....	41
2-14	Electronics configuration for polarization experiment...42	
2-15	"Dip" in spectrum taken by detector pair CD.....	44
2-16	511 keV peak in detector pair AC (a) and CD (b).....	45
2-17	Asymmetry ratios between perpendicular and parallel detector pairs; (a) uncorrected and (b) corrected.....	47
2-18	Determination of polarization efficiency with the polarization at (a) 29.7 cm. and (b) 15.2 cm from the target.....	49

2-19	Examples of output of fitting code RLCFIT. Along the bottom the dots represent the data and the solid lines the fit. At the top the dots represent the weighted difference between the fit and the data.....	54
3-1	Comparison of ^{82}Sr experimental levels to shell model calculations by Kitching et al. (34).....	70
3-2	Comparison of experimental levels in ^{86}Sr , ^{84}Sr , ^{82}Sr and ^{80}Sr to shell model calculations by Ogawa (35).	72
3-3	Comparison of predicted vibrational model levels for ^{82}Sr to experimental levels classified according to band structure (levels in beta band are taken from reference 20).....	80
3-4	Angular momentum projection for an axially symmetric rotor.....	81
3-5	Even parity vibrations in an even-even nucleus (40)....	83
3-6	Potential energy surfaces (40).....	84
3-7	Comparison of predicted rotational model energy levels for ^{82}Sr to the experimental levels.....	86
3-8	Moment of inertia vs. angular frequency for some simple nuclear models.....	89
3-9	Moment of inertia vs. angular frequency for the bands in ^{82}Sr	90
3-10	Graphical solution for γ and μ in ^{82}Sr based on the asymmetric rotor model.....	97
3-11	Comparison of IBM-I predictions to ^{82}Sr levels (27).....	101
3-12	Comparison of IBM-II predictions to ^{82}Sr levels (20).....	103
3-13	Comparison of IBM-II predictions to ^{82}Sr levels (28).....	104
3-14	Placement of particles in the $g_{9/2}$ orbital of a doubly even nucleus (2).....	106
3-15	Coupling of angular momenta for the two-quasiparticle-plus-rotor system (2).....	109
4-1	Level scheme for ^{82}Sr	113
4-2	Energy vs. spin for ^{82}Sr	114
4-3	χ^2 Calculations for the 522.1 keV transition.....	122

4-4	χ^2 Calculations for the 1296.2 keV transition.....	123
4-5	Nilsson levels for protons in ^{82}Sr	129
4-6	Nilsson levels for neutrons in ^{82}Sr	130
4-7	Two-quasiparticle-plus-rotor calculation results for ^{82}Sr	133
4-8	Positive parity band in ^{82}Sr	136
4-9	Kinematic moment of inertia for (a) ^{82}Sr and (b) ^{84}Zr	139
4-10	Aligned angular momentum for (a) ^{82}Sr and (b) ^{84}Zr	140
4-11	Absolute value of the interaction matrix element $V_{g-s}(5)$	142
4-12	Moment of inertia for the positive parity quasiparticle band in ^{82}Sr	144
4-13	Alternative placements of the 522 keV transition.....	148
4-14	Summed ground-state band gates at 0° and 90°	149
4-15	Ratio of the intensities of the gamma rays at 0° to 90°	150
4-16	$A_2 - A_4$ plane for transitions feeding a state with spin $I = 11$	152
4-17	Attenuation coefficient vs. spin for the negative parity band from (a) Haskins and (b) Dewald (23).....	153
4-18	Negative parity bands of the $N = 44$ isotones.....	155
4-19	Ground-state bands of the $N = 44$ isotones.....	157
4-20	$R_I = E_I/E_2$ for $I = 4, 6, 8, 10$ in the $N = 44$ isotones.....	158
4-21	Positive parity bands of the $N = 44$ isotones.....	159
4-22	Moment of inertia plots for (a) ground-state bands and (b) positive parity bands in the $N = 44$ isotones...	160
4-23	Ground-state bands of the strontium isotopes.....	162
4-24	VMI fits to the ground-state band levels in the neutron deficient strontium isotopes.....	163
4-25	Potential energy surfaces for the strontium isotopes calculated with (a) IBM-II and (b) IBM-I (27).....	166
4-26	Band structure in an unidentified nucleus.....	168

Abstract of Dissertation Presented to the Graduate School
of the University of Florida in Partial Fulfillment of the
Requirements for the Degree of Doctor of Philosophy

NUCLEAR SPECTROSCOPY STUDIES OF ^{82}Sr

By

PENELOPE SKORDAS HASKINS

December, 1984

Chairman: F. E. Dunnam
Cochairman: A.C. Rester
Major Department: Physics

The region of atomic nuclei around $A \sim 80$ are of interest to those who study nuclear structure theory because of the wide range of structures that can be found in these nuclei. Many of these nuclei are transitional nuclei such as ^{82}Sr in which rotational, vibrational, and quasiparticle degrees of freedom interact. Extensive experimental data are required for comparison with theoretical predictions.

The present experiments were performed at Florida State University. An 80-MeV oxygen beam produced with the Super FN Tandem Van de Graaff accelerator was used to produce the reaction $^{70}\text{Ge} (^{16}\text{O}, 2p2n) ^{82}\text{Sr}$. Measurements were made of the excitation functions, angular distributions, gamma-gamma-time coincidences, and polarizations.

From these measurements six new levels were placed in the level scheme of ^{82}Sr at 2683.7, 3609.0, 4367.5, 5308.7, 6364.7, and 7827.8

keV. A new band based on the level at 3526.3 keV was identified. The sequence of γ -ray transitions decaying down the negative parity band was reordered to 522-1005-876-694 keV. The 5915 keV level was assigned a spin and parity of 12^- .

Comparison of the present results to nuclear models implies that at low excitation energies ^{82}Sr is a deformed triaxial nucleus but the excitations are primarily vibrational. At excitation energies above about 1.5 MeV the nucleus appears to be more rotational. Both a negative parity band and a positive parity band are attributed to quasiparticle excitations. The interaction of the positive parity quasiparticle band with the quasi-gamma band is particularly strong.

CHAPTER I INTRODUCTION

The problem of a complete theory of nuclear structure that explains all known behavior starting from first principles has not been solved. Basically it is an A-body problem of relativistic particles in an unknown potential. There are too many particles to treat individually, but there are too few for statistical treatments to be valid. The best that theorists have been able to achieve are models based on approximations. The success of these models is measured by how closely their predictions agree with experimental results. Many of the models are phenomenological; i.e., they fit empirical data. Microscopic models depend on assumptions of potentials and wave functions to calculate the properties of nuclei. Although the models do not provide a solution of the nuclear structure problem, they do increase our understanding of observed phenomena in nuclei.

Nuclei can be classified by their properties into three basic structural groups: spherical vibrators, strongly deformed rotators, and transitional nuclei. The latter group makes up about 85% of known nuclei; it is among these nuclei that structure theory is most interesting. The level schemes of transitional nuclei exhibit evidence of an interplay of several degrees of freedom such as collective rotational and vibrational excitations, single-particle excitations, and core deformation. At high angular momentum the collective motion of the nucleus is influenced by single-particle excitations. Rotational and

vibrational excitation modes are superimposed, making the interpretation of the experimental information a formidable challenge.

The early information on nuclear energy levels came from Coulomb excitation studies, radioactive decay, inelastic scattering and direct reactions. Not until in-beam spectroscopy of heavy ion reactions ($A > 4$) was used to study nuclei with high angular momentum could the properties of high spin states be determined. In a heavy ion fusion reaction the target and projectile form a compound nucleus which then decays along one of a number of possible pathways. For projectile energies slightly above the Coulomb barrier, the two most likely decay modes are fission and particle evaporation (1). In fission most of the angular momentum goes into the relative motion of the two fission fragments. Evaporated particles carry only small amounts of angular momentum (1 \hbar per neutron or proton), although alpha particles can carry larger amounts. When the excitation energy drops low enough, the nucleus emits gamma rays which then de-excite the nucleus to its ground state (see Figure 1-1). There are two distinct types of gamma rays emitted. The statistical gamma rays are dipole transitions which cool the nucleus carrying away little angular momentum (1). They decay towards the yrast line, which is the lowest energy state for a given angular momentum. The yrast-like gamma rays are more or less parallel to the yrast line and remove the angular momentum. The observed spectrum of gamma rays consists of a number of resolved gamma rays on a continuum of unresolved gamma rays which come from the higher energy levels with populations too small to be individually observed. The resolved lines are usually at or near the yrast line with spins up to 20-30 \hbar or more.

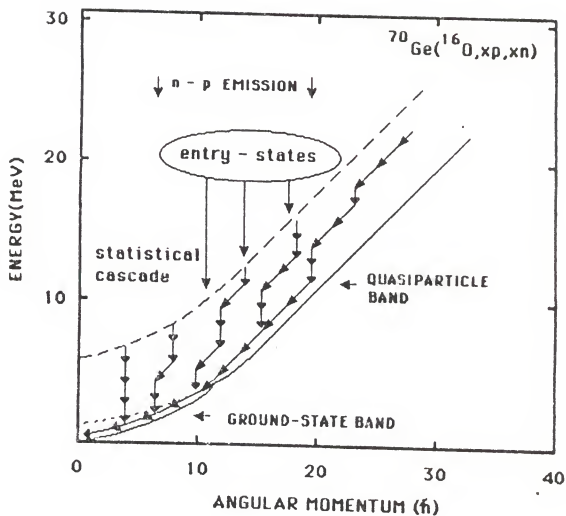


Figure 1-1. Decay of the compound nucleus.

In many nuclei gamma rays de-excite the nucleus in cascades that are referred to as bands. These bands consist of a set of levels at every, or every other, spin value whose energies vary smoothly with spin and which are interconnected by enhanced E2 transitions (2). A band is usually based on an intrinsic structure which remains essentially unchanged as angular momentum is added. In a rotational nucleus one sees three main types of bands. The ground state band is, for low spin, also the yrast band. It is a collective band built on the ground state configuration. The gamma band is based on an intrinsic structure which has oscillations away from axial symmetry. The beta band exhibits oscillations around an equilibrium shape while maintaining axial symmetry. In transitional nuclei one sees a quasi-gamma band and a quasi-beta band instead of the pure configurations seen in well-deformed nuclei. In these bands vibrational and rotational characteristics coexist (3). There are also negative parity bands, some of which are based on octupole vibrations and some of which are quasiparticle configurations.

Nuclear spectroscopy is a valuable tool for gathering information about nuclear structure. Some of the properties that can be measured are the energies, spins, and parities of the quantum states of a nucleus. The energy levels and band structure of a nucleus can be determined using coincidence techniques. Because a heavy ion fusion reaction orients the angular momenta of the residual nuclei in a plane perpendicular to the beam, the gamma rays are emitted with an anisotropy that is characteristic of their multipolarities. Measurement of the angular distributions enables one to establish those multipolarities. The relative parities of the levels can be established

with linear polarization measurements. The comparison of these properties with the predictions of nuclear structure theory increases our understanding of both the theory and behavior of the nucleus.

The neutron-deficient strontium nuclei have level schemes which indicate a systematic change in structure from spherical at $N=50$ to highly deformed at $N=40$ (4). Midway between these two extremes lies the nucleus ^{82}Sr . The level structure of ^{82}Sr is that of a transitional nucleus. There is evidence of rotational and vibrational behavior influenced by quasiparticle excitations. The ground state band appears to be primarily rotational. The first excited positive parity band has vibrational characteristics up to the $J=10^+$ state, indicating that it may be a quasi-gamma band. At that point its behavior can be interpreted either as the crossing of a two-quasiparticle band (5) or as the onset of rigid rotation (6). The negative parity band is identified with two-quasiparticle excitations. The highest level of that band seems to be completely aligned, indicating that it may be an entry level state. All of these phenomena imply that ^{82}Sr is a complex nucleus worthy of study.

The reaction used to study ^{82}Sr was $^{70}\text{Ge}(^{16}\text{O}, 2p2n)^{82}\text{Sr}$. The 80 MeV ^{16}O beam was produced by the Florida State University Tandem Van de Graaff accelerator. The measurements included excitation functions, angular distributions, γ - γ -t coincidences, and polarizations. The experimental methods, analysis techniques, and results are covered in Chapter 2. Chapter 3 is a review of nuclear structure theory as it applies to ^{82}Sr . This includes a review of the nuclear models which have been used by other authors in an attempt to explain the structure of ^{82}Sr as well as an overview of the models which are referred to in

the discussion of the experimental results. Some comparisons of the ^{82}Sr levels with theoretical predictions are made. Chapter 4 includes a discussion of the results and our interpretations. The results are summarized in Chapter 5.

CHAPTER II EXPERIMENTAL METHODS

The experiments were conducted on the Super FN Tandem Van de Graaff accelerator at Florida State University. The reaction used to study ^{82}Sr was $^{70}\text{Ge}(^{16}\text{O}, 2p2n)^{82}\text{Sr}$. The target consisted of $400\text{ }\mu\text{g}/\text{cm}^2$ of 98.5% enriched pure ^{70}Ge metal evaporated onto a Ta foil with a thickness of about $200\text{ mg}/\text{cm}^2$. The oxygen beam was produced in the inverted sputter source.

Excitation Functions

In a heavy ion fusion reaction, the target and projectile fuse to form a compound nucleus which decays in the order of 10^{-17} to 10^{-18} seconds. The exit channels are assumed to be independent of the mode of formation (1). The most likely decay processes are fission and evaporation of particles.

The cross section for production of the different residual nuclei varies with beam energy. Excitation functions are run in order to determine the optimum beam energy for study of a particular nucleus. For this study, excitation functions were run with ^{16}O beam energies of 60, 64, and 68 MeV, the maximum oxygen beam energy available on the tandem at the time. The results, shown in Figure 2-1, indicate an increasing cross section for ^{82}Sr with increasing energy.

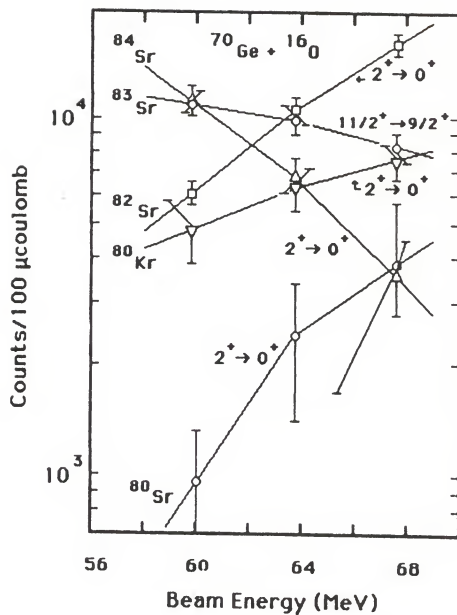


Figure 2-1. Excitation function.

Coincidence Experiment

The reaction, $^{70}\text{Ge}(^{16}\text{O}, \text{xpxn})$, produced several other residual nuclei besides ^{82}Sr . As a result, the singles spectrum for this reaction is very complex. (See Figure 2-2). When there are so many gamma rays, the peaks often overlap, making the resolution of the peaks of interest a difficult problem. In a singles spectrum there is no information on the time relationship of the gamma rays. The relationships between the gamma rays can be determined through the requirement that a gamma ray is counted only when it is detected within a set time of the detection of another gamma ray. The number of events thus counted is reduced, simplifying the spectrum considerably. A three-dimensional array is generated in energy (γ_1), energy (γ_2), and time. A slice, or gate, taken across this array yields information about the relationships of the various gamma rays and their relative intensities. This information can be used to build a level scheme which defines the excited energy levels and the band structure of a nucleus.

The γ - γ -t coincidence measurements were made at beam energies 68, 72, and 80 MeV. The results from the 80 MeV run have been used for the most part in the construction of the present level scheme. The detectors used in the 80 MeV run were 1) an ORTEC true coaxial Ge(Li) detector with 25.2% efficiency relative to that of a standard 3" x 3" NaI(Tl) detector and an energy resolution of 2.1 keV, and 2) a Princeton Gamma Tech (PGT) true coaxial detector with 18% efficiency relative to that of a standard 3" x 3" NaI(Tl) detector and an energy resolution of 2.5 keV. The ORTEC detector was placed at 90° to the beam direction and is referred to in the following section as A1. The PGT detector was

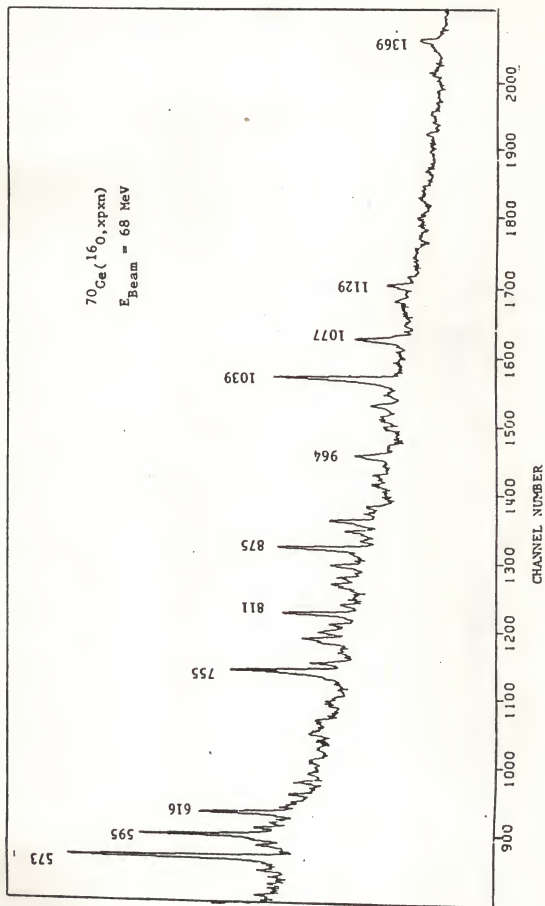


Figure 2-2. Singles spectrum: $^{70}\text{Ge}(^{16}\text{O}, \text{xpxn})$ with $E_{\text{beam}} = 68 \text{ MeV}$.

placed at 0° to the beam direction and is referred to as B1. The coincidence geometry is given in Figure 2-3.

Two gamma rays are said to be in coincidence if, when one is detected in one detector the other is detected in the other detector within a specified time interval. The determination of the coincidence relationship is made electronically. The electronic setup for the coincidence experiment is shown in Figure 2-4. A pulse is generated in detector A1 when a photon enters the detector. This pulse is amplified in the detector preamplifier and sent to both the spectroscopy amplifier (SA) and the timing filter amplifier (TFA). The SA shapes and amplifies the energy pulse and sends it to the analog-to-digital converter (ADC). The constant fraction discriminator (CFD) takes the amplified timing pulse from the TFA and creates two signals, one a delayed pulse, the other a reversed and attenuated pulse; these are added together to produce a fast negative timing pulse that is independent of the amplitude and risetime of the incoming pulse. The output of the CFD on the A1 side generates a start signal in the time-to-pulse-height converter (TPHC). The detection of a gamma ray in detector B1 results in the generation of a timing pulse on the B1 side that provides the stop signal for the TPHC.

The TPHC converts the time difference between the two pulses into a voltage pulse between 0 and 10 volts. The height of the pulse is proportional to the difference in time between the two events. If the height falls within the upper and lower limits set on the discriminators (ULD and LLD), an output is generated through the single channel analyzer (SCA). Since the SCA pulse occurs before the TPHC signal it can be used to generate the TPHC output. The timing coincidence peak is

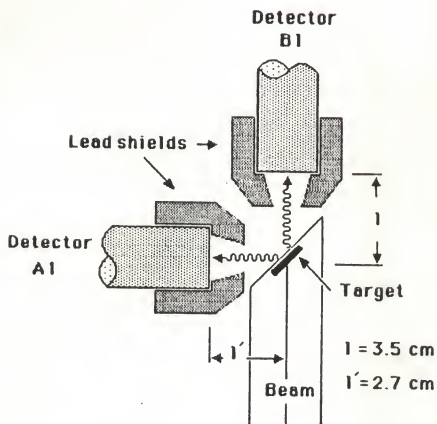


Figure 2-3. Coincidence geometry.

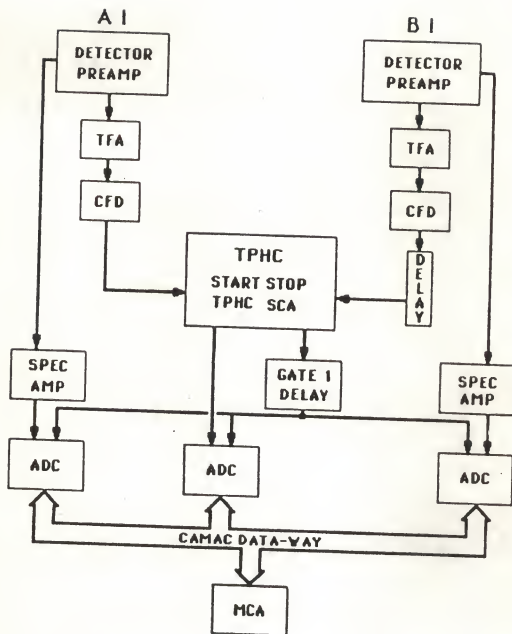


Figure 2-4. Electronic setup for coincidence experiment.

selected by the SCA. The TPHC generates an analog output pulse to its ADC if the stop signal follows the start signal within the chosen period of time. Since the actual lifetimes of the nuclear states of interest are on the order of picoseconds and the capabilities of the electronics are in the range of tens of nanoseconds, a delay line is placed in the stop circuit to delay the signals enough to be seen. The SCA signal is sent to a gate and delay generator (GDG) which sends the three ADC signals (energy,energy,time) to the multichannel analyzer (MCA) if they fall within the gate that is generated by the GDG. The MCA writes the multiparameter data to disk and that disk is periodically written to tape. The events were recorded in two 4096-channel spectra for the two energy signals and a 1024-channel spectrum for the timing signal.

The twenty-one data tapes were translated, compressed and written onto five 6250 BPI tapes and sorted at the University of Florida with the computer code, SORTA (7). Data accumulation accounting for about forty-eight hours of beam time resulted in fifty-five million recorded coincidence events. The background-subtracted gates were then analyzed with the program RCOLD (see the section on Data Analysis) and plotted using DRAW (8). Data manipulation, such as the addition and compression of gates, was accomplished with the FORTRAN program ASCI (9).

A coincidence gate is set by placing a window (2-6 channels, or about 1-3 keV) on a gamma ray peak in one energy spectrum and a time window (100 channels or about 80 nanoseconds) in the timing (TAC) spectrum. The remaining energy spectrum is searched for events that are in coincidence with the two windows. A second gate is set on an equally wide area of the background and this gate is subtracted from the first gate. Examples of background subtracted coincidence gates are shown in

Figure 2-5 for the ground state band. The sum-projected spectrum for Al (Figure 2-6) represents all of the gamma rays recorded in detector Al that are in coincidence with any gamma ray recorded in detector B1 and a 100-channel-wide timing (TAC) gate.

The coincidence measurement results are given in Table II-1. Gates were set on both the Al detector and the B1 detector. The relationships given are taken mainly from the Al gates. Gamma rays seen only in a B1 gate are noted with an asterisk. The underlined energies indicate strong peaks. Not all of the gamma rays identified as belonging to ^{82}Sr have been placed in the level scheme.

Determination of Spins and Parities

Statistical Model

Electromagnetic radiation is characterized not only by its energy but also by its multipolarity and its parity. In a heavy ion fusion reaction, the compound nucleus is oriented with its angular momentum vector in a plane perpendicular to the beam direction (see Figure 2-7(a)). The compound nuclear state can be considered to be completely aligned. The subsequent evaporation of particles (alphas, protons, and/or neutrons) does not affect this alignment very much because each particle carries away only 1-2 \hbar units of angular momentum in random directions compared to 20-25 \hbar for the total system. When the excitation energy is no longer high enough above the yrast line for the emission of particles, gamma rays are emitted. The lower spin levels (which are the ones observed) are preferentially fed from the continuum region because of their higher level densities (10).

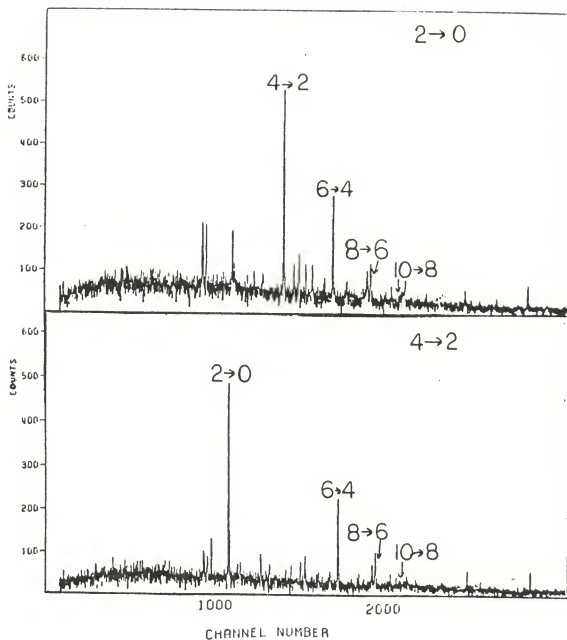
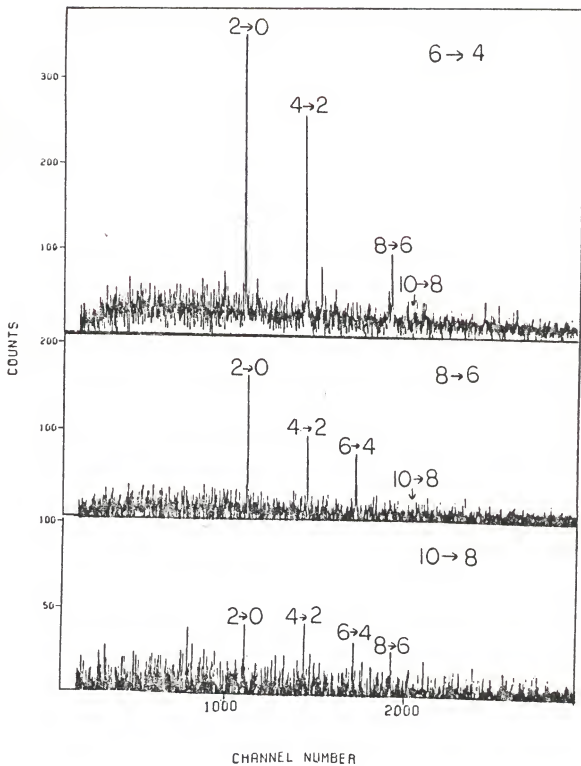


Figure 2-5. Coincidence gates set on members of the ground-state band.



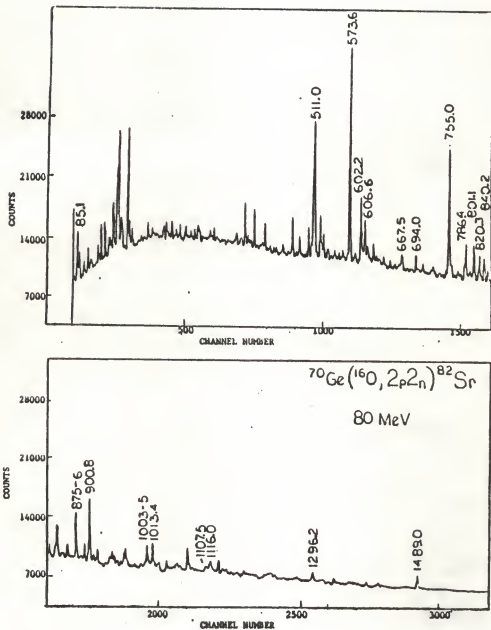
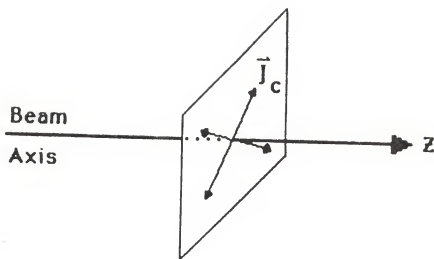
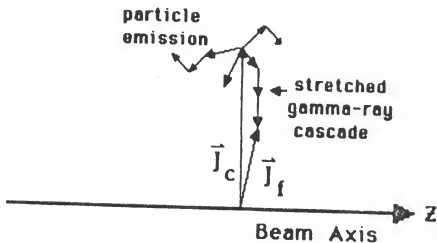


Figure 2-6. Sum-projected spectrum at 90° .



(a)



(b)

Figure 2-7. Alignment of angular momenta in the compound nucleus (10). The angular momentum of the compound nucleus is perpendicular to the beam axis (a). Particles carry away angular momenta in random directions. The gamma-ray emission occurs in stretched cascades, leaving the residual nucleus with alignment that is close to that of the compound nucleus (b).

TABLE II-1
Coincidence Chart

Gate	Coincidences
85.3	511.0, 573.6, 755.0, 900.8
261.8	423.5, 513.7, 522.1, 793.8, 941.3, 962., 1056.0, 1115.8, 1135.5
269.0	269.0, 381., 423.5, 439.9, 573.6, 755.0, 1489.0
403.9	<u>423.5</u> , <u>511.0</u> , <u>537.0</u> , 569.6, <u>573.6</u> , 596.8, 755.0, 786.2, 801.1, 820.2, 841.3, <u>876.0</u> , 900.8, 1107.5, <u>1163.7</u> , 1219.0, 1551.0
415.1	406.5, 573.6, 755.0, 667.5
423.5	261.8, 269.0, <u>403.9</u> , <u>511.0</u> , 537.0, 573.6, 602.2, 755.0, 786.4, 841.3, <u>876.0</u> , <u>1005.4</u> , <u>1163.7</u> , 1230.0
439.9	269.0, 511.0, 513.7, 573.6, 755.0, 841.3, 941.3, 1135.5
443.3	<u>511.0</u> , <u>573.6</u> , <u>840.2</u> , <u>900.8</u> , <u>1013.4</u>
511.0	85.3, 129., 147., 156.9, 183., 472., <u>511.</u> , <u>573.6</u> , 595., 602.2, <u>617.</u> , <u>688.6</u> , 712.4, <u>755.0</u> , 776.8, <u>875.7</u> , 900.8, 1039., <u>1077.</u> , 1113., 1129., 1828.4 (w)
513.7	261.8, 403.9, 415.1(w), 423.5, <u>511.0</u> , <u>573.6</u> , 602.2, 712.4, 837.4(w), 1013.4, 1116.9, 1135.5(w)
522.1	224., 261.5, 351.2, 403.9, 415.1, 511.0, <u>573.6</u> , 602.2, <u>694.0</u> , <u>755.0</u> , 758.8, 837.4, <u>876.0</u> , 941.3, 1005.4, 1056.0, <u>1135.5</u> , <u>1489.0</u>
534.1	403.9, 423.5, 511.0, 573.6, <u>841.3*</u> , 876.0
537.0	403.9, 423.5, 511.0, 573.6, 736.1, 755.0, 1196.6
573.6	85.3, 269.0, 443.3(w), <u>511.0</u> , <u>522.1</u> , 569.6*, <u>602.2</u> , 606.6, 667.5, 694.0, <u>755.0</u> , 758.8, 786.4, <u>801.1</u> , <u>820.2</u> , <u>840.2</u> , 876.0, <u>900.8</u> , <u>941.3</u> , 1003.3, <u>1005.4</u> , <u>1013.4</u> , 1059.1, 1085.9*, 1107.5, 1115-1117, 1135.5*, 1296.2, 1393.5, 1489.0, 1551.0, 1828.4(w)
583.1	156.9, 261.8, 406.5, <u>511.0</u> , <u>573.6</u> , <u>755.0</u>

Table II-1 continued

Gate	Coincidences
596.8	156.9, 439.9, 443.3, <u>511.0</u> , <u>573.6</u> , 755.0
602.2	261.8, 403.9*, 439.9, <u>511-512</u> , 521.4*, 537.0, <u>573.6</u> , 583.1*, <u>786.4</u> , <u>801.1</u> , <u>820.2</u> , 837.4, <u>840.2</u> , 1003.3, 1116.9, 1135.5, 1281.5
606.6	511.0, <u>573.6</u> , <u>755.0</u> , <u>786.4</u> , <u>801.1</u> , <u>900.8</u> , 941.3, 1116.9, 1283.9
667.5	573.6, <u>755.0</u> , 786.4, 801.1, 840.2, 1003.3
694.0	291., 406.5(w), 415.1(w), 513.7, <u>522.1</u> , <u>573.6</u> , 602.2, 755.0, 837.4(w), 841.3*, <u>876.0</u> , <u>1005.4</u> , <u>1489.0</u>
755.0	<u>500.8(c)</u> , <u>511.0</u> , <u>522.1</u> , <u>573.6</u> , 606.6, 667.5, <u>694.0</u> , 758.8, <u>786.4</u> , 801.1, 837.4, <u>840.2</u> , <u>876.0</u> , <u>900.8</u> , <u>941.3</u> , <u>962.2(c)</u> , <u>1003-1005</u> , <u>1013.4</u> , <u>1059.1</u> , 1085.9, 1107.5, <u>1116.9</u> , <u>1296.2</u> , 1336.5, 1393.5, <u>1489.0</u>
758.8	261.6, 269.7, 403.9, 522.1, 573.6, 755.0, 837.4, 900.8, 941.3, 1056.0
786.4	<u>511.</u> , <u>573.6</u> , <u>602.2</u> , 606.6, 667.5, 755.0, <u>801.1</u> , <u>820.2</u> , <u>840.2</u> , <u>900.8</u> , <u>1003.3</u> , 1115-1117, 1175.6, 1336.5
801.1	403.9, 511.0*, <u>573.6</u> , 602.1, 606.6, 667.5, <u>755.0</u> , 758.8*, <u>786.4</u> , <u>820.2</u> , <u>840.2</u> , <u>900.8</u> , <u>1003.3</u> , 1116.9, 1283.9(w), 1393.5
802.90	403.9, <u>511.0</u> , 522.1, <u>573.6</u> , 596.8, 602.2, <u>755.0</u> , 786.4, 840.2, 900.8, 1003-1005, 1085.9, 1296.2*
820.2	406.5, 415.1, 511.0, 537.0, <u>573.6</u> , <u>602.2</u> , 616.9(a), <u>786.4</u> , <u>801.1</u> , <u>840.2</u> , 956.7(a), <u>1003.3</u> , 1018.2(a), 1175.6
837.4	310.0, 403.9, 409.0, 415.1, 439.9*, 513.7, 522.1, <u>573.6</u> , <u>602.2</u> , 694.0, 758.8, 801-803, 900.8, 1115.8, 1175.6(w)
840.2	511.0(B), <u>573.6</u> , <u>602.2</u> , 667.5, <u>755.0</u> , <u>786.4</u> , <u>801.1</u> , <u>820.2</u> , 941.3, <u>1003.3</u> , 1116.9, 1283.9, 1296.2
841.3	511.0, 522.1, 534.1, <u>573.6</u> , <u>602.2</u> , 667.5, <u>755.0</u> , <u>786.4</u> , <u>801.1</u> , <u>820.2</u> , 840.2, <u>901.1</u> , <u>941.3</u> , <u>1003.3</u> , 1056.0, 1175.7, <u>1296.2</u>
876.0	269.0(w), 403.9, 423.5, <u>511.0</u> , 522.1, 528.2(b), <u>573.6</u> , 583.1, <u>694.0</u> , <u>755.0</u> , <u>802.9</u> , 900.8, 1005.4, <u>1077.6(b)</u> , 1129.(b), 1281.1(w), 1489.0

Table II-1 continued

Gate	Coincidences
900.8	380.0, 443.3, 511.0, <u>573.6</u> , 606.7, <u>755.0</u> , <u>801.1</u> , 876.0 941.3, 1003-1005, <u>1013.4</u> , 1059.1, 1085.9, <u>1116.9</u> , 1181.0(w), 1296.2, <u>1336.5</u> , 1393.5(w)
941.3	269.0, 443.3(w), 522.1, <u>573.6</u> , 667.5, <u>755.0</u> , 840-842, 900.8, 1013.4*, 1056.0, <u>1059.1</u> , 1085.9*, <u>1296.2(w)</u> , 1336.5, 1489.0*
951.1	350.7, <u>370.0</u> , 513.7, <u>573.6</u> , 617.0, 694.0, <u>755.0</u> , <u>782.6</u> , <u>837.4</u> , 882.0, <u>900.8</u> , 941.3, <u>1052.0</u> , 1088.0, <u>1163.7</u> , 1268.7
1003.3	380.0(w), <u>511.0</u> , 522.1(w), <u>573.6</u> , 602.2, 606.7, 667.5*, 694.0, <u>755.0</u> , <u>786.4</u> , <u>801.1</u> , <u>802.9</u> , <u>840.2</u> , 876.0, <u>900.8</u> , 1116.9, <u>1175.6(w)</u> , <u>1181.0(w)</u> , 1283.9*(w)
1005.2	415.1, <u>522.1</u> , <u>573.6</u> , 602.2, 667.5, 694.0, <u>755.0</u> , 786.4, 801.1, 840.2, <u>900.8</u> , 1489.0
1013.4	443.3, 511.0*, 537.0, <u>573.6</u> , <u>755.0</u> , 802.9, 843.4, <u>900.8</u> , 962.2, 1005.4, 1087.5, 1181.0, 1107.5, 1116.9, <u>1144.2</u>
1059.1	234., 368., 511.0, 537.0, 573.6, 617.0, 712.4, 755.0, 758.8, 900.8, 941.3, 1052.0, 1489.0
1085.9	511.0, 573.6(w), 583.1, 602.2, 755.0, 900.8, 941.3, 1003.3, 1013.4, 1087.0, 1131.
1107.5	<u>403.9</u> , 511.0*, <u>573.6</u> , <u>755.0</u> , <u>900.8</u> , 1013.4, 1114.5
1115.8	261.8, 269.0, 406.5, 415.1, 423.5, <u>573.6</u> , 606.6, 712.4, 801.1, 837.4, 840.2, 876.0, 900.8, <u>945.0</u> , 1003.3, 1039., 1107.5, 1116.9
1116.9	423.5, <u>573.6</u> , 596.8, 602.2, 606.7, <u>755.0</u> , <u>786.4</u> , <u>801.1</u> , <u>820.2</u> , <u>840.2</u> , <u>900.8</u> , 1003.3, 1013.4, 1115.8, 1175.6, <u>1283.9(w)</u>
1135.5	261.8(w), 381., 439.9, 513.7, 569.6, 573.6, 602.2, 841.3
1163.7	403.9, 423.5, 573.6
1175.6	291.5, 572.2, 755.9, 801.1, 820.2, 840.2, 945.0
1268.7	537.0, 573.6, 670.4, 718.2, 786.4, 801.1, 820.2, 837.4, 841.3, 1003.3, 1056., 1116.9, 1152.2
1283.9	573.6, 694.0, 786.4, 801.1, 837.4, 876.0, 962.2, 1003.3, 1116.9, 1175.6
1296.2	403.9, 423.5*, 443.3, 511.0*, <u>573.6</u> , 608.3*, <u>755.0</u> , 801.1*, <u>841.3</u> , <u>900.8</u> , <u>941.3</u> , 1056.0

Table II-1 continued

Gate	Coincidences
1336.5	511.0*, <u>573.6</u> , 667.5, <u>755.0</u> , 801.1, 882., <u>900.8</u> , 941.3, 962.2
1393.5	573.6, 755.0, 841.3, 900.8
1489.0	269., 443.3, <u>522.1</u> , <u>573.6</u> , <u>694.0</u> , <u>755.0</u> , 876.0*, 941.3, 1005.4. 1059., 1085.9
1828.4	573.6
(a) ⁸⁰ Kr	
(b) ⁸³ Sr	
(c) ⁷⁹ Rb	
(w) Weak peak	
* indicates γ seen only at 0°	

This causes stretched cascades with $J_f = J_i - \lambda$ (λ being the multipolarity of the gamma ray). For stretched cascades J_f , J_i and λ all lie in the plane perpendicular to the beam axis and thus the initial alignment is largely maintained (see Figure 2-7(b)). If the beam axis is the quantization axis, z , then the projection of the angular momentum vectors for this process is

$$M_i = M_f = m = 0. \quad (2.1)$$

This orientation enables one to determine the multipolarity of the emitted gamma rays through the measurement of the angular distribution of their intensities. If the angular momentum vectors were randomly oriented the angular distribution of the gamma rays would be isotropic. The following treatment of the statistical model is based on the presentation given in references 10 and 11.

The probability of a nucleus being in a state of angular momentum \vec{J} with projection m on the quantization axis (the beam direction) is given by the population parameter, $P(m)$. If one assumes that the possible m -values have a Gaussian distribution centered on $m=0$, then $P(m)$ takes on the form

$$P(m) = \frac{e^{-m^2/2\sigma^2}}{\sum_{m_i=-j}^j e^{-m_i^2/2\sigma^2}} \quad (2.2)$$

An alternative representation of the population of a given state is given by the statistical tensor, $\rho_k(J)$ which is related to $P(m)$ by

$$\rho_k(J) = \sqrt{2J+1} \sum_m (-)^{J-m} \langle JmJ-m | k0 \rangle P(m) \quad (2.3)$$

where $k = 0, 1, 2, \dots, 2J$.

For a pure multipole radiation of multipolarity, λ , the angular distribution can be written as

$$W(\theta) = \sum_k \rho_k(J) F_k(J_f \lambda J_i) P_k(\cos \theta) \quad (2.4)$$

where

$$F_k(J_f \lambda J_i) = (-1)^{1+J_i-J_f} \sqrt{2J_i+1} (2\lambda+1) \langle \lambda_1 \lambda_2 -1 | k_0 \rangle W(J_i J_i \lambda_1 \lambda_2; k J_f) \quad (2.5)$$

and $W(\theta)$ is normalized so that

$$\rho_0 = F_0 = P_0 = 1. \quad (2.6)$$

For mixed multipole radiation, the mixing ratio, δ , must be taken into account. It is expressed as

$$\delta = \frac{\langle J_f || \lambda_2 || J_i \rangle}{\langle J_f || \lambda_1 || J_i \rangle} = \frac{\text{intensity of } \lambda_2}{\text{intensity of } \lambda_1} \quad (2.7)$$

where the sign depends on the relative phase of the two reduced matrix elements (10). In this case the A_k are expressed as

$$A_k(J_i \lambda_1 \lambda_2 J_f) = \rho_k(J_i) \frac{1}{1+\delta^2} [F_k(J_f \lambda_1 \lambda_1 J_i) + 2\delta F(J_f \lambda_1 \lambda_2 J_i) + \delta^2 F_k(J_f \lambda_2 \lambda_2 J_i)]. \quad (2.8)$$

For complete alignment, the $\rho(J)$ are equal to

$$B_k(J) = \sqrt{2J+1} (-)^J \langle J0J0 | k0 \rangle \text{ for integer spin} \quad (2.9)$$

and

$$P(m) = \begin{cases} 1 & \text{for } m = 0, \pm 1/2 \\ 0 & \text{otherwise.} \end{cases} \quad (2.10)$$

If, as is usually the case, the alignment is not complete, the $B_k(J)$ are multiplied by an attenuation coefficient, α_k , to give

$$\rho_k = \alpha_k B_k \quad (2.11)$$

and the A_k are now expressed as

$$A_k(J_1 \lambda_1 \lambda_2 J_f) = \alpha_k B_k \frac{1}{1+\delta^2} [F_k(J_f \lambda_1 \lambda_1 J_1) + 2\delta F_k(J_f \lambda_1 \lambda_2 J_1) + \delta^2 F_k(J_f \lambda_2 \lambda_2 J_1)]. \quad (2.12)$$

The experimental A_k 's are related to the theoretical A_k 's by the attenuation coefficients, α_k 's:

$$A_k^{\text{exp}} = \alpha_k A_k^{\text{Theor.}} \quad (2.13)$$

In this model there is only one parameter, the width of the Gaussian distribution, σ . The α_k 's are related to σ through the statistical tensor, ρ_k . Because there is only one parameter, only one α_k can be uniquely determined and this is usually chosen to be the α_2 . Thus the α_4 and α_6 are determined by α_2 . The relationship is

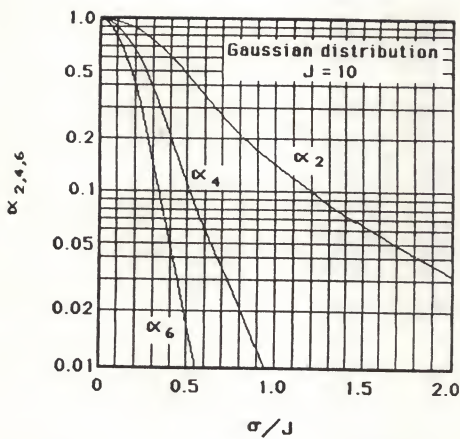


Figure 2-8. Dependence of α_j on the distribution parameter σ/J (10).

expressed graphically in Figure 2-8. The α_6 's fall off so fast with energy that they are usually not taken into account.

In a nuclear level which is fed directly after the evaporation process, the high degree of alignment implies a large attenuation coefficient. A level which is fed through a cascade of gamma rays becomes less aligned by an amount which depends on the number of gamma ray transitions. Therefore one expects increasing α_2 with both increasing spin and increasing level energy if the assumption of the Gaussian distribution of magnetic substates is correct. In Figures 2-9 and 2-10 the experimentally derived α_2 's are plotted against spin and level energy respectively. The α_2 's do show a general increase for both spin and energy implying that we can assume a Gaussian distribution of magnetic substates.

Angular Distributions

The angular distribution measurements are covered in detail in reference 12. However a brief review will be given since the results are used in the data analysis reported here.

The same detectors, beam, and target were used as in the coincidence experiment. The angular distributions were measured with the ORTEC detector. The PGT detector was used as a monitor for normalization purposes. Data were collected at five angles measured with respect to the beam axis; 0° , 30° , 45° , 60° , 90° . Figure 2-11 shows the experimental setup. A correction to the measured intensities was made for the absorption of gamma rays by the target chamber using the equation

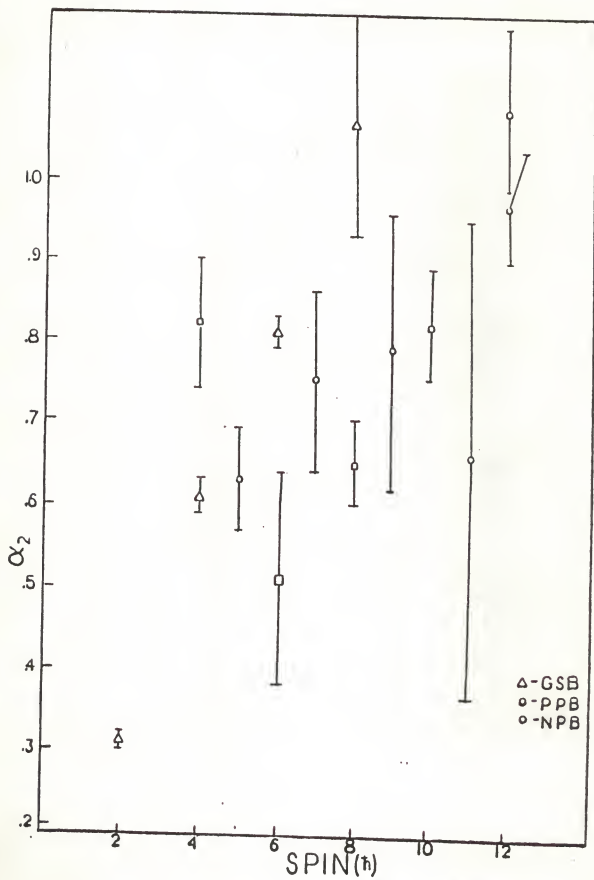


Figure 2-9. Experimental α_2 's vs. spin.

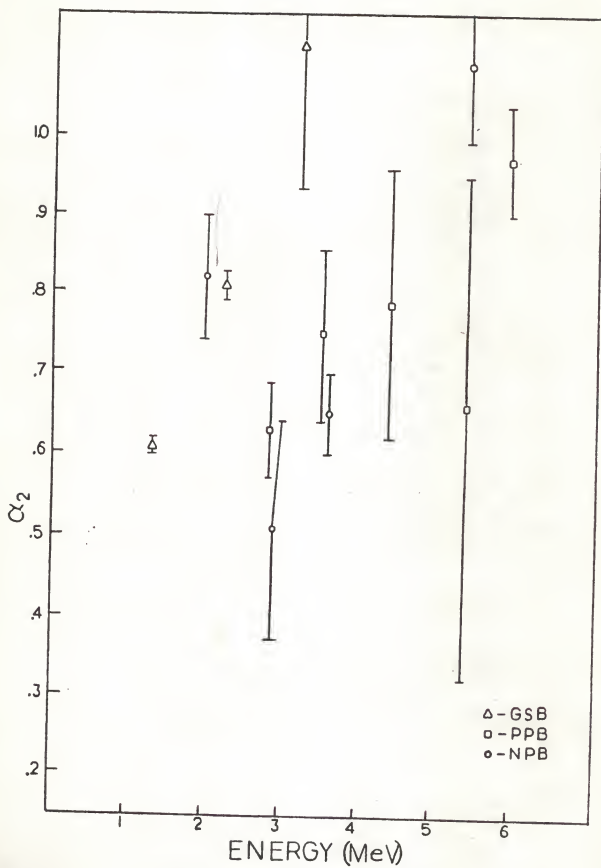


Figure 2-10. Experimental α_2 's vs. level energy.

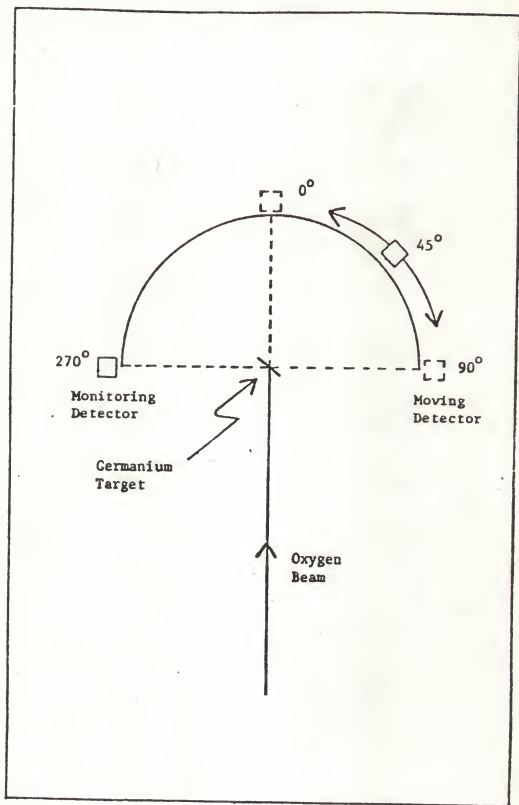


Figure 2-11. Experimental setup for angular distribution measurements (12).

$$I = I_0 \exp[-(\sigma(\text{Cu}) + \sigma(\text{Ta}))x] \quad (2.14)$$

where I_0 and I refer to the gamma ray intensity before and after absorption, σ is the absorption coefficient, and x is the thickness of material through which the gamma rays passed. Correction factors were also applied to account for the finite solid angle subtended by the detector. Calibrations of the detectors for energy and efficiency were done following the same procedures as those used for the coincidence experiments.

The program ANGDIS (12) was used to do a least squares fit of the data to the equation

$$W(\theta) = 1 + \frac{A_2}{A_0} P_2(\cos\theta) + \frac{A_4}{A_0} P_4(\cos\theta). \quad (2.15)$$

The intensities were normalized to the 90° intensity for each gamma ray. The function $W(\theta)$ was plotted as a function of the square of the cosine of the experimental angle. The results of the fit are presented in Table II-2, taken from reference 12, and Table II-3.

Polarization

Theory

The relative parities of two nuclear levels are determined from the measurement of the linear polarization of the gamma ray which decays from one level to the other. The parity of the gamma ray, π_γ , is related to the parities of the initial and final states, π_i and π_f , by

$$\pi_f = \pi_i \times \pi_\gamma. \quad (2.16)$$

TABLE II-2
Results of the Angular Distribution Experiment

Energy	A_2	A_4	ΔJ	χ^2
73.5	-0.60 (9)	0.73 (10)	1	9.94
85.1	-0.60 (9)	0.70 (10)	1	4.86
156.9	0.20 (14)	-0.12 (16)	—	1.39
269.0	-0.17 (13)	0.22 (17)	1	0.24
379.9	0.26 (14)	-0.08 (18)	0	0.89
387.8	0.44 (19)	-0.35 (22)	2,0	0.04
403.9	-0.53 (4)	-0.06 (6)	1	3.22
406.5	-0.50 (8)	-0.06 (10)	1,0	0.17
415.1	0.22 (3)	-0.22 (4)	2,0	0.07
443.4	0.35 (8)	-0.30 (10)	2,0	0.17
522.1	-1.05 (7)	0.12 (6)	1	2.83
537.0	0.56 (5)	-0.08 (5)	1,0	5.38
569.5	0.92 (3)	0.03 (3)	1,0	3.79
573.6	0.22 (1)	-0.14 (1)	2	12.5
596.3	0.29 (5)	0.09 (6)	1,0	5.16
602.1	0.15 (4)	-0.07 (5)	0	0.42
606.9	0.22 (6)	-0.16 (6)	0	0.28
622.6	0.35 (3)	-0.18 (5)	2,0	0.51
667.6	-0.14 (4)	-0.28 (5)	0	0.40
694.1	0.33 (5)	-0.09 (7)	2	1.22
707.6	0.54 (7)	0.49 (18)	1	0.42
714.3	0.10 (13)	0.55 (21)	1	8.39
736.0	0.34 (6)	-0.23 (7)	2,0	1.90
755.0	0.31 (1)	-0.15 (1)	2	2.00
786.4	0.28 (2)	-0.21 (2)	2	0.76
801.0	0.34 (3)	-0.20 (3)	2	0.53
803.0	0.85 (3)	-0.08 (4)	1,0	1.75
820.2	0.42 (3)	-0.22 (3)	2	0.07
840.3	0.23 (6)	-0.52 (8)	0	2.73
842.2	0.52 (8)	-0.29 (9)	0	2.61
861.8	0.75 (9)	-0.04 (10)	1,0	1.77
876.2	0.33 (7)	-0.05 (8)	2	0.14
900.8	0.37 (1)	-0.17 (2)	2	1.14
941.4	0.22 (3)	-0.10 (4)	2,0	4.32
962.2	0.10 (5)	-0.04 (7)	—	5.43
1003.2	0.44 (4)	-0.28 (4)	2	2.69
1005.3	0.27 (12)	-0.05 (12)	2	0.09
1013.3	0.54 (7)	-0.20 (6)	0	0.13
1052.8	0.82 (22)	0.00 (25)	—	0.02
1059.0	0.43 (6)	-0.04 (8)	—	0.64
1107.4	-0.13 (9)	0.08 (11)	2	0.02
1115.4	-0.21 (10)	0.18 (9)	1	1.33
1116.0	0.25 (8)	-0.38 (8)	2	0.42
1144.2	0.07 (4)	-0.20 (6)	2,0	7.22
1175.6	0.08 (13)	0.48 (19)	1	0.26
1181.0	-0.46 (18)	-0.20 (27)	2,0	0.10
1196.6	0.88 (17)	-0.72 (19)	0	2.40
1230.0	0.28 (9)	-0.28 (13)	2,0	1.15
1269.3	-0.59 (22)	0.09 (24)	1,0	0.92
1296.1	-0.43 (4)	0.04 (5)	1	1.95
1310.2	0.14 (10)	-0.12 (13)	—	0.13
1336.5	-0.12 (6)	0.04 (8)	1,0	0.35
1393.2	0.47 (7)	0.23 (9)	1	0.78
1488.9	-0.21 (2)	0.00 (3)	1	0.00
1633.5	0.30 (9)	0.04 (12)	—	0.44

TABLE II-3
Additional Angular Distribution Results

Energy (keV)	A_2	A_4	ΔJ
261.8	0.50 (14)	-0.21 (16)	2,0
423.5	-0.33 (04)	-0.03 (05)	1
439.9	-0.12 (07)	-0.01 (09)	1
598.6	0.23 (04)	0.10 (05)	1
712.4	0.22 (12)	0.37 (19)	1
758.8	0.43 (10)	-0.40 (11)	2,0
841.3	0.62 (07)	-0.35 (09)	2,0
876.0	-0.20 (26)	-0.00 (38)	2,1,0
951.1	0.42 (06)	-0.46 (07)	2,0
1013.0	0.48 (08)	-0.14 (65)	2,0
1056.0	0.50 (13)	0.04 (15)	1
1135.5	-0.60 (10)	0.65 (13)	1

The parity of electromagnetic radiation is dependent on the multipolarity and magnetic or electric character of the radiation:

$$\pi[E(\lambda)] = (-1)^\lambda$$

$$\pi[M(\lambda)] = (-1)^{\lambda+1}. \quad (2.17)$$

The multipolarity is established in the angular distribution measurements, but since the angular distribution of a multipole expansion is the same for both electric and magnetic radiation, linear polarization measurements are necessary for the determination of nuclear parities. These measurements take advantage of the fact that \vec{E} and \vec{B} differ in their orientation with respect to λ :

$$\vec{B} \parallel \lambda \text{ for electric radiation}$$

$$\vec{E} \parallel \lambda \text{ for magnetic radiation.}$$

With λ oriented in a plane perpendicular to the beam axis, observations at right angles to the beam axis will provide a means for differentiating between electric and magnetic radiation. For electric radiation, \vec{E} will be perpendicular to the plane and for magnetic radiation \vec{E} will lie in the same plane as $\vec{\lambda}$.

The sensitivity of the Compton effect to the polarization of an incoming gamma ray can be used to study linear polarizations. The cross section for Compton scattering summed over all directions of the scattered gamma ray is given by the Klein-Nishina formula (13):

$$\frac{d\sigma}{d\Omega} = \frac{r_0^2}{2} \frac{k^2}{k_0^2} \left[\frac{k_0}{k} + \frac{k}{k_0} - 2 \sin^2 \theta \cos^2 \phi \right] \quad (2.18)$$

where

$$k = \frac{k_0}{1 + \frac{k_0^2}{m_0^2 c^2 (1 - \cos \theta)}} \quad (2.19)$$

The geometry of the scattering process is defined in Figure 2-12. It can be seen from the formula that for measurements taken at $\theta = 90^\circ$ the cross section is maximized in a plane perpendicular to the electric vector ($\phi = 90^\circ$).

The polarization of a photon is defined as (10)

$$P(\theta) = \frac{W(\theta, 0^\circ) - W(\theta, 90^\circ)}{W(\theta, 0^\circ) + W(\theta, 90^\circ)} \quad (2.20)$$

where (14)

$$W(\theta, \phi) = \sum_k [A_k P_k(\cos \theta) \pm \cos 2\phi A_k K_k P_k^2(\cos \theta)] \quad (2.21)$$

$$K_k(\lambda_1 \lambda_2) = - \left[\frac{(k-2)!}{(k+2)!} \right]^{1/2} \frac{C(\lambda_1 \lambda_2 k, 1 \ 1)}{C(\lambda_1 \lambda_2 k, 1 - 1)} \quad (2.22)$$

and

$$P_k^2(\cos \theta) = (1 - \cos^2 \theta) \frac{d^2 P_k(\cos \theta)}{d^2(\cos \theta)} \quad (2.23)$$

Here K depends on the multipolarity of the radiation and the C 's are Clebsch-Gordan coefficients. The angle between the \vec{E} vector and the reaction plane is defined by ϕ . Since the measurements are made at $\phi = 0^\circ$ or 90° , $\cos 2\phi$ is ± 1 . The P_k^2 are unnormalized associated Legendre

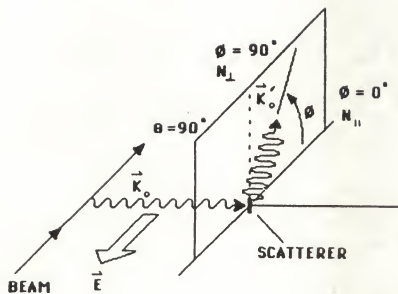


Figure 2-12. Geometry of the scattering process (10).

functions. The plus sign refers to even parity radiation (M1 or E2) and the minus sign refers to odd parity radiation (E1 or M2).

Substituting the values of $W(\theta, \phi)$ into the equation for $P(\theta)$ and using the appropriate values for dipole and quadrupole transitions, one obtains the theoretical formulas for linear polarizations:

$$1) \text{ Dipole} \quad P(90^\circ) = \pm \frac{1 + A_2}{1 - 2A_2} \quad (2.24)$$

$$2) \text{ Quadrupole} \quad P(90^\circ) = \pm \frac{1 + A_2 + A_4}{1 - 2A_2 - A_4/4} \quad (2.25)$$

$$3) \text{ Mixed} \quad P(90^\circ) = \pm \frac{3(A_2 + B_2) + 1.25A_4}{2 - A_2 + 0.75A_4} \quad (2.26)$$

where

$$B_2 = \frac{-8\delta A_2 F_2(J_f L_1 L_2 J_1)}{3[F_2(J_f L_1 J_1 J_1) + 2\delta F_2(J_f L_1 L_2 J_1) + \delta^2 F_2(J_f L_2 L_2 J_1)]} \quad (2.27)$$

The mixing ratio, δ , is defined with the sign convention of Krane and Steffen (15). The F_k 's are tabulated in Yamazaki (11). In each case, (1) - (3), the sign of the polarization is taken to be positive if there is no parity change (M1, E2, and E2/M1) and negative if there is a parity change (E1, M2, and M2/E1).

Experiment

Linear polarizations of the gamma rays produced in the reaction $^{70}\text{Ge}(^{16}\text{O}, \text{xpxn})$ were measured with a four element Compton polarimeter belonging to Vanderbilt University. The four HpGe coaxial detectors

TABLE II-4
Properties of the Individual Germanium Detectors in the Polarimeter

Detector	D	A	C	B
Identification Number	1258	1256	1257	1259
Outside Diameter (mm)	42.2	41.8	42.0	42.8
Length (mm)	50.7	50.4	50.0	50.8
Nominal Active Volume (cm ³)	63.0	58.0	60.0	62.0
Face Dead Layer Thickness (mm)	0.26	0.42	0.37	0.33
Efficiency (relative to a 3" x 3" NaI at 25 cm and E _γ = 1.33 MeV) (%)	12.0	12.0	12.0	12.0
Resolution (FWHM @ E _γ = 1.33 MeV) (keV)	2.03	2.02	2.01	1.90
Peak to Compton Ratio	40.0	37.8	38.3	38.3

were mounted closely together in a single cryostat. The individual characteristics of each detector are given in Table II-4 and the experimental setup is shown in Figure 2-13.

Each crystal acts as both a scatterer and an analyzer. An incoming gamma ray is Compton scattered off an electron in one detector, depositing part of its energy there. The scattered gamma ray is then detected in one of the other detectors. If the two events occur within a preset time window, the signals from the two detectors are summed. If the full energy of the scattered gamma ray is deposited in the second detector, the summed signal represents the total energy of the incoming gamma ray.

The electronics setup is shown in Figure 2-14. Summing of the energy signals before processing them in the spectroscopy amplifiers seemed to give better energy resolution than summing the amplified energy signals. The timing circuits were used to set the gates which established whether the event was valid and therefore to be counted.

The experimental asymmetry is defined as

$$\Delta = \frac{N_{\perp} - N_{\parallel}}{N_{\perp} + N_{\parallel}} . \quad (2.28)$$

The values of N_{\perp} and N_{\parallel} for a given gamma ray are determined by measuring the area under the full energy peak in the spectra representing photons scattered perpendicular and parallel to the reaction plane respectively. In this experiment AC and BD represented the perpendicular scattering and CD and AB represented the parallel scattering. Because of a malfunction in the preamplifier for detector

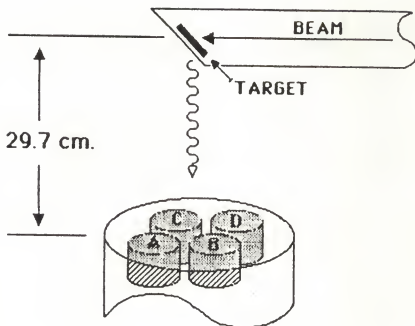
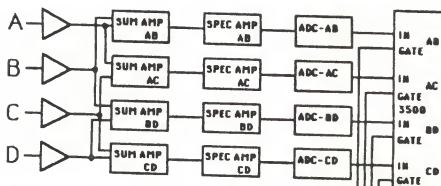


Figure 2-13. Experimental setup for polarization experiment.

LINEAR CIRCUITS



TIMING CIRCUITS

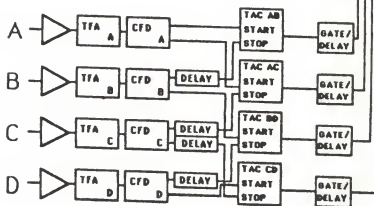


Figure 2-14. Electronics configuration for polarization experiment.

B, there were not sufficient data to use the results from BD and AB. Therefore the experiment was analyzed as though the detector were a three-element polarimeter.

Because all three detectors were acting as both scatterer and analyzer, the perpendicular and parallel counting rates could be measured simultaneously, thus reducing systematic errors such as those due to variations in beam position and beam current. Normalization was unnecessary. Only a correction for the relative efficiencies of the two pairs needed to be done. Although the detectors were carefully matched in size and mounted symmetrically about the center of the polarimeter, there appeared to be a difference in detection efficiency between AC and CD. This could have been due either to the target being off center or, more likely, mismatches in the electronics. There was a one hundred channel 'dip' in the spectra produced by the parallel pair (CD) at about 250 keV and the counting rate was lower in CD (see Figure 2-15). The origin of the dip may have been due to a problem with the timing signal. A result of the different efficiencies can be clearly seen in Figures 2-16(a) and (b) which show the 511 keV peak for each of the two pairs.

Because the radiation due to radioactivity is assumed to be unpolarized, the requirement was made that the asymmetry ratio, Δ , for gamma rays from radioactive sources would be zero. This implied that $N_{\perp} = N_{\parallel}$, or $N_{\perp}/N_{\parallel} = 1$. A plot of N_{\perp}/N_{\parallel} vs. energy for a mixed radioactive source spectrum and a ^{226}Ra source spectrum is shown in Figure 2-17(a). The error bars are large due to the relatively low intensity of the sources and the resulting low counting rates in the two pairs of detectors. The points were fitted to a quadratic formula:

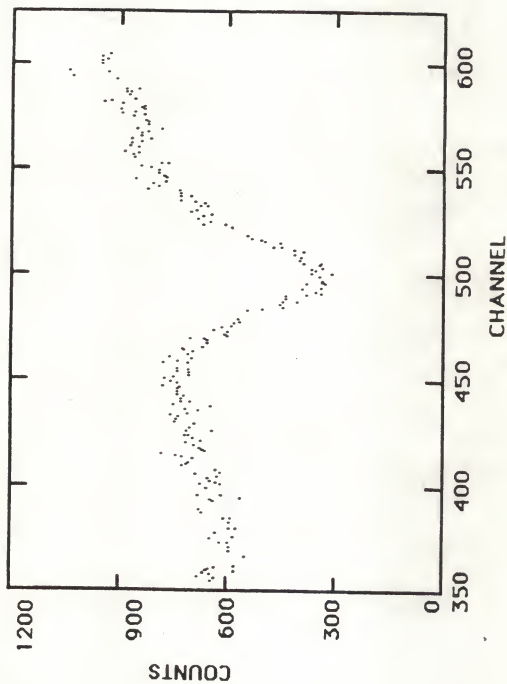


Figure 2-15. "Dip" in spectrum taken by detector pair CD.

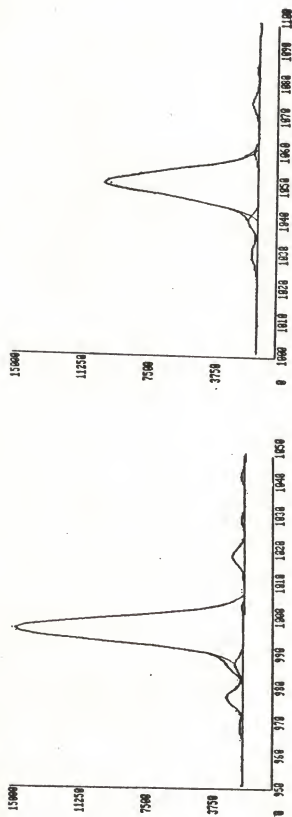


Figure 2-16. 511 keV peak in detector pair AC (a) and CD (b).

$$N_{\perp} = [A + BE + CE^2]N_{11} = f(E)N_{11} \quad (2.29)$$

where $A = 2.18$ $B = -0.211 \times 10^{-2}$ $C = 0.107 \times 10^5$ and $f(E)$ is the relative efficiency of the two pairs AC (N_{\perp}) and CD (N_{11}). A plot of $N_{\perp}/f(E)N_{11}$ vs. energy is shown in Figure 2-17(b). The weighted average of the ratios is $.99 \pm .01$.

The experimental polarization is obtained by dividing the asymmetry, Δ , by the polarimeter efficiency, Q :

$$P_{\text{exp}} = \frac{\Delta}{Q}.$$

The efficiency of the polarimeter depends on how well it can discriminate between the scattering angles of the gamma rays (16). The maximum efficiency, Q_0 , is achieved with point-size crystals and is defined as

$$Q_0 = \frac{1 + (E_{\gamma}/m_0c^2)}{1 + (E_{\gamma}/m_0c^2) + (E_{\gamma}/m_0c^2)^2}. \quad (2.30)$$

The actual efficiency, Q , is less than Q_0 since crystals with a finite size accept a larger range of scattering angles. Because Q_0 is a slowly varying function, the shape of the curve for Q should not change much. A reasonable approximation for Q is therefore given as (16)

$$Q = Q_0(a + bE). \quad (2.31)$$

Using known stretched E2 transitions, Q can be calculated from the relationship $Q = \Delta/P_{\text{ad}}$. The value of the polarization, P_{ad} , is

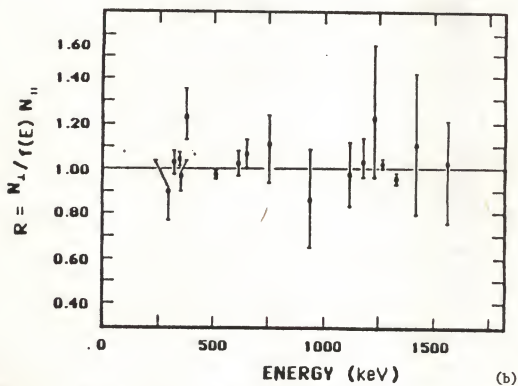
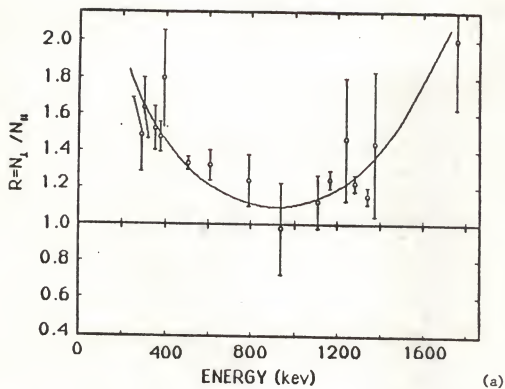


Figure 2-17. Asymmetry ratios between perpendicular and parallel detector pairs; (a) uncorrected and (b) corrected.

calculated from equation 2.25 with the A_2 's and A_4 's obtained from the angular distribution measurements. A least squares fit to the data points determines the parameters a and b in equation 2.31. Figures 2-18(a) and (b) show graphs of Q and Q_0 as functions of E_Y for the polarimeter at two distances (29.7 cm. and 15.2 cm.). The data points which were used to obtain the least squares fit are included. In Figure 2-18(a), the values of a and b are $a = .735$ and $b = -.537 \times 10^{-4}$. Figure 2-18(b) represents Q for the parameters $a = .764$ and $b = -.443 \times 10^{-4}$.

The polarization data were collected for 25 hours with the polarimeter at 29.7 cm. from the target and for 14 hours at 15.2 cm. from the target. Data were recorded in two hour runs and added together. When the preamplifier for detector B failed twenty-one hours after the start of the experiment, one end of the preamplifier signal cable for detector D was left hanging loose. The loose cable caused poor resolution in the CD detector pair. The cable was reconnected six hours after the detector was moved to 15.2 cm. from the target. Data taken during the time the cable was loose were not considered in the analysis. The data from the two runs, hereafter called experiment 1 (29.7 cm.) and experiment 2 (15.2 cm.), were analyzed separately and the results were averaged with a weighted average

$$\bar{P} = \frac{\sum_{i=1}^N \frac{P_i}{\sigma_i^2}}{\sum_{i=1}^N \frac{1}{\sigma_i^2}}, \quad \frac{1}{\sigma_T^2} = \sum_{i=1}^N \frac{1}{\sigma_i^2}. \quad (2.32)$$

TABLE II-5
Results of the Polarization Experiment

E_γ (keV)	$J_i \rightarrow J_f$	P_{exp}	P_{cal} (b)	δ (c)	Multipolarity
522.1	$12^- \rightarrow 11^-$	0.08 (12)		-0.53 (37)	E2/M1
573.6	$2^+ \rightarrow 0^+$	0.27 (05)	0.29 (01)		E2
602.2	$2^{+'} \rightarrow 2^+$	-0.20 (08)		2.8 (2.4)	E2/M1
606.6	$6^{+'} \rightarrow 6^+$	0.03 (16)		0.62 (51)	E2/M1
667.5	$4^{+'} \rightarrow 4^+$	-0.14 (23)		1.1 (1.3)	E2/M1
755.0	$4^+ \rightarrow 2^+$	0.49 (07)	0.47 (01)		E2
786.4	$8^{+'} \rightarrow 6^{+}$	0.48 (10)	0.37 (01)		E2
801.1(a)	$10^{+'} \rightarrow 8^{+}$	0.63 (10)	0.51 (02)		E2
820.2	$4^{+'} \rightarrow 2^{+}$	0.71 (08)	0.70 (04)		E2
840.2(a)	$6^{+'} \rightarrow 4^{+}$	0.37 (21)	0.03 (05)		E2
876.0(a)	$9^- \rightarrow 7^-$	0.48 (09)	0.57 (06)		E2
900.8	$6^+ \rightarrow 4^+$	0.53 (10)	0.60 (01)		E2
941.3	$(9^-) \rightarrow (7^-)$	0.40 (16)	0.31 (02)		E2
951.1	$(7^+) \rightarrow (5^+)$	0.33 (40)	0.55 (07)		E2
1003.3(a)	$12^+ \rightarrow 10^{+}$	0.28 (13)	0.72 (04)		E2
1013.4	$8^+ \rightarrow 6^+$	0.27 (15)	0.89 (53)		E2
1115.8	$3^+ \rightarrow 2^+$	-0.99 (68)		-22.2 (13.8)	E2/M1

Table II-5 continued

E_γ (keV)	$J_i \rightarrow J_f$	P_{exp}	P_{cal} (b)	δ (c)	Multipolarity
1117.0	$14^+ \rightarrow 12^+$	0.62 (39)	0.19 (06)		E2
1296.2	$7 \rightarrow 6^+$	0.18 (28)		-0.36(13)	M2/E1
1489.0	$5^- \rightarrow 4^+$	-0.68 (31)	-0.29 (01)		E1

(a) Unresolved doublet.

(b) Calculated assuming no parity change and no mixing.

(c) Calculated with A_{2exp} , A_{4exp} , and P_{exp} .

The experimental polarizations (P_{exp}) for ^{82}Sr are listed in Table II-5. The first column gives the transition energies in keV. The second column gives the initial and final spin and parity assignments based on previous experimental studies (12, 17-20) and the present angular distribution and polarization measurements. The experimental polarizations are listed in column three. The polarizations in column four were calculated using equation 2.25 for stretched E2 transitions. The mixing ratios for mixed transitions are listed in column five. These values were obtained from equations 2.26 and 2.27 using $A_{2\text{exp}}$, $A_{4\text{exp}}$ and P_{exp} . Because the experimental values were used, the calculated δ is independent of any assumptions made about the parameter α_2 . However since equations 2.26 and 2.27 are quadratic in δ , the adopted value is the one which agrees most closely with the δ obtained from the χ^2 fit to the angular distribution and polarization data.

A goodness-of-fit index, χ^2 , was calculated for different values of initial and final spins. For each pair of spins, the attenuation coefficient $\alpha_2(J_1)$ and the multipole mixing ratio δ are changed in steps and the χ^2 is calculated at each step, where

$$\begin{aligned} \chi^2 = \sum_{i=1}^3 \chi_i^2 = & [A_{2\text{exp}} - A_{2\text{cal}}(J, \delta, \alpha)]^2 / \epsilon_{A_2}^2 \\ & + [A_{4\text{exp}} - A_{4\text{cal}}(J, \delta, \alpha)]^2 / \epsilon_{A_4}^2 \\ & + [P_{\text{exp}} - P_{\text{cal}}(J, \delta, \alpha)]^2 / \epsilon_P^2. \end{aligned} \quad (2.33)$$

The calculated polarization P_{cal} is obtained with equations 2.26 and 2.27 and A_{2cal} and A_{4cal} are calculated with equation 2.12. The experimental angular distribution coefficients were taken from reference 12. The ϵ_{A_2} , ϵ_{A_4} , and ϵ_p are the experimental errors. In equation 2.23 the number of degrees of freedom is equal to the number of experimental quantities minus the number of free parameters. The three experimental parameters are A_{2exp} , A_{4exp} , and P_{exp} . There are two parameters, δ and α_2 , but α_2 is not completely free since it is restricted to values between zero and one and to values less than those obtained for the levels above it in the cascade. Therefore, the confidence limits for χ^2 are based on two degrees of freedom.

Data Analysis

Fitting Code - RLCFIT

Difficulty with fitting the spectra obtained from background subtracted coincidence gates with available fitting codes led to the development of a new spectral analysis code, RLCFIT, by Coldwell (21). It is a least squares curve fitting routine in which the entire spectrum is fitted as a unit until the chi-square value is equal to or less than the number of data points.

The first step one takes in using the program is to define a standard peak shape by using the program SHAPE to fit splines to a reasonably clean peak which is representative of the shapes of the other peaks. A series of up to nine spline functions are fitted to the given peak and the coefficients of those splines are output for use as the standard in RLCFIT.

The fitting process begins by fitting the background with a Cooley-Tukey fast Fourier transform (21) and examining the residuals (the weighted difference between the fit and the data) for peaks. In each location where the residuals are the largest, a standard peak is placed. The standard is then adjusted with respect to its width, height, and location to fit the data. The background and peaks are then refitted and the chi-square evaluated. Again the residuals are examined for the possibility of missed peaks, peaks are placed and fitted, and the whole spectrum is refitted. This process is repeated through many iterations until the chi-square value is equal to less than the number of data points or one of a number of other stopping mechanisms is reached. An example of the fit obtained with this program is seen in Figure 2-19. The dots are the data points and the lines the fitted values. The residuals are plotted across the top.

Several adjustable parameters are used in the program to adjust the degree of fit. The number of peaks expected puts a limit on the number of peaks which can be fitted. The peak widths are varied within limits set by estimating the average peak widths at the low and high energy ends of the spectrum. The widths can be allowed to vary between 75% and 150% with respect to a quadratic curve which is fitted to the widths. The ratio of the size of the background oscillations to the width of the peaks in the middle of the spectrum influences how closely the background fits the data. This number varies between 4.0 and 16.0 for the type of spectra fitted in the present experiment. The code will attempt to add peaks until the largest residual is less than a number

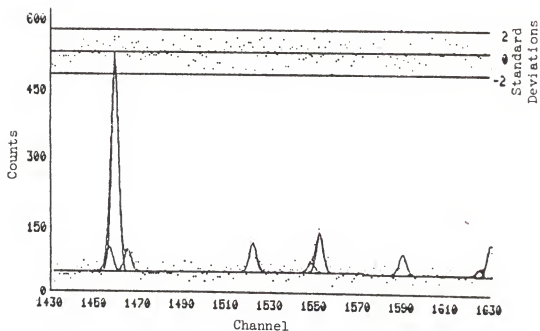
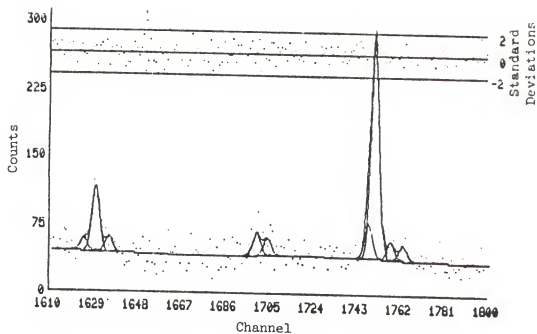


Figure 2-19. Examples of output of fitting code RLCFIT. Along the bottom the dots represent the data and the solid lines the fit. At the top the dots represent the weighted difference between the fit and the data.

which is specified on input. This enables one to do a first pass fit to get only the largest peaks or to fit the data very closely, resolving peaks down to the noise level.

For background subtracted spectra, the statistics and error analysis become unreliable because the number of counts in each channel does not accurately represent the data. This is resolved by using the subroutine ABKG which estimates the effect the subtracted background would have by weighting each data point by a factor which is determined from the scatter of the points.

The errors in the fitting process arise from both the random nature of the data and the ambiguities in the possible ways to fit the data. After the spectrum is fitted and the chi-square minimized, an abbreviated version of the whole process is repeated to ascertain the range of errors. Each calculated fitting constant is varied within its standard deviation. In the spectrum, all peaks within 2.5 standard deviations of the background are removed and each data point is varied randomly around its experimental value with an appropriate Gaussian distribution. Then the spectrum is refitted, usually adding back the removed peaks, and the chi-square is minimized with respect to all of the constants. Repeating this process three times is usually sufficient to determine the probable errors. Further refits do not change the calculated errors by a significant amount.

An earlier version of this code, RCOLD, differed from the present one in two ways; (1) The spectrum was fitted in sections, and (2) In the background subtracted gates the estimated background that is determined from the scatter of the points was added to the data, generating an

artificial background. The chief benefits of the present code over the original one are a more accurate determination of the background and a minimization of the chi-square over the entire spectrum.

Energy and Efficiency Determinations

The energies were determined with a three-step process. First an NBS mixed radioactive source spectrum was taken with the source outside the target chamber but in the target position. Then, with the source still in place, an ^{16}O beam was put onto the ^{70}Ge target. That spectrum was then calibrated against the NBS source energies, thus giving the energies of the reaction yield products. A self-consistent set of the reaction gamma-ray energies were used to calibrate the singles and the sum-projected coincidence spectra. Using the energies from the source-plus-beam run and the fitted peak channels from the spectrum being calibrated, the overall variation of delta, the difference between the calibration energy and the calculated energy, is less than 0.10 keV over an energy range of 85 keV to 1764 keV. The energies were fitted to a polynomial using the program GEFI (22). The energies which were adopted were taken from the angular distribution data. The energies and errors from each of the five angles (0° , 30° , 45° , 60° , 90°) were averaged with formula 2.32. The errors in the table include only the statistical errors. The adopted energies and intensities are given in Table II-5.

The efficiency calculations were done with the same NBS mixed standard source. The detector efficiency for each peak was determined and the natural logarithm of each efficiency point was fitted to a polynomial using the least-squares fitting routine MULT (23). The efficiency vs energy relationship that was used was

$$\ln e = A_0 + A_1 E + A_2 E^2 + A_3 E^3 + \dots \quad (2.34)$$

The relative intensities of the gamma rays were calculated by dividing the area under the peak by the efficiency of the detector at that energy. These intensities were normalized to the 573.6 keV gamma ray which was assigned an intensity of 100%. Because the intensities were a weighted average over the five angles of the angular distribution data, the effects of the anisotropies were averaged out. The errors quoted for the intensities are only the statistical errors. The intensity errors are larger than the energy errors due to the method of fitting. The energy errors are due to the uncertainty in the position of the center of the peak that is usually rather small. The intensity errors are proportional to the errors in the calculation of the area under the peak. That error is estimated by allowing each data point to randomly vary within its standard deviation and refitting the peak and background, a process that is repeated three times to determine the effect this variation will have on the peak area. The effect is expressed as the error in the area. It does not reflect the accuracy of the final fit, but rather the statistical uncertainty of the counting process.

The energy levels were calculated by a weighted average of the summed energies along the paths through which the level can decay. The results are found in Table II-6. The quoted errors are the statistical errors. These level energies are compared to those published by other authors in Table II-7.

TABLE II-6
Energies and Relative Intensities of the Gamma Rays in ^{82}Sr

Energy (keV)	Relative Intensity
85.35 (02)	6.50 (34)
156.94 (03)	.93 (06)
261.83 (04)	1.94 (13)
269.02 (05)	1.46 (11)
379.96 (05)	2.01 (15)
403.91 (01)	4.47 (25)
406.48 (05)	2.47 (15)
415.14 (01)	13.56 (52)
423.51 (01)	5.09 (22)
439.88 (02)	3.58 (18)
443.28 (03)	3.48 (17)
513.68 (03)	9.62 (46)
522.09 (01)	3.79 (27)
534.11 (04)	4.30 (24)
537.00 (04)	6.69 (27)
569.57 (01)	11.88 (47)
573.64 (01)	100.00 (3,59)
583.13 (02)	7.01 (31)
598.56 (03)	8.18 (33)
602.15 (01)	23.89 (96)

Table II-6 continued

Energy (keV)	Relative Intensity
606.65 (05)	10.07 (55)
667.53 (05)	5.57 (41)
694.04 (02)	17.15 (73)
712.44 (03)	2.49 (17)
755.03 (01)	88.11 (3.27)
758.77 (02)	7.35 (42)
786.36 (01)	22.04 (81)
801.11 (01)	23.97 (91)
802.94 (02)	14.79 (59)
820.25 (01)	16.35 (62)
837.37 (02)	9.29 (39)
840.24 (01)	21.47 (96)
841.34 (05)	4.64 (25)
876.02 (06)	7.50 (74)
900.84 (01)	45.86 (1.68)
941.26 (02)	10.06 (38)
951.15 (03)	5.25 (23)
964.60 (02)	9.27 (36)
1003.26 (03)	16.03 (71)
1005.43 (06)	8.10 (51)
1013.36 (02)	21.82 (93)
1052.76 (05)	1.57 (14)
1056.03 (04)	3.13 (19)

Table II-6 continued

Energy (keV)	Relative Intensity
1059.14 (02)	4.40 (20)
1085.90 (07)	1.80 (26)
1107.47 (02)	4.09 (23)
1115.80 (07)	8.56 (40)
1116.85 (10)	3.31 (26)
1135.52 (03)	2.00 (13)
1144.20 (04)	5.40 (23)
1163.74 (09)	1.72 (18)
1175.64 (05)	3.18 (21)
1180.98 (06)	1.72 (13)
1196.62 (06)	1.60 (14)
1268.74 (45)	1.45 (16)
1281.13 (22)	1.09 (13)
1283.90 (35)	.84 (15)
1296.19 (04)	4.91 (21)
1336.49 (03)	3.07 (15)
1368.41 (07)	3.45 (20)
1381.88 (02)	4.17 (21)
1393.51 (02)	3.83 (17)
1489.00 (02)	8.71 (33)
1550.98 (46)	.81 (19)
1828.39 (10)	.68 (22)

TABLE II-7
Energy Sums

J^{π}	Sums	Weighted Average
2^{+}	$0 + 1175.64 (05) = 1175.64 (05)$ $573.64 (01) + 602.15 (01) = 1175.70 (01)$	1175.78 (01)
4^{+}	$573.64 (01) + 755.03 (01) = 1328.67 (01)$	1328.67 (01)
3^{+}	$573.64 (01) + 1115.80 (07) = 1689.44 (07)$ $1175.78 (01) + 513.68 (03) = 1689.32 (06)$	1689.37 (05)
4^{+1}	$1175.78 (01) + 820.25 (01) = 1996.03 (01)$ $1328.67 (01) + 667.53 (05) = 1996.20 (05)$	1996.04 (01)
6^{+}	$1328.67 (01) + 900.84 (01) = 2229.51 (02)$	2229.51 (02)
3^{-}	$1996.04 (01) + 406.48 (05) = 2402.52 (05)$ $1689.37 (05) + 712.44 (03) = 2401.81 (06)$ $573.64 (01) + 1828.39 (10) = 2402.03 (10)$	2402.20 (04)
5^{+}	$1689.37 (05) + 837.37 (02) = 2526.74 (05)$	2526.74 (05)
(5)	$2526.74 (05) + 156.94 (03) = 2683.68 (06)$	2683.68 (06)
5^{-}	$1489.00 (02) + 1328.67 (01) = 2817.67 (02)$ $415.14 (01) + 2402.20 (04) = 2817.34 (04)$	2817.60 (02)
4^{-}	$1689.37 (05) + 1135.52 (03) = 2824.89 (06)$	2824.89 (06)

Table II-7 continued

6 ⁺	840.24 (01) + 1996.04 (01) = 2836.28 (01) 2229.51 (02) + 606.63 (05) = 2836.14 (05)	2836.27 (01)
6 ⁻	2824.89 (06) + 261.83 (04) = 3086.72 (07) 2817.60 (02) + 269.02 (05) = 3086.62 (05) 2683.68 (06) + 403.91 (01) = 3087.59 (06)	3086.95 (03)
8 ⁺	2229.51 (02) + 1013.36 (02) = 3242.86 (03)	3242.86 (03)
7 ⁺	2526.74 (05) + 951.15 (03) = 3477.89	3477.89 (06)
7 ⁻	2817.60 (02) + 694.04 (02) = 3511.64 (03) 2229.51 (02) + 1281.13 (22) = 3510.64 (22) 3087.95 (03) + 423.51 (01) = 3511.46 (03)	3511.54 (02)
7	2229.51 (02) + 1296.19 (04) = 3525.70 (04) 3086.95 (03) + 439.88 (02) = 3526.83 (04)	3526.27 (03)
(7)	2229.51 (02) + 1336.49 (03) = 3566.00 (04)	3566.00 (04)
(7)	3086.95 (03) + 522.09 (01) = 3609.04 (03)	3609.04 (03)
8 ⁺	3242.86 (03) + 379.96 (05) = 3622.82 (06) 2229.51 (02) + 1393.51 (02) = 3623.02 (03) 2836.27 (01) + 786.36 (01) = 3622.63 (01)	3622.67 (01)
(8)	3242.86 (03) + 443.28 (03) = 3686.14 (01)	3686.14 (01)
10 ⁺	3242.85 (03) + 1107.47 (02) = 4350.33 (04)	4350.33 (04)

Table II-7 continued

(9)	3526.27 (03) + 841.34 (05) = 4367.61 (07)	
	3566.00 (04) + 801.11 (01) = 4367.11 (04)	
	3609.04 (03) + 758.77 (02) = 4367.81 (04)	4367.48 (03)
9 ⁻	3511.54 (02) + 876.02 (06) = 4387.56 (06)	
	3242.86 (03) + 1144.20 (04) = 4387.06 (05)	4387.26 (04)
10 ⁺	3622.67 (01) + 801.11 (01) = 4423.78 (01)	
	3242.86 (03) + 1180.98 (06) = 4423.84 (07)	4423.78 (01)
(11)	4367.48 (03) + 941.26 (02) = 5308.74 (04)	5308.74 (04)
(11 ⁻)	4387.26 (04) + 1005.43 (06) = 5392.69 (07)	5392.69 (07)
(12 ⁺)	4423.78 (01) + 1003.26 (03) = 5427.04 (03)	5427.04 (03)
(12 ⁻)	5392.56 (07) + 522.09 (01) = 5914.78 (07)	5914.78 (07)
(13)	5308.74 (04) + 1056.03 (04) = 6364.77 (06)	6364.77 (06)
(14 ⁺)	5427.04 (03) + 1116.85 (10) = 6543.89 (10)	6543.89 (10)
(16 ⁺)	6543.89 (10) + 1283.90 (35) = 7827.79 (36)	7827.79 (36)

TABLE II-8
Comparison of Energy Level Values of Various Authors

J ^π	This Work*	Ball et al. (17)	Fields et al. (18)	Higo et al. (19)	Dewa. (20)
2 ⁺	573.6	575.	575.3	573.4	573.6
2 ⁺	1175.8	-	1179.1	1175.4	1175.7
0 ⁺	-	1310.	-	-	-
4 ⁺	1328.7	-	1332.7	1327.9	1328.5
3 ⁺	1689.4	-	1694.2	1686.6	1688.6
2 ⁺	-	1865.	-	-	-
4 ⁺	1996.0	-	2002.0	1994.8	1996.1
2 ⁺	-	2195.	-	-	-
6 ⁺	2229.5	-	2236.5	2228.4	2229.2
3 ⁻	2402.2	2405.	-	-	-
5 ⁺	2526.7	-	-	-	2525.8
0 ⁺	-	2665.	-	-	-
(5)	2683.7 (1)	-	-	-	-
5 ⁻	2817.6	2820.	2824.6	2814.6	2817.4
4 ⁻	2824.9 (1)	-	-	-	2824.2
6 ⁺	2836.3	-	2841.6	2835.4	2836.3
2 ⁺	-	2885.	-	-	-
2 ⁺	-	2920.	-	-	-
6 ⁻	3087.0	-	-	-	3086.4
8 ⁺	3242.9	-	3252.2	3241.0	3242.6
7 ⁺	3477.9 (1)	-	-	-	-
7 ⁻	3511.5	-	-	-	3511.3
(7)	3566.0	-	-	-	3565.4
(7)	3609.0	-	-	-	-
8 ⁺	3622.7	-	-	3621.2	3622.4
(8)	3686.1	-	3696.6	3686.5	3685.8
10 ⁺	4350.3	-	4363.3	4348.8	4350.2
(9)	4367.5	-	-	-	-

J^π	This Work*	Ball et. al (17)	Fields et al. (18)	Higo et al. (19)	Dewald (20)
9^-	4387.3	-	-	-	-
10^+	4423.8	-	-	-	4423.4
(11)	5308.7	-	-	-	-
(11 $^-$)	5392.6 (1)	-	-	-	-
(12 $^+$)	5427.0	-	-	-	5426.4
(12 $^-$)	5914.7	-	-	-	5915.5
(13)	6364.7	-	-	-	-
(14 $^+$)	6543.9	-	-	-	6542.4
(16 $^+$)	7827.8	-	-	-	-

*All errors not indicated are equal to or less than .05.

CHAPTER III NUCLEAR MODELS

Nuclear models can be divided into two general classifications; phenomenological and microscopic. The phenomenological models tend to be extensions of classical concepts and often explain structure in terms of well-known classical systems such as the harmonic oscillator or the rigid rotor. Amazingly, the predictions of these somewhat simple models are sometimes quite accurate and, more often, a good first approximation.

The microscopic models approach nuclear structure from a more mathematical point of view. Beginning with a set of wave functions and a Hamiltonian, complex computer codes are used to predict nuclear energy levels, transition probabilities, quadrupole moments, etc. Attempts have been made to explain nuclear structure without free parameters (24). More often, nuclear structure theory consists of a fit of experimental observations to a collection of parameters.

The experiments described in the last chapter were performed to determine the energies, spins, and parities of the excited nuclear states of ^{82}Sr . This information is most interesting when compared to the predictions of nuclear theories. In the $A = 80$ mass region there is no one model that satisfactorily describes the characteristics of all the nuclei. The collective models (rotational, vibrational, and interacting boson) have been applied most successfully to the lower spin states of nuclei in this region of the nuclear chart. Levels which are not described in terms of such collective models are usually explained

in terms of quasiparticle excitations. A model which takes into account the quasiparticles is the quasiparticle-plus-rotor model.

The following is a review of the nuclear models which have been compared to ^{82}Sr data in an attempt to understand its structure. Although the nuclear shell model (25) does not provide an adequate description of ^{82}Sr it is presented first since it is the foundation from which the other models have been developed. The vibrational model (26) applies to nuclei near closed shells, but the low-lying energy levels in ^{82}Sr are similar to those predicted by the simple harmonic oscillator vibrational model. The first few levels in the first excited positive parity band are evenly spaced indicating vibrational characteristics. The Bohr-Mottelson rotational model (26) is the basis for many of the relationships that are used to characterize the nucleus such as the standard moment of inertia plot ($2\theta/\hbar^2$ vs. $\hbar^2\omega^2$) and the relationships between the $B(E2)$'s, the quadrupole moments, and the deformation parameter, β . The level spacings in ^{82}Sr do not conform to the well-deformed rotor model predictions, but they do show evidence of deformation and rotation. Two versions of the interacting boson model have been applied to ^{82}Sr by several authors, the IBM-I and the IBM-II (18-20, 27-28). The predictions of the model compare favorably to the experimental levels of the ground state band and the first excited positive parity band. Only the high spin states ($I > 10^+$) differ significantly from the predictions of the various collective models. This is probably due to quasiparticle excitations which lower the collective levels. In the quasiparticle-plus-rotor (QPR) model (29) the ground state band is fitted with the variable moment of inertia (VMI) model (30) and the Coriolis-mixing operators are applied to the wave

functions generated by the Nilsson model (31) to obtain the quasiparticle excitations. In the cranked shell model (CSM) the quasiparticle motion is considered in a uniformly rotating potential (32). This model has only recently been applied to transitional nuclei to study the interplay between few-particle excitations and collective properties (33).

All of these models are covered briefly in order to define the terminology. A review of the literature in which these models are applied to ^{82}Sr is included. The predictions of each model are then compared to the experimental data obtained in the present study.

The Shell Model

The shell model was developed in an attempt to explain phenomena that occurred systematically throughout the nuclear chart. These included nuclear binding energies, nuclear magnetic moments, the excitation energies of even-even nuclei, and ground state spins. The basic assumption of the simplest shell model is that the nucleons move independently of one another in stationary orbits with fixed angular momentum much like the electronic orbits in an atom. However, in atomic structure, the nucleus provides the electrons with a central potential. There is no obvious center providing a potential for the nucleons. Instead, the potential seen by each nucleon is considered to be the sum of its interactions with all the other nucleons. A very simple approximation to this potential is a finite square well. However these simple assumptions do not lead to shells that close at the observed magic numbers. The independent-particle model must therefore be modified by the inclusion of spin-orbit forces which split degenerate

levels (25) and pairing energies which fill the levels in a way that then reproduces the observed properties of closed shell nuclei (25). The success of the shell model in reproducing observed spectra is taken as strong evidence supporting its basic hypotheses, i.e., that the nucleons in a nucleus move somewhat independently of one other, that the spin and orbital angular momentum of a nucleon are strongly coupled, and that there exists a large pairing energy. Although the shell model fails to explain the nuclear quadrupole moments and non-spherical shapes, it remains the basis upon which many other models are built. The existence of energy levels that are filled in pairs by nucleons and which are split by spin-orbit forces provides a framework from which other models can be developed. The shell model predicts the correct energy levels in very few nuclei, only those close to the magic numbers, N or $Z = 2, 8, 20, 28, 50, 82, 126$.

Kitching et al. (34) used a shell model effective-interaction method to calculate the levels in ^{82}Sr . They treated only the $1g_{9/2}$ and $2p_{1/2}$ neutron shells, truncating the model space because of lack of experimental information on the presence of particles or holes in other orbitals. The assumption was made that the $1f_{5/2}$ neutron and proton shells are essentially complete. The lower-level ordering of level spins was approximately correct (See Figure 3-1), but the energy relationships were not reproduced. At the time of submission of their paper, there were no experimental data on ^{82}Sr levels available.

Ogawa (35) calculated the energies of the low-lying levels in Sr nuclei assuming proton and neutron correlations. The proton closed shell is assumed to be $Z=40$, i.e., a ^{90}Zr core with two-proton hole states assuming a configuration of $(2p_{1/2}, 2p_{3/2}, 1f_{5/2})^{-2}$. The neutron

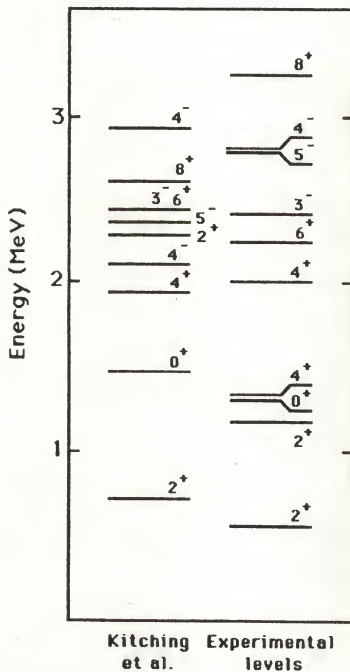


Figure 3-1. Comparison of ^{82}Sr experimental levels to shell model calculations by Kitching et al. (34).

hole states are measured from $N=50$, ^{88}Sr , and are restricted to the $1g_{9/2}$ hole orbit. His calculations reproduce the trend in neutron deficient Sr nuclei from shell model spectra to rotation-like spectra (See Figure 3-2). The agreement with experimental levels in ^{82}Sr is fair. The wavefunctions obtained show strong correlations between proton and neutron motions. Ogawa postulated that the proton and neutron configurations in ^{82}Sr show a tendency towards oblate deformation and their interactions correlate strongly to strengthen the deformation, causing a rotation-like spectrum of energy levels.

Experimental data on the neutron deficient strontium isotopes were reported by Ball et al. (17) who used (p,t) reactions to obtain the energy levels. Their comparison of their data to the above calculations of Kitching et al. (34) and Ogawa (35) indicated that a model space which included only the $2p_{1/2}$ and $1g_{9/2}$ neutron orbitals and required seniority conservation would not be able to reproduce the marked decrease in level spacing observed from ^{86}Sr to ^{82}Sr or the two 2^+ levels in ^{84}Sr (17). Observation of a number of 0^+ states and larger ground-to-ground state transition intensities in the (p,t) reaction data were additional evidence for the need for a larger set of basis states in shell-model calculations.

The thirty-eight protons in ^{82}Sr may fill a $Z=38$ sub-shell (36), but the forty-four neutrons are six neutrons away from the $N=50$ shell closure. Since the shell model works well only near closed shells, it is not expected to reproduce the observed energy levels in ^{82}Sr . The shell model assumes a spherical potential $V(r)$. As neutrons or protons are removed from closed shell nuclei, this assumption is no longer valid.

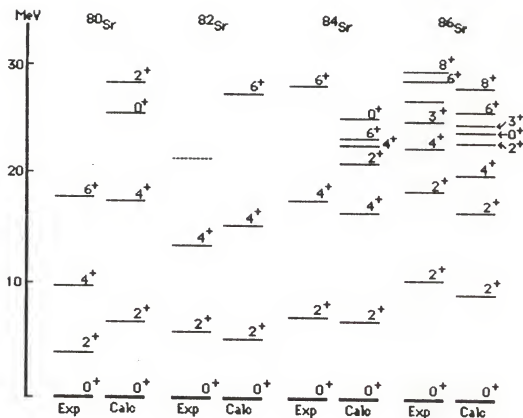


Figure 3-2. Comparison of experimental levels in ^{86}Sr , ^{84}Sr , ^{82}Sr and ^{80}Sr to shell model calculations by Ogawa (35).

Nilsson Model

Nilsson calculated the binding states of nucleons in a deformed potential (31). He used a single-particle Hamiltonian of the form

$$H = H_0 + C \vec{l} \cdot \vec{s} + D \vec{l}^2. \quad (3.1)$$

The first term, H_0 , is a harmonic oscillator potential, chosen for simplicity. The second term is a spin-orbit term that splits levels with different l -values. The third term is a correction term that depresses high angular momentum states (31). The result is a potential which is similar to an interpolation between the oscillator and the square well (31).

Because the potential is assumed to be cylindrical, only one parameter, δ , is needed to describe the deformation:

$$\omega_x^2 = \omega_0^2 (1 + \frac{2}{3} \delta) = \omega_y^2 \quad (3.2)$$

$$\omega_z^2 = \omega_0^2 (1 - \frac{4}{3} \delta). \quad (3.3)$$

The assumption that the nucleus has a constant volume requires that $\omega_x \omega_y \omega_z = \text{constant}$ and thus

$$\omega_0(\delta) = \omega_0 (1 - \frac{4}{3} \delta^2 - \frac{16}{27} \delta^3)^{-1/6} \quad (3.4)$$

where

$$\hbar \omega_0 = \hbar \omega_0(0) = 41 A^{-1/3} \text{ MeV}. \quad (3.5)$$

The two parameters used in the calculations are κ and μ , where

$$\kappa = -1/2 \left(\frac{C}{\hbar\omega_0} \right) \quad (3.6)$$

and

$$\mu = 2 \frac{D}{C} . \quad (3.7)$$

The sequence of particle orbitals is determined by μ , and the energy spread between orbitals is influenced by κ . The parameters κ and μ are chosen by requiring that the shell model orbital relationships be reproduced for $\delta = 0$.

The Nilsson Hamiltonian is often used to generate zeroth order internal wave functions for deformed nuclei. In particular, it is used in the calculation of the two-quasiparticle-plus-rotor model results reported in Chapter 4. The Nilsson wave functions as a function of δ for protons and neutrons in ^{82}Sr are shown in Figures 4-5 and 4-6 in Chapter 4.

Collective Models

The single-particle model may represent the spectra of nuclei near closed shells, but as nucleons are removed from a closed shell nucleus, evidence of the collective behavior of the nucleons is seen. The energy of the first excited state is lowered and the E2 decay rate from that level is much faster than would be expected for a single particle transition. There are two basic types of collective motion 1) vibrations about an equilibrium shape, and 2) rotations of a deformed

nucleus. For quadrupole excitations, the collective Hamiltonian does not refer to a specific nuclear model. Instead, the structure of the Hamiltonian is expressed geometrically in terms of the collective variables that describe the two types of motion described above (37). The collective variables consist of the three Euler angles of the body-fixed axes with respect to the space-fixed axes and the deformation coordinates, β and γ . In a non-spherical binding field the nuclear shape and orientation are considered dynamical variables (31). In a well-deformed nucleus, the nuclear motion can be divided into two approximately separate parts, the intrinsic nuclear motion relative to the deformed field and the collective rotational and vibrational motion.

Hydrodynamical Model

One of the most general collective models is the hydrodynamical model. The treatment of this model in the following sections follows the approach taken by Davidson in reference 38. In this theory of nuclear structure the nucleus is treated as a charged liquid drop. Excitations are explained in terms of oscillations about a spherical equilibrium shape. The deformations preserve volume since nuclear matter is considered essentially incompressible. If R_0 is the radius of the undistorted spherical nuclear surface then the radius vector can be expanded in spherical harmonics in either the laboratory frame (1) or the body-fixed frame (2):

$$(1) \quad R^L(\theta, \phi) = R_0 \left[\alpha_0 + \sum_{\lambda > 1, \mu} \alpha_{\lambda\mu}^* Y_{\lambda\mu}(\theta, \phi) \right] \quad (3.8)$$

$$(2) \quad R^B(\theta', \phi') = R_0 \left[a_0 + \sum_{\lambda > 1, \nu} a_{\lambda\nu}^* Y_{\lambda\nu}(\theta', \phi') \right] \quad (3.9)$$

where α_0 and $a_0 = 1$ to first order. The relationship between the laboratory and body-fixed coordinates is

$$\alpha_{\lambda\mu} = \sum_{\nu} D_{\mu\nu}^{\lambda*}(\theta_1) a_{\lambda\nu} \quad (3.10)$$

where the $D_{\mu\nu}^{\lambda}(\theta_1)$ are the $(2\lambda+1)$ -dimensional representations of the rotation group defined by Rose (39) and are functions of the Euler angles.

According to the classical theory of small oscillations, the $\alpha_{\lambda\mu}$ may be considered generalized coordinates so that the kinetic energy in the lab frame is

$$T^L = \frac{1}{2} \sum_{\lambda\mu} B_{\lambda\mu} |\dot{\alpha}_{\lambda\mu}|^2. \quad (3.11)$$

The potential energy consists of an attractive surface term and a repulsive Coulomb term and can be written

$$V = \frac{1}{2} \sum_{\lambda\mu} C_{\lambda\mu} |\alpha_{\lambda\mu}|^2. \quad (3.12)$$

The Lagrangian of the system can be used to define a momentum, $\pi_{\lambda\mu}$, conjugate to $\alpha_{\lambda\mu}$:

$$\pi = \frac{\partial}{\partial \dot{\alpha}} L = \frac{\partial}{\partial \dot{\alpha}} (T-V) = B \dot{\alpha}. \quad (3.13)$$

This leads to the Hamiltonian for the classical motion

$$H = \frac{1}{2} \sum_{\lambda\mu} \frac{1}{B_{\lambda}} |\pi_{\lambda\mu}|^2 + \frac{1}{2} \sum_{\lambda\mu} C_{\lambda} |\alpha_{\lambda\mu}|^2 = \sum_{\lambda} H_{\lambda}. \quad (3.14)$$

This Hamiltonian is just that for a system of uncoupled harmonic oscillators with frequency

$$\omega_{\lambda} = \left(\frac{C_{\lambda}}{B_{\lambda}} \right)^{1/2}. \quad (3.15)$$

The quantization of this theory may be approached in two different ways. A theory of quantized surface oscillations is based on the assumption that the number of nucleons outside the deformable core is small and therefore the zero point energy of the oscillations is greater than the energy of the deformation and the core shape. If the number of nucleons outside the core is larger and the zero-point energy of the oscillations is small compared to the energy of deformation, then the nuclear surface stabilizes about a deformed shape. The first case results in a vibrational model. The second case describes a deformed, almost rigid rotor.

Vibrational Model.

The predictions of the vibrational model are most nearly fulfilled in nuclei near closed shells. The energy levels are given by

$$E = E_0 + \sum_{\lambda\mu} \left(n_{\lambda\mu} + \frac{1}{2} \right) \hbar \omega_{\lambda}. \quad (3.16)$$

The lowest vibrational mode of interest is the quadrupole mode, $\lambda=2$, since the $\lambda=1$ mode simply represents the motion of the center of mass. Application of the above formulation to an even-even nucleus (i.e. one having an even number of both protons and neutrons) yields a ground state with spin and parity $I = 0^+$ with all nucleons paired. The

first excited state is $I = 2^+$, formed by the creation of a single quadrupole phonon. The creation of two quadrupole phonons is identified with three possible states with $I = 0^+, 2^+, 4^+$. Although in theory these states are degenerate, they are usually slightly separated due to perturbations not taken into account in the model. An octupole vibration ($\lambda=3$) will yield a 3^- state.

One characteristic of a vibrational nucleus is the presence of evenly spaced energy levels. Deviations from even spacing are usually attributed to anharmonicities. Other characteristics are given in Table III-1 where they are compared to the low-lying levels in ^{82}Sr . The predicted energy levels are compared to the experimental ones in Figure 3-3. It can be seen that ^{82}Sr appears to have vibrational properties through the 4^+ level. At higher spins other modes of excitation influence the level energies.

Rotational Model.

Far from closed shells the deformation energy is large compared to the vibrational energies and the system may be considered a stable, deformed rigid rotor. The Bohr-Mottelson model (26) assumes the nucleus is an axially symmetric ellipsoid and treats only the $\lambda=2$ quadrupole deformations.

An axially symmetric rotor has two equivalent axes, 1 and 2, about which the system can rotate. The 3-axis is the axis of symmetry. The applicable quantum numbers for the rotational states of a deformed nucleus are I , M , and K (26) (illustrated in Figure 3-4).

TABLE III-1
Comparison of Vibrational Model Predictions to ^{82}Sr Experimental Data

Prediction	Data
1. $\frac{E_2^+}{E_2} = 2.00$	$\frac{E_2^+}{E_2} = 2.05$
2. $\frac{B(E2, 4^+ \rightarrow 2^+)}{B(E2, 2^+ \rightarrow 0^+)} = 2.00$	$\frac{B(E2, 4^+ \rightarrow 2^+)}{B(E2, 2^+ \rightarrow 0^+)} = 2.34(55) \text{ (20)}$
3. Strong $B(E2, 2^+ \rightarrow 0^+)$	$B(E2, 2^+ \rightarrow 0^+) = 47(3)\text{WU (20)}$
4. Strong $B(E2, 2^{+'} \rightarrow 0^+)$ $B(E2, 0^{+'} \rightarrow 2^+)$ $B(E2, 4^+ \rightarrow 2^+)$	$B(E2, 2^{+'} \rightarrow 2^+)$ Strong (not measured) $B(E2, 0^{+'} \rightarrow 2^+)$ Very weak (not measured) $B(E2, 4^+ \rightarrow 2^+) = 110(25)\text{WU (20)}$
5. No crossover from E_2^+ to 0^+	$\frac{B(E2, 2^{+'} \rightarrow 0^+)}{B(E2, 2^+ \rightarrow 0^+)} = .009(2) \text{ (20)}$
6. Quadrupole moment of $E_2^+ = 0$.	Not measured.

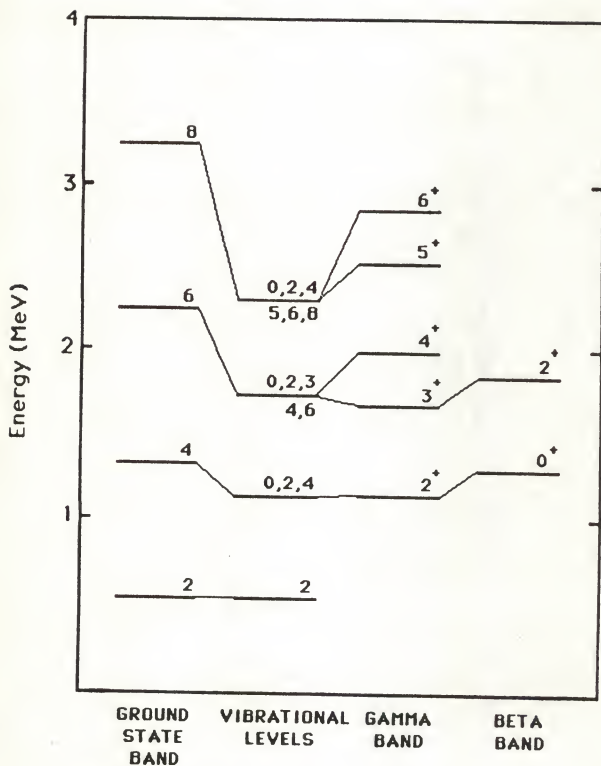


Figure 3-3. Comparison of predicted vibrational model levels for ^{82}Sr to experimental levels classified according to band structure (levels in beta band are taken from reference 20).

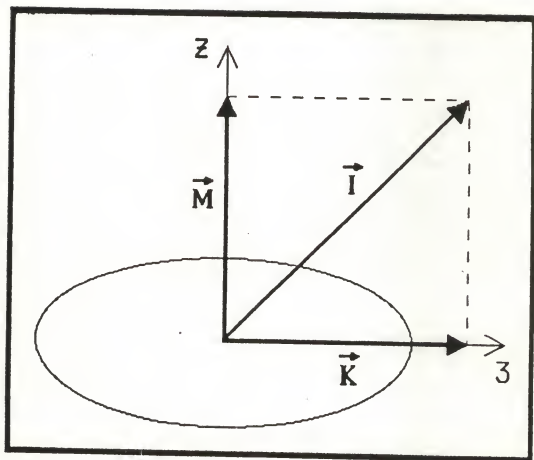


Figure 3-4. Angular momentum projection for an axially symmetric rotor.

1. I is the total angular momentum of the system.
2. M is the projection of I on the space-fixed axis, $M = I_z$.
3. K is the projection of I on the body-fixed axis, $K = I_3$.

There are two basic types of even parity vibrations in even-even nuclei:

1. Beta-vibrations are oscillations around an equilibrium value while maintaining axial symmetry; $K=0^+$.
2. Gamma-vibrations are oscillations away from axial symmetry; $K=2^+$.

Figure 3-5 illustrates the gamma and beta vibrations with respect to the body-fixed axes. On the left are the cross sections perpendicular to the 3-axis. The diagrams on the right hand side show the cross section in the 2-3 plane. The arrows indicate the direction of rotation for a rotational state. The relationship between the body-fixed coordinates, $a_{\lambda\mu}$, and the deformation coordinates β and γ , is

$$a_{20} = \beta \cos \gamma \quad (3.17)$$

$$a_{22} = \frac{1}{\sqrt{2}} \beta \sin \gamma. \quad (3.18)$$

The potential energy surface of a quadrupole excitation can be expressed graphically in terms of the β and γ coordinates in the β - γ plane (40). In Figure 3-6 (a) the β coordinate is measured in distance from the origin. The γ coordinate is measured in degrees from 0° to 60° . For $\gamma = 0^\circ$, the nucleus has an axially symmetric prolate shape with the axis of symmetry along the 3-axis. An oblate nucleus with an axis of symmetry along the 2-axis has a $\gamma = 60^\circ$. A spherical nucleus is

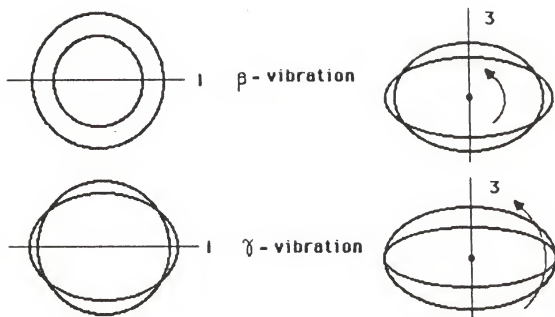


Figure 3-5. Even parity vibrations in an even-even nucleus (40).

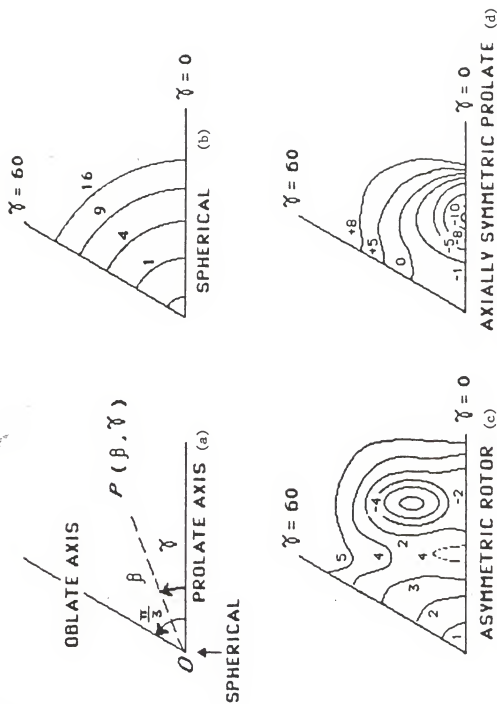


Figure 3-6. Potential energy surfaces (40).

represented by a point at the origin. The relationship between the models discussed so far [vibrational (spherical) and rotational (axially symmetric and asymmetric)] and their respective potential energy surfaces is shown in Figures 3-6(b) through 3-6(d).

The energy levels in a rotational band can be compared to the eigenvalues of a rotating symmetric top with constant K . If $\mathfrak{J}_1 = \mathfrak{J}_2 = \mathfrak{J}_0$ and $\mathfrak{J}_3 = 0$, the eigenvalues are

$$E_I = \frac{\hbar^2}{2\mathfrak{J}_0} I(I+1). \quad (3.19)$$

As the nucleus rotates, centrifugal stretching causes the moment of inertia, \mathfrak{J}_0 , to increase and therefore $E(I)$ to decrease slightly. For the $K = 0$ ground state bands, these energies can now be expressed as

$$E_I = \frac{\hbar^2}{2\mathfrak{J}_0} I(I+1) - bI^2(I+1)^2 \quad (3.20)$$

where b is positive.

These relationships are compared to the experimental levels of ^{82}Sr in Figure 3-7. The level energies in ^{82}Sr do not increase with spin as fast as the levels predicted by the simple rigid rotor model. When centrifugal stretching is taken into account, with $\hbar^2/2\mathfrak{J}$ and b determined from the 2^+ and 4^+ level energies, the second term begins to dominate at spin 8^+ and the energies become negative. The centrifugal stretching model does not seem to be an appropriate one to explain the level scheme of ^{82}Sr .

According to the rotational model, the transition probability for a quadrupole transition is defined as a function of the deformation, β :

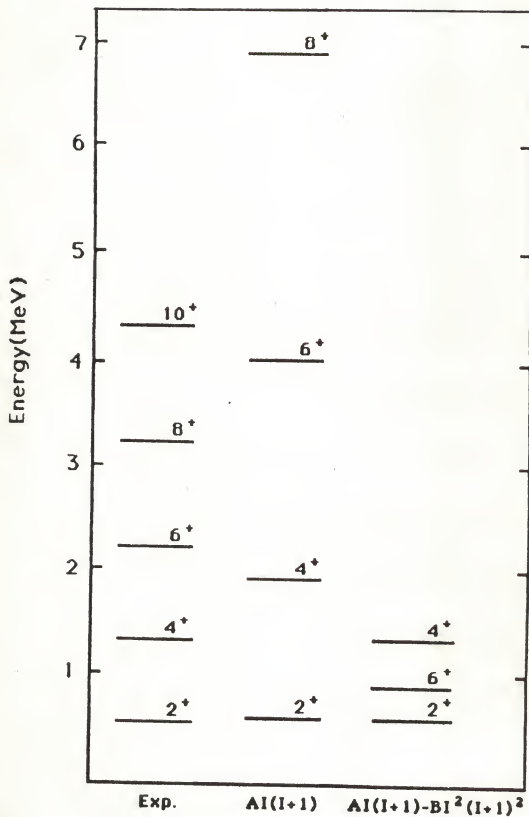


Figure 3-7. Comparison of predicted rotational model energy levels for ^{82}Sr to the experimental levels.

$$B(E2; J+2+J) = .0854 Z^2 R_0^4 \beta^2 \frac{(J+1)(J+2)}{(2J+3)(2J+5)} . \quad (3.21)$$

If this formula is applied to ^{82}Sr with the value of the

$B(E2, 2^+ \rightarrow 0^+) = 1000(50) e^2 \text{fm}^4$ which was measured by Dewald (20), the value of β is calculated to be .287(7).

In a system without spherical symmetry, there is often a rotational band associated with each intrinsic state. The remarkable thing about rotational bands is that each different intrinsic configuration may have a very different moment of inertia. In even-even nuclei the moments of inertia change smoothly from nucleus to nucleus. But in odd A nuclei the moments of inertia are systematically larger than in the neighboring even-even nuclei and they often vary quite dramatically for different intrinsic configurations (41).

Although the ground state band level spacings in ^{82}Sr increase smoothly with spin as expected for a rotational nucleus, they are not well fitted by the simple rigid rotor relationships. One of the problems is that these relationships assume that the moment of inertia, \mathcal{I}_0 , is unchanged as the spin increases. This is not necessarily the case.

The moment of inertia is related to the spin, energy, and frequency of rotation of a rotating body by the following equations:

$$E(I) = \frac{\hbar^2}{2\mathcal{I}} I(I+1) = \frac{1}{2} \mathcal{I} \omega^2 \quad (3.22)$$

where the frequency

$$\hbar\omega(I) = \frac{\partial E}{\partial I} = \frac{1}{2}[E(I+1) - E(I-1)] = E_V/2. \quad (3.23)$$

The moment of inertia is usually defined through the measured quantity,

$$AE(I, I-2) = \hbar^2 \frac{4I-2}{2g}. \quad (3.24)$$

The assumption that a rotating nucleus is a rigid body yields moments of inertia that are too large. An attempt to explain the rotational motion of the nucleus as the irrotational flow of a hydrodynamical system results in a moment of inertia that is four to five times too small. Obviously the rotational motion of the nucleus is complex, with irrotational flow superimposed on the collective motion of the whole nucleus, which is added to single-particle alignment to give a total angular momentum. Plots of moment of inertia vs. angular frequency have been valuable tools for seeing that changes in rotational behavior were occurring in a nucleus. For example, the relationships between the moment of inertia and the angular frequency are given in Figure 3-8 for some of the models discussed in this chapter. An ideal rotor has a constant moment of inertia. An ideal vibrator does not rotate, or rotates with a constant frequency of rotation. In the variable moment of inertia (VMI) model, discussed in the following sections, the moment of inertia varies linearly with rotational frequency. The plot for most nuclei is more complex. For example, the bands in ^{82}Sr shown in Figure 3-9, exhibit the characteristic behavior of all three models. The meaning of this behavior is discussed in Chapter 4.

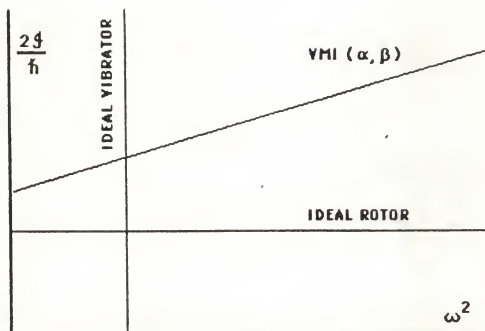


Figure 3-8. Moment of inertia vs. angular frequency for some simple nuclear models.

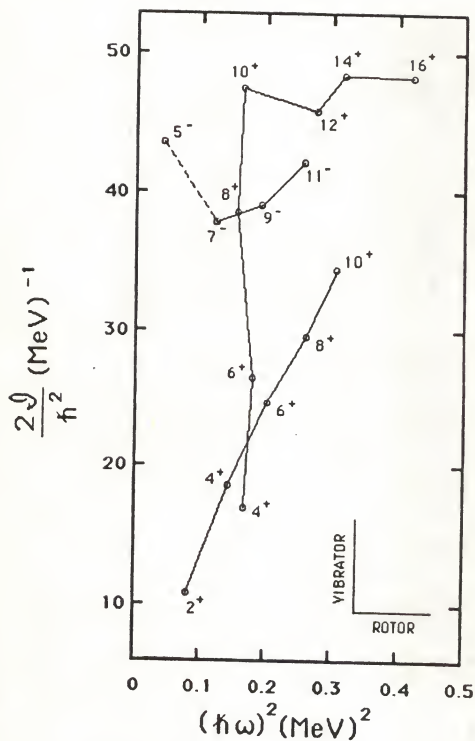


Figure 3-9. Moment of inertia vs. angular frequency for the bands in ^{82}Sr .

Cranking

Many of the fully microscopic theories of nuclear rotation are based on, or related to, some version of Inglis's Cranking Model (42). Basically this model assumes that the rotating nuclear many-body system can be described in terms of independent, non-interacting particles contained in an external potential well that is rotating. The energy of the system is calculated as a function of the angular velocity of the potential. The Hamiltonian for such a system is $H_\omega = H(0) - \omega L_z$. The second term, $-\omega L_z$, contains both the Coriolis and the centrifugal forces of the rotating frame. $H(0)$ is the motion in a non-rotating frame. The energy is $E = E_0 + \frac{1}{2} \mathcal{J} \omega^2$.

In an attempt to model the deviations from rigid rotor predictions, Harris (43) proposed an expansion in ω^2 :

$$E = 1/2 \omega^2 (\mathcal{J}_0 + 3C\omega^2 + 5D\omega^4 + \dots) \quad (3.25)$$

$$I = \omega \mathcal{J}_0 = \omega (\mathcal{J}_0 + 2C\omega^2 + 3D\omega^4). \quad (3.26)$$

If $[I(I+1)]^{1/2}$ is substituted for I , this expansion gives good results up to about $I = 14$.

Variable Moment of Inertia Model

An equivalent result is obtained with the variable moment of inertia (VMI) model of Mariscotti, Scharff-Goldhaber, and Buck (30) which also leads to

$$\mathcal{J} = \mathcal{J}_0 + 2C\omega^2. \quad (3.27)$$

The VMI equation for the energy of a state with spin I is

$$E_I(\mathcal{J}) = \frac{1}{2} C(\mathcal{J} - \mathcal{J}_0)^2 + \frac{1}{2} \frac{I(I+1)}{\mathcal{J}} \quad (3.28)$$

where
$$\frac{1}{2} C(\mathcal{J} - \mathcal{J}_0)^2 \quad (3.29)$$

is the potential energy and

$$\frac{1}{2} \frac{I(I+1)}{\mathcal{J}} \quad (3.30)$$

is the rotational energy.

The equilibrium condition of $\partial E(\mathcal{J})/\partial \mathcal{J}_0 = 0$ gives \mathcal{J}_I . The ground state moment of inertia is \mathcal{J}_0 and C is the stiffness parameter. The two parameters, \mathcal{J}_0 and C , are fitted with the energies of E_2^+ and E_4^+ from the experimental spectrum. The stiffness is a measure of resistance to deformation. Its reciprocal is the softness parameter, σ , which measures the relative initial variation of \mathcal{J} with respect to I ,

$$\sigma = \left[(1/\mathcal{J})(d\mathcal{J}/dI) \right]_{I=0} = 1/2C\mathcal{J}^3. \quad (3.31)$$

The range of validity in the deformed region is determined from the limits on σ .

$$R_I(\sigma=0) = 1/6 I(I+1) \quad (3.32)$$

$$R_I(\sigma \rightarrow \infty) = [1/6 I(I+1)]^{2/3} \quad (3.33)$$

where

$$R_I = E_I/E_2 + \quad R_4(\sigma \rightarrow \infty) = 2.23 \quad R_4(\sigma=0) = 3.33. \quad (3.34)$$

Therefore, this approach to relating the spin, energy, and moment of inertia is valid for

$$2.23 < R_4 < 3.33. \quad (3.35)$$

Outside of this region, more general forms of the VMI can be applied. Bonatsos and Klein (44) propose a general five parameter formula that can be reduced for special cases to

1. A three parameter variable anharmonic vibrator model (VAVM)

$$E(I) = aI + \frac{1}{3} I(I-2) + \frac{1}{2} C[\mathcal{J} - \mathcal{J}_0]^2, \quad (3.36)$$

2. A three parameter generalized VMI model (GVMI) which reduces to the VMI model for $X = 1/3$,

$$E(I) = \frac{I+XI(I-2)}{3} + \frac{1}{2} K[\mathcal{J} - \mathcal{J}_0]^2. \quad (3.37)$$

The ground state band of ^{82}Sr can be described by the VMI model. The fit to each of these models, VMI, VAVM, and GVM are listed in Table III-2. In the VMI fit, the first two levels are used to determine the parameters. In VAVM and GVMI, the parameters are fitted to the first three levels. The number DE_1 is a measure of the goodness of fit. It is determined by the summation of the absolute values of the differences between the calculated and experimental values for $J \geq 8$ and division by n , the number of energies not used in the fit. In the one

TABLE III-2
Experimental and Theoretical Energies of the Ground
State Band of ^{82}Sr for a Generalized VMI Model

	EXP.	VMI	VAVM	GVM
E_2	.5736	-	-	-
E_4	1.3285	-	-	-
E_6	2.2292	2.215	-	-
E_8	3.2426	3.203	3.243	3.253
E_{10}	4.3502	4.277	4.347	4.383
E_{12}		5.424	5.528	5.607
E_{14}		6.637	6.773	6.917
E_{16}		7.909	8.077	8.305
E_{18}		9.235	9.432	9.764
DE_1		.0561	.0002	.0244

hundred fifty nuclei tabulated by Bonatsos and Klein in reference 44 the fit of the VAVM model to ^{82}Sr had the lowest DE_2 .

Asymmetric Rotor.

The deviation of the ^{82}Sr levels from the predictions of the rigid rotor model may indicate that the assumptions of the model are not completely valid for this nucleus. The model assumes a rigid nucleus with axial symmetry. A comparison of the ^{82}Sr energy levels to the predictions of the asymmetric rotor model of Davydov and Filippov (45) indicates that ^{82}Sr may not be axially symmetric.

Davydov and Chaban (46) investigated the collective excitations of even nuclei and included both the rotational and vibrational excitations. They modified the earlier model of Davydov and Filippov (45) which assumed that β and γ were fixed by assuming the nucleus was rigid for γ vibrations but not for β vibrations. For a given K and I , the energy of the excited states is expressed only through the 'non-adiabaticity' parameter, μ , and the 'non-axiality' parameter, γ . The non-adiabaticity parameter, μ , is a measure of how rigid the nucleus is to vibrations. A rigid nucleus has $\mu=0$ and the nucleus becomes softer as μ approaches 1.0. For $\mu > .5$ the nucleus is soft; rotational and vibrational motions should be separable.

They introduce the ratios

$$R_{k1}(I) = \frac{E_{kv_1}(J) - E_{1v_1}(0)}{E_{1v_1}(2) - E_{1v_1}(0)} \quad \text{and} \quad R_{k2}(I) = \frac{E_{1v_2}(0) - E_{1v_1}(0)}{E_{1v_1}(2) - E_{1v_1}(0)} \quad (3.38)$$

where the k refers to the number of the energy level $E_k(I)$. In Figures 3-10(a) and (b) the values of $R_{11}(4)$ and $R_{11}(6)$ are plotted as functions of $R_{21}(2)$, the ratio of the first two 2^+ levels, as a function of μ and γ . In Figure 3-10(c) the values for the ratio of the difference between the first excited 0^+ state and the energy of the first excited 2^+ and the energy of the first excited 2^+ state are plotted against $R_{21}(2)$ as a function of μ and γ . For ^{82}Sr the values of these ratios are

1. $R_{11}(4) = 2.32,$
2. $R_{21}(2) = 2.05,$
3. $R_{11}(6) = 3.89,$
4. $R_{12}(0) = 2.29.$

A graphical solution for the values of γ and μ for ^{82}Sr according to this model yields $\gamma = 22.5^\circ$ and $.5 < \mu < .66$. These values indicate a soft, non-axial shape. Other predictions of this model with respect to ^{82}Sr are given in Table III-3.

The results of the model of Davydov and Chaban's modified asymmetric rotor (46) are very similar to the results obtained with an axially symmetric model which includes rotation-vibration coupling (40). A nucleus which oscillates about axial symmetry with a rms value, γ_0 , would have collective levels which are very similar to those of an asymmetric rotor with an asymmetry of γ_0 (40).

Interacting Boson Model

An alternative description of collective quadrupole states of nuclei in terms of boson variables was proposed by Arima and Iachello (47). The following overview of the model follows the review by Arima

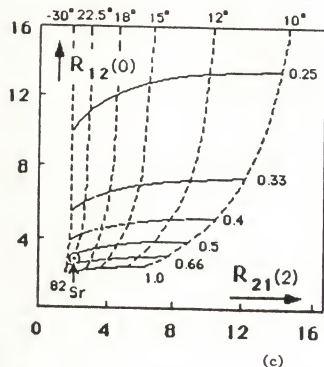
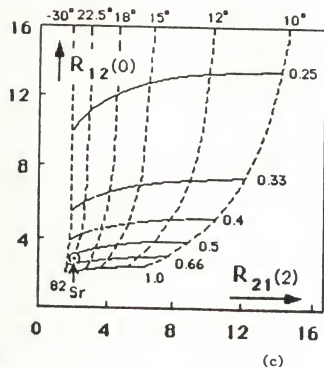
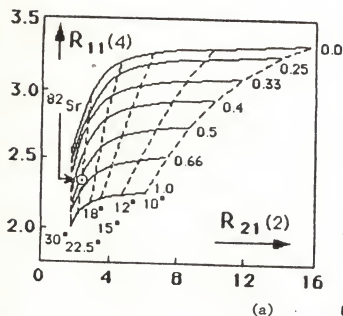


Figure 3-10. Graphical solution for γ and μ in ^{82}Sr based on the asymmetric rotor model.

TABLE III-3

Comparison of the Predictions of the Asymmetric Rotor Model
To ^{82}Sr Data

Prediction of the Model	^{82}Sr Results
1. Two states with $I=0$ ($K=0$)	Three seen (17)
2. No possible state for $I=1$	None seen
3. Two states with $I=2^+$ ($K=0,2$)	Yes
4. One state with $I=3^+$ ($K=2$)	Yes
5. Three states with $I=4$ ($K=0,2,4$)	Only two seen
6. $E_2 + E_2' = E_3$	$573.64 (01) + 1175.78 (01) =$ $1749.42 (01)$ $E_3 = 1689.37 (05)$ $\% \text{ error} = 3.4\%$

and Iachello in reference 48. Their interacting boson model (IBM) uses five quadrupole variables with $I=2$ (the d boson) and adds a sixth variable, a scalar boson (the s boson) with $I=0$ which describes the pairing correlations. The s and d bosons are interpreted as pairs of nucleons coupled to angular momentum $I=0$ and $I=2$. In IBM-I the nucleon pairs are not differentiated. IBM-II explicitly introduces protons ($s_{\pi} d_{\pi}$) and neutron ($s_{\nu} d_{\nu}$) bosons.

The low-lying collective quadrupole shapes are generated by a system of N bosons occupying two levels, one with angular momentum $I=0$ and the other with $I=2$. In IBM-I N is taken as a parameter. In IBM-II the total number of bosons, $N = N_{\pi} + N_{\nu}$, where N_{π} and N_{ν} are assumed constant. It is assumed that the structure of these states is dominated by excitation of the valence particles. The number of bosons is counted from the nearest major closed shell. For the light strontium nuclei, the major closings are $N=50$ and $Z=28$. There are eight bosons in ^{82}Sr , five proton bosons and three neutron-hole bosons.

The difference between the IBM and the Bohr-Mottelson collective model is in the mathematical approach each takes. The IBM uses quantum variables and the Bohr-Mottelson model uses classical variables. Defining the correspondence between the two approaches requires taking the classical limit of a quantum system. The advantage of the IBM over the Bohr-Mottelson model is that the solutions of the IBM are algebraic and are therefore simpler than the solutions of the differential equations of the Bohr-Mottelson model. The application of group theoretical techniques to the study of the physical properties of the nucleus points out the dynamical symmetries in nuclear spectra (48).

The IBM-II takes into account explicitly the neutron and proton degrees of freedom, inferring a connection between the collective model and the spherical shell model. Both the quadrupole and pairing correlations are included in one theoretical framework (48).

Application of the IBM works best in medium-mass and heavy nuclei ($A > 80$) with at least two pairs away from close shells. The model predicted spin limit is $I = 2N$. At that spin one sees the excitation of particles not in the valence shell and some pairs couple to angular momentum $I \neq 0$ or 2 , requiring the inclusion of hexadecapole (g) bosons.

The IBM-I model was used to calculate the energy levels in ^{82}Sr by Bucurescu et al. (27). They used the program package PHINT. The Hamiltonian they diagonalized was

$$H = E_n^{\hat{d}} + \sum_{L=0,2,4} \frac{1}{2} \sqrt{2L+1} C_L [(d^{\dagger} \times d^{\dagger})^{(L)} \times (\tilde{d} \times \tilde{d})^{(L)}]_0^{(0)} \quad (3.39)$$

$$+ \frac{1}{2} v_2 [(d^{\dagger} \times d^{\dagger})^{(2)} \times (\tilde{d} \times s)^{(2)}]_0^{(0)} + \frac{1}{2} v_0 [(d^{\dagger} \times d^{\dagger})^{(0)} \times (s \times s)^{(0)}]_0^{(0)}.$$

Two of the parameters, C_0 and v_0 were held constant and the other four were allowed to vary smoothly with N . The fits were compared to the ground state band and the quasi-gamma band (see Figure 3-11). The ground state band was well fitted to spin 8^+ . The 0^+ and 2^+ states were predicted in the proper position but are probably not identified with the experimental states (27).

Dewald et al. (20) used the simplified version of the IBM-II Hamiltonian to calculate the energy levels and $B(E2)$ values for ^{82}Sr .

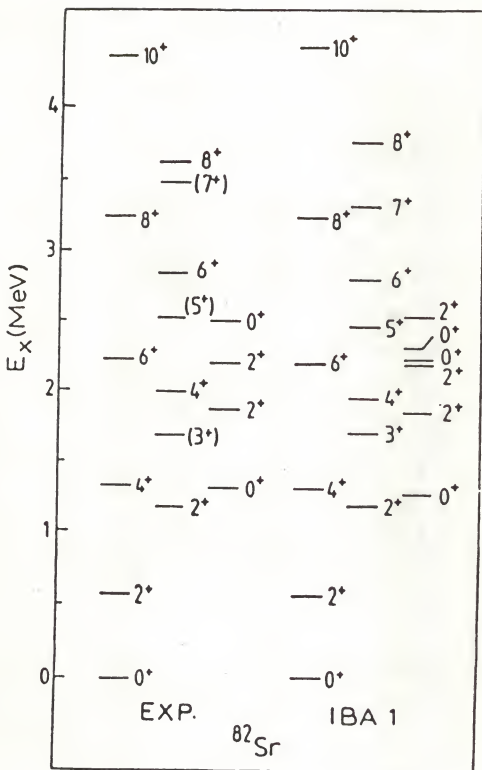


Figure 3-11. Comparison of IBM-I predictions to ^{82}Sr levels (27).

$$H = \epsilon(n_{d\pi} + n_{dv}) + \kappa Q_v^{(2)} \cdot Q_\pi^{(2)} + aM_{\pi v}. \quad (3.40)$$

In this model, the first term in the Hamiltonian describes the independent motion of the bosons, producing a harmonic energy spectrum. The second and third terms are the proton-neutron interaction terms. The second term describes the quadrupole-quadrupole force and the third term is a Majorana-type (49) exchange force. The strengths of the two forces are represented by the parameters κ and a . Since the $Q_{\pi,v}$ are a linear combination of two terms, there are two additional parameters ($X_{\pi,v}$) that determine the quadrupole force. The "Majorana" term is included to improve the position of the unnatural parity levels.

In his calculations, Dewald (20) kept a and X_π constant. A linear variation of X_v with neutron number was made and ϵ and κ were allowed to vary. The agreement is good in the ground state band and the quasi-gamma band is fairly well represented to spin 7^+ (Figure 3-12).

Heyde et al. (28) calculated the excited states of the even-even strontium nuclei with the IBM-II and paid particular attention to a systematic study of the parameters ϵ , κ , X_π and X_v . The results of their fit are presented in Figure 3-13.

Other authors who have used the IBM to calculate the collective levels in ^{82}Sr are Fields et al. (18) and Higo et al. (19). The results are similar to those already presented.

In all of the IBM fits to the strontium data, the experimental levels correspond well to the theoretical levels in the ground state band and the lower states in the first excited positive parity band. These states are expected to be collective in nature because of the

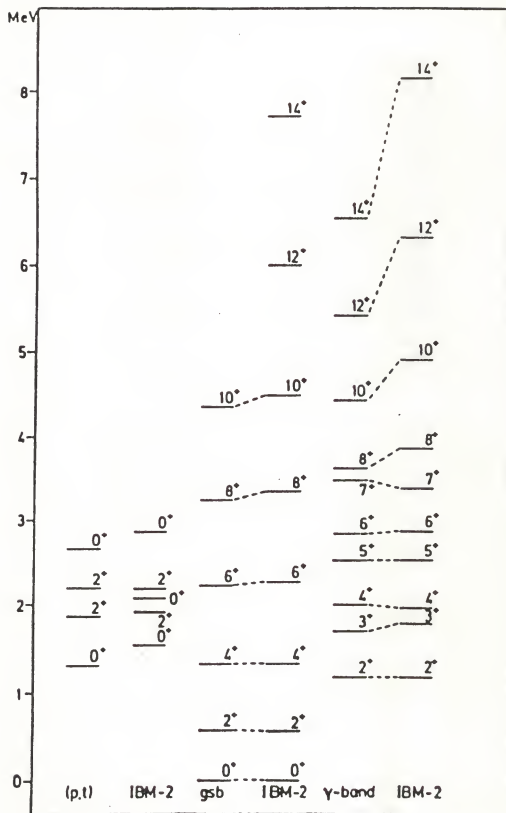


Figure 3-12. Comparison of IBM-II predictions to ^{82}Sr levels (23).

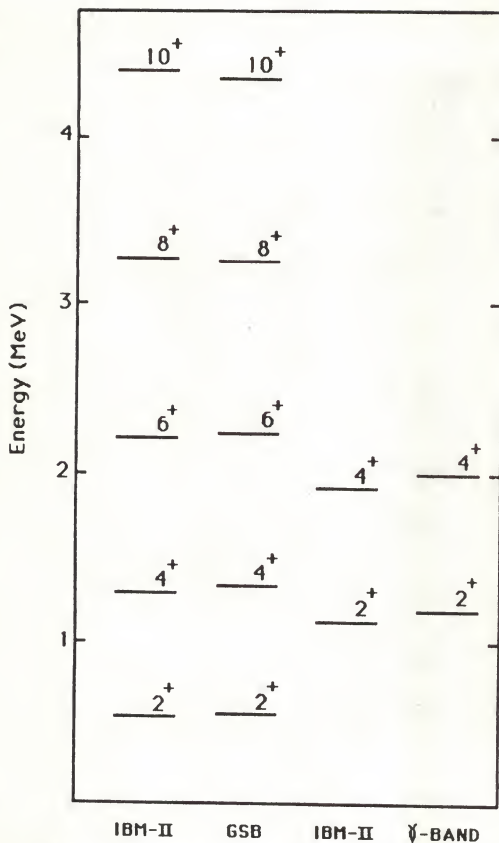


Figure 3-13. Comparison of IBM-II predictions to ^{82}Sr levels (28).

large transition probabilities connecting them and transition energies that are lower than those expected for single particle transitions. The model and experimental levels begin to disagree at spin $I=8^+$ in both bands. It is at that point that noncollective or intrinsic excitations begin to influence the energy levels.

Quasiparticles

These intrinsic excitations are due to the creation of quasiparticles. In the ground state configuration of an even-even nucleus, all nucleons are paired and occupy the $N/2$ lowest available states. The Fermi energy, λ , is the energy of the highest filled level. When one of the particles is excited into an orbital above the Fermi level, a two-quasiparticle (2-qp) state is produced (see Figure 3-14). A quasiparticle consists of a particle-hole pair in which the particle state has an amplitude of U and the hole state has an amplitude of V and $U^2 + V^2 = 1$. The binding energy of the nucleon pairs causes an energy gap of 2Δ that separates the fully paired ground state of an even-even nucleus from the lowest excited state involving the two quasiparticles obtained from the breaking of a pair. The energies of the two-quasiparticle levels are

$$E_K(I) = E_{v_1} + E_{v_2} + \frac{\hbar^2}{2J} [I(I+1) - K^2] \quad (3.41)$$

where

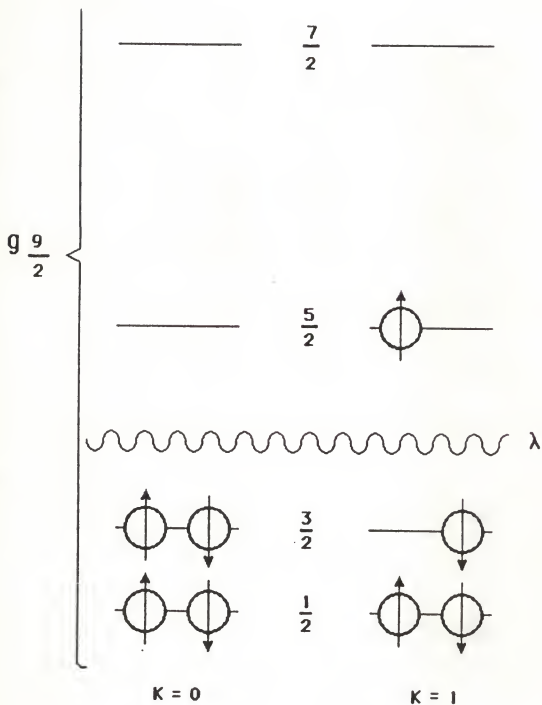


Figure 3-14. Placement of particles in the $g_{9/2}$ orbital of a doubly even nucleus (2).

$$E_{v_1} = \sqrt{(\epsilon_v - \lambda)^2 - \Delta^2} \quad (3.42)$$

is the quasiparticle energy and ϵ_v is the single particle Nilsson eigenvalue.

These two-quasiparticle excitations interact with the collective states in two ways:

1. They couple to the intrinsic deformation of the nucleus (strong coupling);
2. They interact with the rotations through the Coriolis and centrifugal forces (decoupling).

In a highly deformed nucleus the first interaction dominates. But in transitional nuclei the second effect becomes more pronounced and the Coriolis force influences the motion of the quasiparticles, aligning their angular momenta with that of the core. This results in the yrast states with large spins seen in (HI,xn) reactions (50).

Mottelson and Valatin (51) predicted that at a sufficiently high rotational frequency the pairing correlations would be eliminated and a phase transition would occur analogous to the destruction of superconductivity in a strong magnetic field, the Meissner effect. This effect is referred to as Coriolis anti-pairing (CAP). At high enough spins the moment of inertia would be equal to the rigid body value obtained with the cranking model. However, in a superconductor the electrons move in a highly degenerate conduction band and the superconductivity depends on this degeneracy. Nucleons are bound in single particle orbits separated by energies comparable to the pairing

energies. The sudden coherent breakdown of pairing is less likely; equally likely is the possibility that one or two pairs are broken at a time (29).

Quasiparticle-Plus-Rotor Model

Coriolis decoupling is the basis for the development of the two quasiparticle-plus-rotor bandmixing calculations developed by Flaum and Cline (29). The coupling of angular momenta for the two quasiparticle-plus-rotor system is defined in Figure 3-15. The particle in orbits j_1 and j_2 are coupled to an axially symmetric core rotating with angular momentum \vec{R} .

The Hamiltonian is

$$H = H_0 + \hbar^2 \vec{R}^2 / 2\mathcal{I} \quad (3.43)$$

$$\vec{R} = \vec{I} - \vec{J} \quad (3.44)$$

$$\vec{J} = \vec{j}_1 + \vec{j}_2 \quad (3.45)$$

$$H_0 = H_{sp}(1) + H_{sp}(2) + H_{int} \quad (3.46)$$

H_{sp} = the single particle Hamiltonian

H_{int} = the residual two-body Hamiltonian

H_{rot} = the rotational Hamiltonian

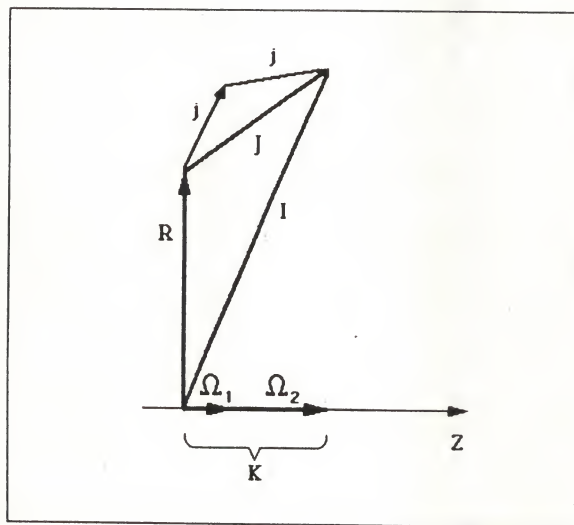


Figure 3-15. Coupling of angular momenta for the two-quasiparticle-plus-rotor system (2).

$$H_{\text{rot}} = \hbar^2 K^2 / 2\mathcal{J} = \hbar^2 / 2\mathcal{J} \{ [I(I+1) - K^2] - [\hat{I}_+ \hat{J}_- + \hat{I}_- \hat{J}_+] + [(\hat{J}_1^2 - \hat{n}_1^2) + (\hat{J}_2^2 - \hat{n}_2^2) + (\hat{J}_{1+} \hat{J}_{2+} + \hat{J}_{1-} \hat{J}_{2-})] \} \quad (3.47)$$

$$\hat{I}_{\pm} = \hat{I}_x \pm i\hat{I}_y \quad \hat{J}_{\pm} = \hat{J}_x \pm i\hat{J}_y \quad (3.48)$$

The first term of the rotational Hamiltonian is the rotational energy. The second term is the Coriolis term which includes the particle-rotor coupling. The last term is the two particle analog of the 'recoil' term and is usually ignored in one-particle calculations since it is much smaller than the particle-rotor coupling term for high spin states (29).

The residual interaction between the valence nucleons and the core nucleons is accounted for by the assumption of the pairing interaction and the BCS approximation (52), i.e., by a transformation to quasiparticles. The single particle states are computed with the Nilsson Hamiltonian and the ground state band is fitted with the variable moment of inertia model. The comparison of this model to the ^{82}Sr data is discussed in detail in Chapter 4.

Cranked Shell Model

The approach of the cranked shell model (32) allows one to separate the aligned angular momentum of the quasiparticles from the angular momentum of the core. The frequency is defined as

$$\hbar\omega(I) = \frac{dE(I)}{dI_x(I)} = \frac{E(I+1) - E(I-1)}{I_x(I+1) - I_x(I-1)} \quad (3.49)$$

The alignment of the angular momentum along the rotation axis, I_x , is given by

$$I_x(I) = \sqrt{(I + 1/2)^2 - K^2}. \quad (3.50)$$

The energy in the rotating frame of reference can then be expressed as

$$E'(I) = \frac{1}{2} [E(I+1) + E(I-1)] - \omega(I) \cdot I_x(I). \quad (3.51)$$

The single-particle energies and aligned angular momentum are

$$e'(\omega) = E'(\omega) - E_r(\omega) \quad (3.52)$$

$$i(\omega) = I_x(\omega) - I_r^*(\omega) \quad (3.53)$$

where E_r and I_r^* are reference configurations which have little or no aligned angular momentum.

Application of the cranked shell model to the first excited positive parity band by Funke et al. (5) is used to explain the crossing of a two-quasiparticle band with both the quasi-gamma band and the ground state band. A detailed discussion of this approach is included in Chapter 4 in the discussion of the positive parity band.

CHAPTER IV RESULTS AND DISCUSSION

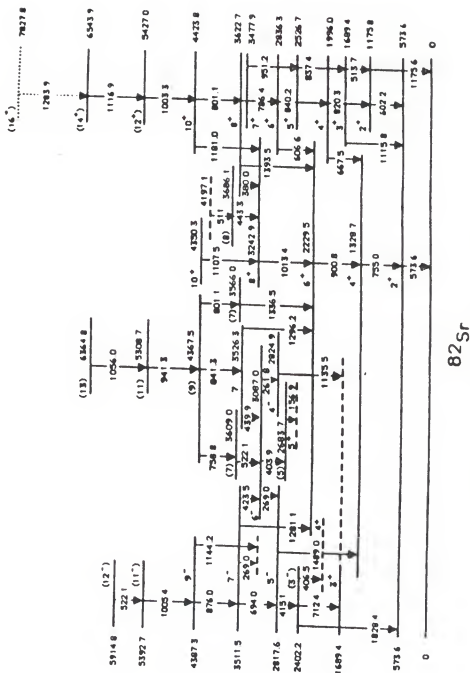
Level Scheme

The level scheme of ^{82}Sr determined from the coincidence measurements is shown in Figure 4-1. The decay of the excited residual nucleus proceeds through cascades of gamma rays that form three main bands as described in Chapter I. There is a negative parity band, a positive parity band based on the 2^{+1} excited state, and the yrast, or ground state, band. A possible fourth band may be another negative parity band. Other levels are not immediately identifiable as members of a band.

The variation of energy with spin for each band is seen in Figure 4-2. The smooth behavior of the energy-spin relationship is characteristic of band structure. The slight deviation of that smooth behavior for the positive parity band at spin 8^{+} may indicate the crossing of two bands, a point which is discussed later in this chapter.

Ground State Band Levels

The levels of the ground state band are well established through the present and other measurements (17-20) with only slight differences in energy among the various measurements. (See Table II-7). The energy, spin and parity results for the levels at 573.6 (2^{+}), 1328.7 (4^{+}), 2229.5 (6^{+}), and 3242.9 (8^{+}) keV agree with previously published values (17-20).

Figure 4-1. Level scheme for ^{82}Sr .

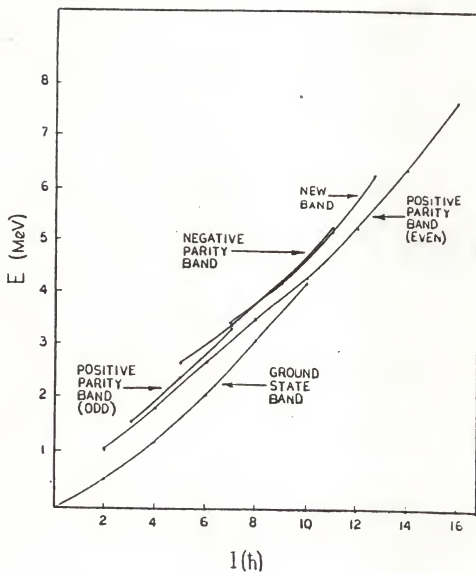


Figure 4-2. Energy vs. spin for ^{82}Sr .

The transition de-exciting the 4350.3 keV level is very weak (see Table 2-8 for relative intensities). The statistics in both the angular distribution and polarization measurements were not sufficient for a determination of the spin and parity. The assignment of $I = 10^+$ is based on previous reports (18-20) and systematics.

Positive Parity Band Levels.

The 1175.8 keV level is depopulated by two gamma rays. The most intense one is the 602.2 keV transition which decays to the 2^+ level in the ground state band. The angular distribution of this gamma ray requires a ΔI of 0 and the polarization measurements indicate no change of parity between the initial and final states. A closer look at this gamma ray is warranted. The intensity ratio between the 1175.6 keV transition to the ground state and the 602.2 keV transition is 0.22(09) in the 820.3 keV gate and 0.13(01) in the singles measurements averaged over the five angles of the angular distributions. Although the ratio between these two numbers is not statistically significant (1.69 ± 0.70), there may be an indication that the 602.2 keV gamma ray represents an unresolved doublet. Other factors which reinforce this possibility are 1) the energy relationships and 2) the feeding into the 573.6 level. The energy of the 1175.8 level is based on the energy sum: $602.15 (01) + 573.64 (01) = 1175.79 (01)$. However, the gamma ray which feeds the ground state has an energy of 1175.64 (05) keV. The sum of the relative intensities of the gamma rays which directly feed the 573.6 keV level should equal 100%. Instead it equals $121.2 \pm 3.4\%$. The problem can be traced to three of the four gamma rays which feed the 573.6 keV level. As much as 20% of the intensity of the 755.0 keV gamma

ray may be due to a ^{79}Rb contaminant. The 1115.8 keV gamma ray is part of a triplet, so the relative intensities of the members of the triplet are not well-defined. However, there is still the possibility that part of the intensity of the 602.2 gamma ray belongs to a transition other than $2^{+} \rightarrow 2^{+}$. There is no evidence for contamination from other isotopes in the 602.2 keV gates, but there may be a possible placement of a 602.7 keV gamma ray in the ^{82}Sr level scheme. The evidence is not strong enough to make any claims at this time.

The level at 1689.4 keV is assigned a spin and parity of 3^{+} based on the angular distribution of the 1115.8 keV gamma ray which de-excites this level and systematics. The other gamma ray which depopulates this level is one with an energy of 513.7 keV. Data collected in the present investigation do not permit the energy of either transition to be determined with great precision. The 1115.8 keV transition is a member of a triplet which is deconvoluted differently in each of the five singles measurements which were used for energy determinations. The value, $1115.80 \pm .07$ keV, is the weighted average of the values for the middle member of the triplet for the five angles. There was not sufficient resolution in the polarization experiment for the triplet to be broken up reliably. The 513.7 keV transition feeds a level which is also fed by radioactive decay from ^{82}Y (53-54). In the 602.2 and 1175.6 gates therefore it is not possible to distinguish the annihilation gamma ray of 511. keV and the 513.7 keV gamma ray depopulating the 3^{+} level. The value, 513.68(03), is the weighted average of the third member of a triplet that was deconvoluted from the high energy tail of the 511.0 keV annihilation gamma ray peak.

The 1996.0, 4^+ , level is depopulated by transitions with energies 820.3 and 667.5 keV. According to the results of the angular distribution and polarization measurements, the 820.3 keV gamma ray is a stretched E2 transition to the 1175.8 2^+ level. The 820.3 keV gate shows evidence of the decay of ^{80}Kr which has a 4^+ to 2^+ transition with an energy that has been reported as 819.4 keV (33) and 819.9 keV (55). However the energies of the peak in the singles measurement vary only from 820.20 to 820.28 over five measurements indicating that most of the intensity is due to ^{82}Sr . The 667.5 keV gamma ray decays to the 4^+ level of the ground state band. According to the polarization measurements it is a mixed E2/M1 transition with a mixing ratio of 1.1 (1.3).

Two gamma rays also de-excite the 6^+ level at 2836.3 keV; an 840.2 keV transition to the 4^+ level and a 606.6 keV transition to the 6^+ level in the ground state band. Both of these gamma rays are members of doublets. The angular distribution of the 606.8 keV gamma ray indicates that it has a $\Delta I = 0$. The polarization measurement indicates no change of sign, making it an E2/M1 transition with a mixing ratio of 0.62(51). The angular distribution of the 840.2 keV transition implies a $\Delta I = 0$, probably due to the ambiguous fit to the doublet. However, the addition of the information from the polarization experiment supports the $6^+ \rightarrow 4^+$ assignment.

The 3622.7 keV 8^+ state can decay through three transitions, 380.0 keV, 1393.5 keV and 786.4 keV. The 380.0 keV and 1393.5 keV gamma rays were not strong enough for valid results from the polarization

measurements. That the 786.4 keV gamma ray represents a stretched E2 transition is supported by both the angular distributions and the polarization measurements.

The level at 5427.0 keV is assigned a tentative spin of (12^+) . Because the only observed gamma ray which de-excites this level is a member of a doublet, neither the angular distribution nor the polarization values can be determined accurately. However the measured values do suggest a stretched E2 transition.

A similar problem arises for the (14^+) level at 6543.9 keV. Although the angular distribution measurements support a spin change of 2h, the 1116.9 keV gamma ray cannot be resolved from the 1115.8 keV gamma ray in the polarization measurements. The energy is a simple average of the energies of this transition seen in gates in which the 1115.8 keV transition is not seen.

The 7827.8 keV level is only tentatively proposed; its defining transition at 1283.9 keV is weak, being resolved in the singles spectra only at 0° and 30° . It appears very weakly in the coincidence gates, but when the gates for the members of the positive parity band are compressed, the 1283.9 keV gamma ray appears in each one of them. Summing the uncompressed gates at 0° results in a 1283.9 keV gamma ray with an intensity that is stronger than any other gamma ray in the spectrum except for those already identified as band members. Because this gamma ray was too weak to be seen in the polarization measurements and was resolved at only two angles in the angular distributions, the spin and parity assignment of (16^+) for the 7827.8 keV energy level are based solely on systematics.

Negative Parity Band Levels.

The 3^- state at 2402.2 keV is probably not a member of the negative parity band. The fact that other nuclei in this region have 3^- states at the same energy (55-57) indicates that this state might be interpreted as an octupole ($\lambda=3$) vibrational state. The energy also differs significantly from that predicted by the two quasiparticle-plus-rotor model calculations for the negative parity band (see the following section). Transitions between this level and the 5^- state of the negative parity band are very weak. This level was first observed in (p,t) reactions (17) and assigned an energy of 2405 ± 5 keV. It is verified in the present work by a weak 1828.4 keV peak in the 573.6 keV gate. A gate set on the 1828.4 keV gamma ray shows a 573.6 keV peak as the strongest coincidence. The spin and parity assignments are based on agreement of energy with the (p,t) reaction results (17) and the occurrence of other 3^- states at about the same energy in related nuclei.

The 2817.6 keV, 5^- level is fed by a gamma ray with energy 694.0 keV and deexcited by two gamma rays, 1489.0 and 415.1 keV. Most of the intensity flows through the 694.0 to the 1489.0 keV transitions. The spin and parity of this level are assigned on the basis of the angular distribution and polarization data for the 1489.0 keV transition which indicate an E1 transition. This state was also seen in the (p,t) reaction work (17) and identified there as a 5^- or 4^+ . The intensity of the 415.1 keV gamma ray is primarily due to ^{181}Ta from the target backing.

The decay of the 7^- level at 3511.5 keV proceeds primarily through the 694.0 keV stretched E2 transition to the 2817.6 keV level. There

are also a weak 1281.1 transition to the 6^+ 2229.5 keV level, a 269.0 keV transition to the 8^+ level in the ground-state band, and a 423.5 keV transition to the 6^- level at 3087.0 keV. Both the angular distribution and the polarization measurements verify the E2 nature of the 694.1 keV transition and therefore the 7^- spin and parity assignment.

The 4387.3 keV, 9^- , level decays primarily by a gamma ray with energy 876.0 keV. The exact energy, intensity, angular distribution and polarization of this transition are somewhat tenuous because there is a strong 875.1 keV contaminant due to the reaction products ^{83}Sr and ^{81}Rb . There is a weak 1144.2 transition to the 8^+ 3242.8 keV level. The spin and parity are based on the apparent stretched E2 nature of the transition seen in our data and suggested by the the $^{66}\text{Zn}(^{19}\text{F}, p2n)^{82}\text{Sr}$ reaction studied by Dewald (20). The assignment agrees with the systematics of the $N = 44$ isotones (see Figure 4-17).

The energy of the level at 5392.7 keV is not well determined. The 1005.4 keV transition which de-excites this level is a member of a 1003-1005 keV doublet. As the energies were taken from the angular distribution spectra, the assigned energies depend on how one breaks up the doublet. For four of the angles the energy of the second member varied from 1004.8 to 1005.5. Dewald assigns an energy of 1006.0 keV to this transition (20). The spin and parity assignments are based on the angular distributions and systematics. Within the resolution of the polarization experiment the two members of this doublet could not be differentiated.

The level at 5914.8 keV was assigned a spin of 12 based on the angular distribution which showed it to be de-excited by a highly aligned dipole transition to the (11^-) level. Although the polarization

results are not conclusive, they do indicate that it is more likely that the parity changes in the transition to the 11^- state than that it does not. (The χ^2 calculations for the 522.1 keV transition are shown in Figure 4-3). Therefore the 5914.8 keV state is assigned a spin and parity of (12^-) . The placement of the 522.1 keV transition in this work differs from that suggested by other authors (18-20). This point is discussed in detail in the section on the negative parity band.

Levels in a New Band.

A fourth possible band is presented for the first time in the present work. Although the $I = 7$ level at 3526.3 keV has also been proposed by Dewald (20), the transitions which feed it have not been reported previously. The 3526.3 keV level decays through two gamma rays, 1296.2 and 439.9 keV. Each of these gamma rays has an angular distribution which indicates a spin change of one. The χ^2 analysis of the polarization plus angular distribution data of the 1296.2 keV gamma ray indicates no change of parity although the possibility that the parity changes also cannot be statistically ruled out (See Figure 4-4). Based on systematics, one would expect this level to have a spin and parity of 7^- . Because of the uncertainty in the measured polarization, $.18 \pm .28$, the results of the χ^2 calculations cannot be used as a strong argument for a parity assignment. Therefore the assignment of the parity for this level (and thus, this band) will have to await the results of future experiments.

The gamma rays which decay from the 4367.5 keV level feed three levels assigned a spin of 7. All three of these transitions have angular distributions which are consistent with either $\Delta I = 0$ or

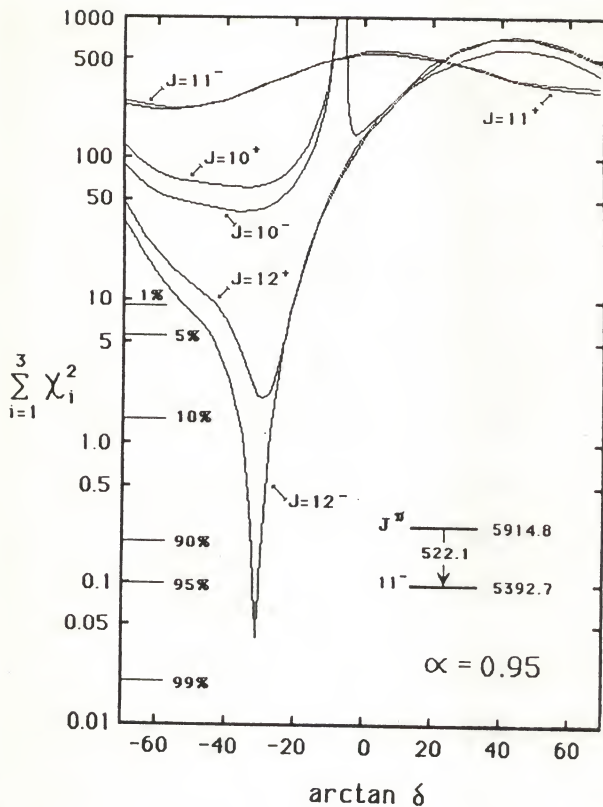


Figure 4-3. χ^2 Calculations for the 522.2 keV transition.

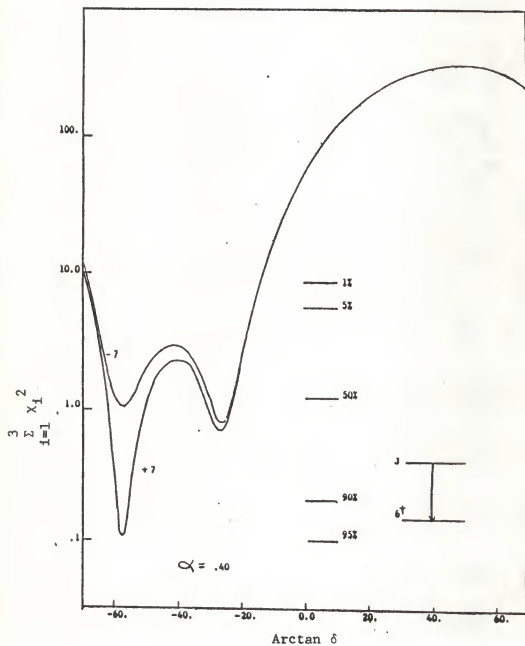


Figure 4-4. χ^2 Calculations for the 1296.2 keV transition.

$\Delta I = 2$. None of the three was resolved in the polarization data because they all lie under a stronger peak at or about the same energy. Therefore the level at 4367.5 keV can only be assigned a spin of 7 or 9 with the parity unknown. Systematics would favor a spin of 9^- however.

The 941.3 keV transition which feeds the 4367.5 keV state has angular distribution coefficients which allow $\Delta I = 0$ or $\Delta I = 2$. The polarization results indicate that $\Delta I = 2$ is the more probable choice and that there is no change of parity. This does not help with the assignment of spin and parity for the 5308.7 keV level because of the uncertainty in the assignments for the 4367.5 keV level. According to systematics, it is probably an 11^- state.

The 5308.7 keV level is fed by the 1056.0 keV gamma ray from a level at 6364.8 keV. Although the statistics for the angular distribution and polarization results do not allow an unambiguous conclusion, they are consistent with a stretched E2 characterization. A 13^- assignment for the level would agree with systematics.

Other levels

There are additional energy levels which are not clearly associated with band structure but which may be the lower spin members of bands whose higher spin members are too weak to be observed in the present reaction.

A level at 2683.7 keV is fed by a 403.9 keV gamma ray from the 6^- state and decays by a 156.9 keV gamma ray to the 5^+ level at 2526.7 keV. This level is assigned a spin of 5 based on the angular distribution.

The 2824.9 keV level is assigned a spin and parity of 4^- based on the angular distribution and polarization of the 1135.5 keV transition which deexcites it. The 261.8 keV gamma ray which feeds it has an angular distribution which is consistent with a stretched E2 transition, but its polarization could not be measured. The spin and parity assignments of this level agree with those of Dewald (20).

At 3087.0 keV is a level which is fed by two gamma rays and which decays by three gamma rays. The assignment of 6^- as its spin and parity agrees with that of Dewald (20). It is based on the $\Delta I = 1$ angular distribution of two transitions from levels with spin 7 and two transitions to levels with spin 5. The polarization of the 423.5 keV transition from the 7^- level indicates no change of parity.

The angular distribution of the 1336.5 keV transition from the 3566.0 keV level to the 2229.5 keV, 6^+ , level in the ground state band indicates a spin change of 1 \hbar . The results of the polarization experiment were inconclusive. The tentative assignment of (7) is based on systematics and the observation that a level is somewhat more likely to decay to another level of lower spin and a gamma ray with the proper energy to decay from this level to a 4^+ level is not seen in the singles spectra. The coincidence spectra only includes gamma rays up to 2000 keV.

The level at 3686.1 keV decays through a 443.3 keV transition to the 8^+ level of the ground state band. There is also a tentative decay through a 598.6 keV transition to the 6^- level at 3087.0 keV. The

angular distribution of the 443.3 keV transition indicates $\Delta I = 0$ or 2. The χ^2 analysis favors the $\Delta I = 0$ assignment, but the uncertainty in the polarization result is too great to use for parity assignment.

The level at 3609.0 keV is a tentative level that helps explain coincidences that are not otherwise readily understood. For example, the 941.3 keV gamma ray and the 522.1 keV gamma ray are in coincidence with each other, but no connecting transition is seen in either gate for the $12^- + 11^-$ transition and the 941.3 keV radiation. In addition, the 522.1 keV gamma ray is in coincidence with one at 602.2 keV and is seen in a 0° gate set on the latter. The 522.1 keV gamma ray is also seen in both the 758.8 keV 90° and 0° gates. The $12^- + 11^-$ transition is seen only in the 90° gates (i.e., 90° with respect to the beam). The spin and parity of the 3609.0 keV level is difficult to assign. The 758.8 keV gamma ray has an angular distribution that is consistent with $\Delta I = 0$ or 2 \hbar . The 522.1 keV gamma ray is an E2/M1 transition with a $\Delta I = 1$. It decays to the 6^- level at 3087.0 keV. If the level at 4367.5 keV is 9^- , then the 3609.0 keV level would have a spin of 7 \hbar .

A tentative level is placed at 4197.1 keV to account for a 511. keV gamma ray which feeds the levels at 3686.1 and 3242.8 keV. Although the 511. keV may be annihilation radiation from the decay of a high spin isomer of ^{82}Y (which has not yet been observed), the fact that this transition is seen more strongly in the 0° gates indicates an anisotropy that would not be characteristic of annihilation radiation. The actual placement of this gamma ray is highly speculative at this point.

Two-Quasiparticle-Plus-Rotor Calculations

In the two-quasiparticle-plus-rotor model the core is assumed to be a deformed rotor whose excited states can be fitted by the variable moment of inertia model. At high enough spin, a particle pair is broken by the Coriolis force and the angular momentum of the pair is partially aligned with the angular momentum of the core. The basis states for the Coriolis mixing calculations are generated with Nilsson wave functions.

The Nilsson wave functions for ^{82}Sr were calculated by Soundranayagam (58) using the program WAVEFN.FOR (59). By choosing the parameters, κ and μ , one can generate the neutron and proton Nilsson levels as a function of the deformation parameter, δ . The values used in the present calculation are given in Table IV-1.

The Nilsson levels generated by the program are shown in Figures 4-5 and 4-6. In these plots the y-axis represents the level energy in MeV. The x-axis is labeled by the deformation, δ . The shell model quantum numbers are given for $\delta = 0$ and the asymptotic quantum numbers are used at $\delta = 0.4$.

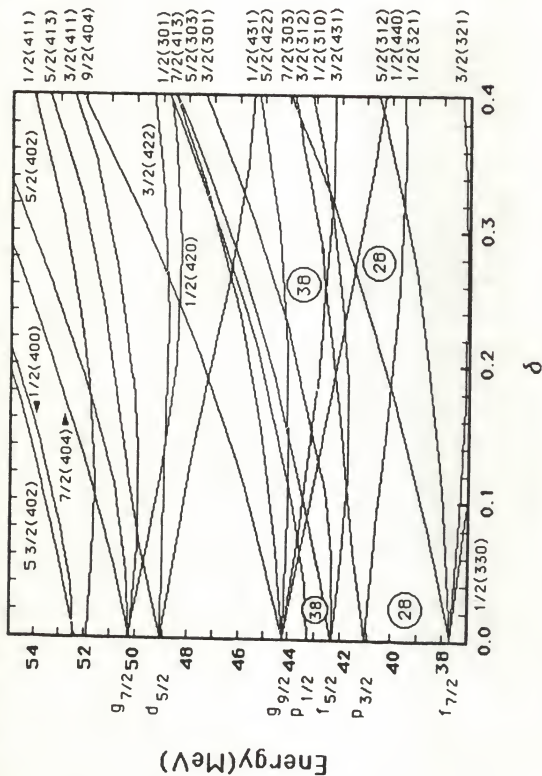
Shell closings are characterized by energy gaps between orbitals. One can see that the shell closings generated by the shell model (represented by $\delta = 0$ here) are not necessarily reproduced for a deformed nucleus. In the proton plot there is a larger (1.6 MeV) gap at $Z=38$ for $\delta = 0.27$ than at $\delta = 0.0$ (0.6 MeV). The orbitals nearest the Fermi level are the $g_{9/2}$, $p_{3/2}$, and $f_{5/2}$ levels. The valence orbitals within two MeV of the Fermi level are the $g_{9/2}$ and $f_{5/2}$ orbitals. Another $f_{5/2}$ orbital is one MeV higher in energy. Thus one would predict that proton quasiparticle excitations would be $(g_{9/2}, g_{9/2})$,

TABLE IV-1
Parameters Used to Calculate Nilsson Levels

	Shell No.	K	μ
Neutron Levels	3	0.04	0.55
	4	0.06	0.50
Proton Levels	3	0.07	0.31
	4	0.07	0.38

TABLE IV-2
Nilsson Configurations Chosen for the Basis States of Negative Parity

Shell	Configurations	Levels
3	$\frac{3}{2}^-$ (312), $\frac{5}{2}^-$ (303)	$f_{5/2}$
	$\frac{1}{2}^-$ (310), $\frac{3}{2}^-$ (301)	$p_{3/2}$
4	$\frac{3}{2}^+$ (431), $\frac{1}{2}^+$ (440),	$g_{9/2}$
	$\frac{5}{2}^+$ (422)	

Figure 4-5. Nilsson levels for protons in ^{82}Sr .

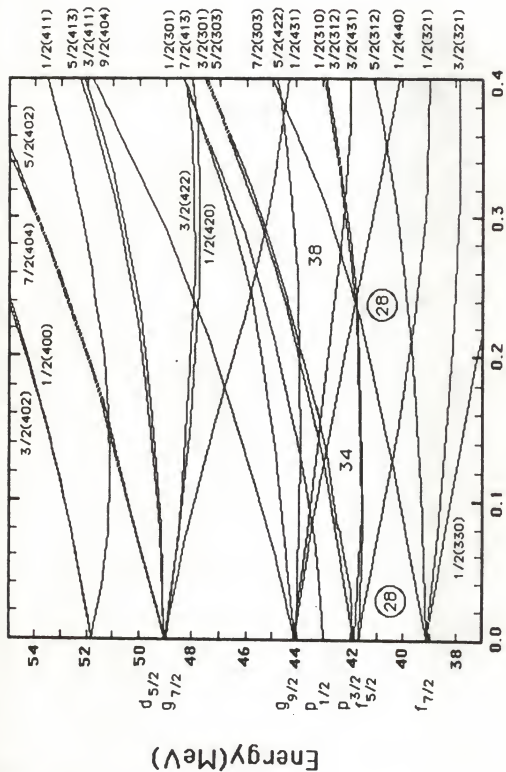


Figure 4-6. Nilsson levels for neutrons in ^{82}Sr .

$(g_{9/2}, f_{5/2})$, $(p_{3/2}, g_{9/2})$, or $(p_{3/2}, f_{5/2})$ configurations. Only the first and last of these combinations would yield positive parity states.

The neutron levels have no energy gap at $\delta = .27$ for $N = 44$. The levels just below the Fermi surface ($\lambda = 44.8$ MeV) are the $f_{5/2}$ and $p_{3/2}$ orbitals. The closest valence levels, with a gap of approximately 0.8 MeV, are the $p_{1/2}$ level and $g_{9/2}$ levels which are almost degenerate. Another 0.5 MeV above those two orbitals is another $g_{9/2}$ orbital. Thus the predicted neutron quasiparticle excitations would arise from $(p_{3/2}, p_{1/2})$, $(f_{5/2}, p_{1/2})$, $(p_{3/2}, d_{5/2})$, or $(f_{5/2}, d_{5/2})$ configurations. The first two would yield positive parity states and the last two negative parity states.

In an attempt to understand the negative parity band, the experimental levels were fitted using the Coriolis mixing program, COREMX.FOR (60). The input parameters were varied until a good fit to the level energies was obtained. The parameters and the values used for the fit were:

1. The Fermi level, obtained from the Nilsson plots ($\lambda = 42.78$),
2. The energy gap (less than $12/A^{1/2}$) ($2\Delta = 0.46$ MeV),
3. \mathcal{J}_0 and C from the VMI fit of the ground state band ($\mathcal{J}_0 = 0.8 \times 10^{-3} \text{ keV}^{-1}$ and $C = 0.14 \times 10^8 \text{ keV}^3$),
4. Wavefunctions calculated from WAVEFN.FOR for a given δ ($\delta = 0.27$),
5. Oscillator shell numbers and configurations for construction of the basis states (Table IV-2).

The basis states are chosen from those close to the Fermi level because they are expected to have a larger contribution to the quasiparticle excitations than those farther away.

The selection of Nilsson orbitals used in the construction of the basis states of the wave functions is somewhat dependent on the choice of δ . A first-pass value for δ is 95% of the value of β obtained from the $B(E2, 2^+ \rightarrow 0^+)$ using Bohr and Mottelson's rigid rotor relationships, which for ^{82}Sr is .287 (see Chapter 3). As ^{82}Sr does not exhibit the ground state band energy spacings of a rigid rotor (see Figure 3-7), this value of β may not be an accurate representation of the deformation of this nucleus. Even if it does describe the deformation of the 2^+ state, the deformation of higher spin levels may be affected by the quasiparticle excitations. Therefore, the value of δ used in these calculations should be considered only as an average value, the one that gives the best fit.

The change in internal structure with spin is taken into account in another way in these calculations. The values of β_0 and C from the VMI fit to the ground state band are allowed to vary from their original values in the calculation of the rotational Hamiltonian. In this way the possible changes in both deformation and softness are taken into account. The final values differ by 42% from the VMI parameters input to the calculation. This indicates that the structure of the nucleus in this band differs from that of the ground-state band.

The best fit to the experimental levels was obtained with two-proton-quasiparticle states. The levels obtained with this calculation are shown in Figure 4-7. The 5^- state is produced primarily by a $(f_{5/2}, g_{9/2})$ configuration (97%) with a small mixture of a $(p_{3/2}, g_{9/2})$ configuration (3%). The percentage of the $(f_{5/2}, g_{9/2})$ configuration decreases as the spin increases so that at $J=11^-$ there is only 88% $(f_{5/2}, g_{9/2})$ and 12% $(p_{3/2}, g_{9/2})$.

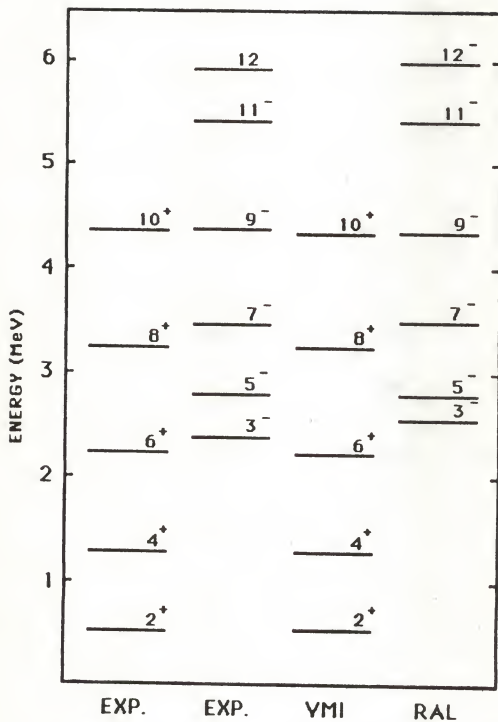


Figure 4-7. Two-quasiparticle-plus-rotor calculation results for ^{82}Sr .

In Figure 4-7 it can be seen that the 3^- experimental level does not correspond to the level predicted by the model, indicating it probably is not part of this band. The levels at 5^- , 9^- and 11^- are fitted to within 19 keV of the experimental level. The 7^- level varies 74 keV from the experimental level. The $I=12$ state was not used in the fit as its parity was not known at the time the fit was done. However the model predicts a 12^- state at 5985 keV which might be identified with the experimental level at 5915 keV.

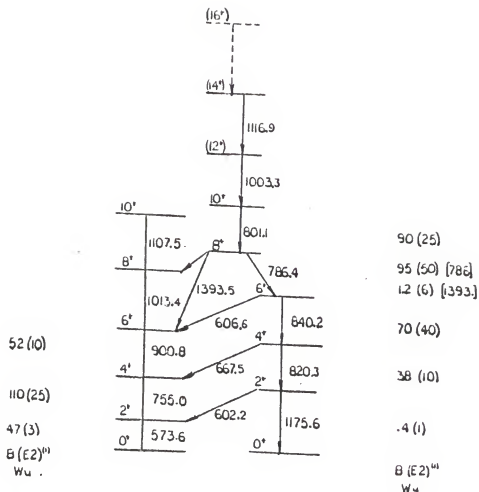
Positive Parity Band

The first excited positive parity bands in the even-even transitional nuclei in this mass region ($N \sim Z \sim 40$) are often interpreted as quasi-gamma bands. These bands have the following properties which are characteristic of the gamma-vibrational bands in well-deformed nuclei: (1) the band head is a 2^+ state; (2) it is a $\Delta I = 1$ band; (3) the states decay primarily by skipped stretched E2 transitions; (4) the energy spacings for the even-integer spins and the odd-integer spins are approximately rotational in character for the higher spin states; (5) the transitions between this band and the ground state band are much weaker than the transitions within the band. These bands are usually seen only up to spins $7^+ - 9^+$. They are presumed to arise from a two-phonon vibrational excitation of the ground state configuration. The projection of the angular momentum on the symmetry axis is $K = 2^+$.

In ^{82}Sr , the first excited positive parity band has characteristics (1), (2), (3), and (5). As for (4), the higher spin states do have approximately rotational energy spacings, but the rotational spacing .

doesn't occur until spin $I > 8^+$ which is where most quasi-gamma bands die out (see Figure 4-8). Up to that spin, the level spacings for the even-integer spins appear vibrational in character. The levels with odd-integer spins do have spacings which are characteristic of rotational bands. The unusual feature of this particular band is its high degree of collectivity to spin 12^+ .

The graph of the moment of inertia with respect to the angular frequency based on the rotational model indicates a change from vibrational characteristics to rotational characteristics at $I = 10^+$ (See Figure 3-9). Either this band is a single band which makes an abrupt phase transition at $I = 10^+$ or there are two bands which cross at $I = 6^+$ with an unusually strong interaction. The first possibility is supported by the strong transition probabilities between the band members. In this case the nucleus exhibits behavior that would indicate it has become a rigid rotor. Although this possibility is highly unusual for this region of the nuclear chart, similar behavior has been reported for ^{84}Zr (6) and the behavior of the two isotones will be compared below. The second possibility has been discussed by Funke et al. in reference 5 and their findings will be reported also. Although both approaches assume the breaking of a proton pair and the alignment of the quasiparticle angular momenta with the rotation of the core, the difference is in the way that the alignment is taken into account. In the first case it is simply added to the angular momentum of the core and the total is used to calculate the moment of inertia. In the second case, the moment of inertia is calculated as a function of the angular momentum of the core alone without considering the aligned momenta of the quasiparticles.



$^{11}B(E2)^{Wu}$ FROM DEWALD (20)

Figure 4-8. Positive parity band in ^{82}Sr .

The assumption that all the angular momenta contribute to the moment of inertia leads to an interpretation of rigid rotor behavior at $I > 10^+$ based on the moment of inertia plot of Figure 3-9. The average moment of inertia above 10^+ is 47.5 MeV^{-1} . The rigid body moment of inertia, \mathcal{J}_{rig} , can be calculated with the equation (26)

$$\frac{2\mathcal{J}_{\text{rig}}}{\hbar^2} = \frac{2}{5} \text{MAR}_0^2 \left[1 - \left(\frac{5}{4\pi} \right)^{1/2} \beta \cos(120 + \gamma) \right].$$

If $\beta = .287$ (from the $B(E2, 2^+ \rightarrow 0^+)$) and $\gamma = 22.5^\circ$ (from the relationship of the 2^+ to the 2^{+1} states), then $\mathcal{J}_{\text{rig}} = 48.7 \text{ MeV}^{-1}$. Assumption of axial symmetry ($\gamma = 0$) and $\beta = .287$ results in $\mathcal{J}_{\text{rig}} = 46.5 \text{ MeV}^{-1}$. Both the values of γ and β are taken from model-dependent calculations for low-spin states. Although there is no reason for one to believe the nucleus maintains its ground state shape to spins 14^+ to 16^+ , the range of possible values for β and γ all lead to an \mathcal{J}_{rig} which is close to the value taken from the graph.

The interpretation of the behavior of the nucleus as a rigid rotor above spin $I = 10^+$ suggests that there has been a breakdown of the pairing force which usually keeps the moment of inertia at about one-half the rigid body value. This would be a classic example of Mottelson-Valatin Coriolis antipairing (51). A similar interpretation of the moment of inertia plot has been made by Price et al. (6) for the ground-state band in ^{84}Zr . The two nuclei are isotones and their level schemes are very similar (see the section on Systematics).

In their paper, Price et al. (6) treat the ^{84}Zr data with the formalism of the cranked shell model. The rotational frequency is defined by equation 3.49 and the alignment of the angular momentum along

the rotation axis by equation 3.50 of the present work. The kinematic moment of inertia is $\mathcal{J}_{(1)} = I_x/\omega$. Comparison of their plots of I_x vs. $\hbar\omega$ and $\mathcal{J}_{(1)}$ vs. $\hbar\omega$ for the ground state band of ^{84}Zr to the same plots for the positive parity band of ^{82}Sr shows similar behavior. In both moment of inertia plots, [Figures 4-9 (a) and (b)] the moment of inertia exhibits large changes with small changes in rotational frequency up to a given frequency after which there is very little change. In contrast, the moment of inertia of the ground state band of ^{82}Sr changes gradually with rotational frequency.

The plots of aligned angular momentum vs. rotational frequency (Figure 4-10) both show sharp gains in alignment: ^{82}Sr at $\hbar\omega \approx 0.400$ MeV and ^{84}Zr at $\hbar\omega \approx 0.500$ MeV and $\hbar\omega \approx 0.600$ MeV. These gains in alignment are attributed to the breaking of a quasiparticle pair. In the case of ^{84}Zr the calculations suggest that the alignments are due first to two $g_{9/2}$ quasiprotons and then to two $g_{9/2}$ quasineutrons (6). The alignment in ^{82}Sr is attributed to two $g_{9/2}$ quasiprotons (5). A second alignment of quasiparticles is not seen.

Although the plots of I_x and $\mathcal{J}_{(1)}$ are very similar for the two nuclei, indicating similar structural behavior, Price et al. (6) base their claim of rigid rotation on some facts which do not apply to ^{82}Sr . In ^{84}Zr the transition to rigid rotor behavior occurs at $\hbar\omega = .9$ MeV, more than twice the frequency of the apparent ^{82}Sr transition at $\hbar\omega = .4$ MeV. In ^{84}Zr both protons and neutrons have undergone a bandcrossing. Only the protons have undergone a bandcrossing in ^{82}Sr . The nuclear configurations of both nuclei are influenced by the $N = Z = 38$ deformed shell gap however. Price et al. (6) compare the possible β and γ values for the experimentally

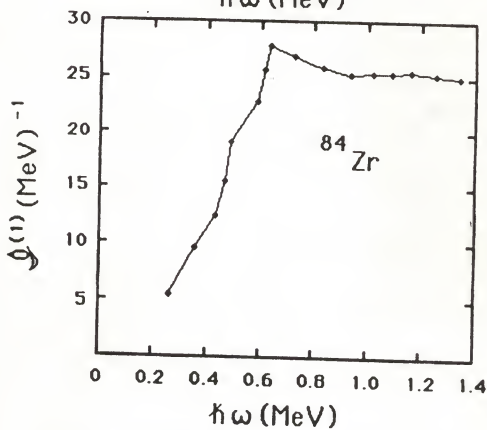
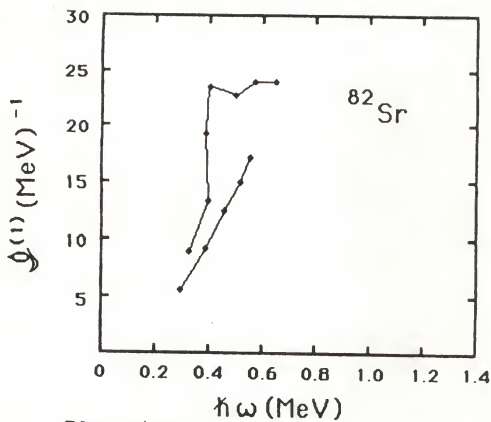


Figure 4-9. Kinematic moment of inertia for (a) ^{82}Sr and (b) ^{84}Zr .

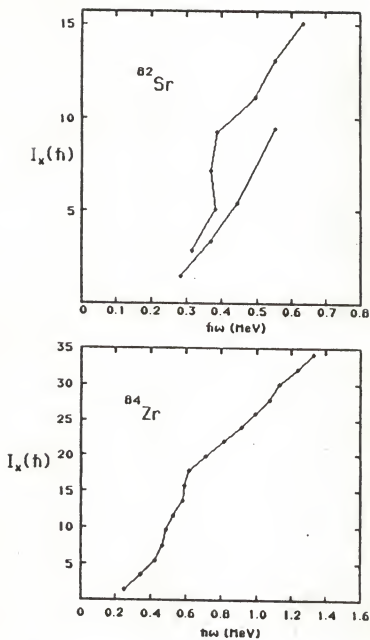


Figure 4-10. Aligned angular momentum for (a) ^{82}Sr and (b) ^{84}Zr .

obtained transition quadrupole moment of ^{84}Zr moment of inertia and find a consistent set of shape parameters of $\beta = .43 \pm 0.3 \text{ MeV}^{-1}$ and $\gamma = 3^\circ \pm 6^\circ$. They find that these results are consistent with the rotation of an axially symmetric nucleus with no pairing. It would be interesting to measure the quadrupole moment of ^{82}Sr to see if similar results would be obtained.

Funke et al. (5) also use the cranked shell model (CSM) to describe the positive parity band. However, they compare $I_x(\omega)$ and $E'(\omega)$, the energy in the rotating system, with the values of a reference configuration (the $K = 1/2$ band of ^{81}Rb) which has almost all collective rotation in order to extract the aligned angular momentum of the quasiparticle excitations, $i(\omega)$, and the quasiparticle energies, $e'(\omega)$. According to their results, the S-band, which is the lowest quasiparticle band, originates from two $g_{9/2}$ protons. They derive a value of $i = 4.2 \text{ h}$ for ^{82}Sr . In addition they use a two-band mixing calculation to determine the interaction strength between the two bands. They found that $V_{g-s} < 35 \text{ keV}$ and $V_{\gamma-s} = 120 \text{ keV}$ for ^{82}Sr . Comparison to ^{80}Kr and other Kr nuclei indicate a correlation of V_{g-s} and an anticorrelation of $V_{\gamma-s}$ with proton number. The solid line in Figure 4-11 represents the calculated value of the absolute value of the interaction matrix element V_{g-s} as a function of the position of the Fermi surface and proton number for two $g_{9/2}$ protons. The two data points are for ^{80}Kr and ^{82}Sr . Preliminary results indicate that ^{78}Se has a large g-s interaction as predicted (5). The previous material on ^{84}Zr (6) would also indicate that it has a larger V_{g-s} interaction than ^{82}Sr . The strong interaction between the γ -band and the S-band would also help explain the strong transition probabilities of this band.

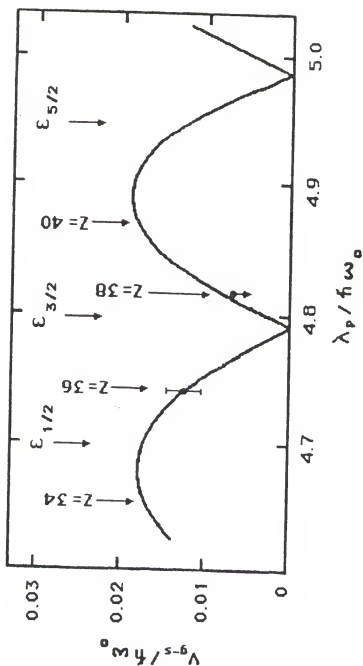


Figure 4-11. Absolute value of the interaction matrix element $V_{g-s}(5)$.

According to Funke et al. (5), the $B(E2)$'s in the crossing region should be about 75% those of a pure collective transition. The uncertainties in the measured $B(E2)$'s up to 8^+ are too great to determine if there is actually a slight decrease (see Figure 4-8), but such a possibility cannot be ruled out.

If one subtracts the aligned angular momentum from the total angular momentum, there is left the collective angular momentum. Because the moment of inertia is a collective property, it is this value that should be used to determine the moment of inertia and rotational frequencies. The result is a very different moment of inertia plot for the S-band (Figure 4-12). Although the collective degree of freedom is still rotational, looking very much like the rotational behavior of the ground state band, it no longer looks like a rigid rotor. The moment of inertia is about 70% that of a rigid rotor at the highest spin. The excitation of aligned quasiparticles in soft nuclei may stabilize the deformation and decrease the pairing correlations (33), but any evidence of rigid rotor behavior would have to come at higher spins and higher rotational frequencies than those seen in the present experiment.

It can be assumed that the positive parity band in ^{82}Sr is made up of two different bands which cross at about $J = 6^+$. The lower energy band is a $K = 2^+$ quasi-gamma band based on the ground-state configuration, and the higher energy band is most likely a two-quasiproton configuration. The apparent collective strength of the transitions comes from the feeding of the two bands from the continuum. Evidently, above the crossing the quasiparticle band is fed rather than the quasi-gamma band and below the crossing the quasi-gamma

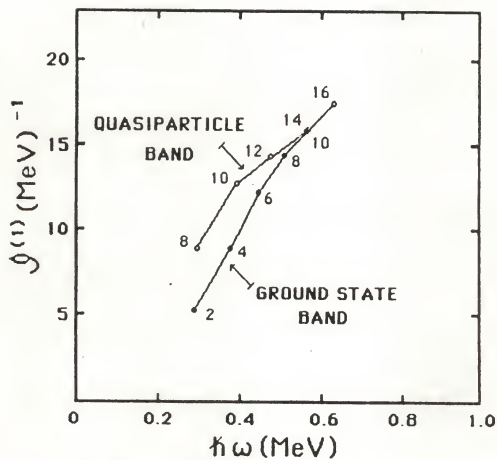


Figure 4-12. Moment of inertia for the positive parity quasiparticle band in ^{82}Sr .

band is preferentially fed so that the strength of the transitions flows down the quasiparticle band to the quasi-gamma band.

Negative Parity Band

The negative parity band is based on the 5^- state at 2817.7 keV. The 3^- state at 2402.5 keV is associated with an octupole vibration (as discussed in the section on the Level Scheme). The 415.1 keV transition between the 5^- and 3^- levels does not have the collective strength one would expect if the 3^- state were the band head of a collective band.

The ordering of the transitions above the 3511.7 keV level in the negative parity band has caused some difficulty. The problems have been

1. The 876.2 keV transition is part of an 875 - 876 keV doublet in which the 875 keV gamma ray is the stronger of the two and belongs to two contaminants (in our reaction the contaminants are ^{83}Sr and ^{81}Rb).
2. The 1005.3 keV transition is part of a 1003 - 1005 doublet in which both gamma rays belong to ^{82}Sr .
3. The 522.1 keV transition is a highly aligned dipole transition and is therefore very anisotropic.

Problems 1) - 3) have made the intensity determinations difficult. A weighted average of the intensities at each of the five angles of the angular distribution measurement yields intensities which do not contradict the ordering suggested in the present work, however the 876.0 and 1005.4 transitions could be reversed in order. The transitions, assigned spins, and averaged intensities relative to the 573.6 keV transition are given in Table IV-3.

TABLE IV-3
Energies and Intensities of Transitions in the Negative Parity Band

E_{γ} (keV)	$J_i \rightarrow J_f$	I_{γ}	$I_{\gamma}^{(a)}$
694.0	$7^- \rightarrow 5^-$	17.2(7)	11.6(4)
876.0	$(9^-) \rightarrow 7^-$	7.5(7)	-
1005.4	$(11^-) \rightarrow (9^-)$	8.1(5)	5.9(4)
522.1	$(12^-) \rightarrow (11^-)$	3.8(3)	8.6(3)

(a) from Dewald (20), $^{66}\text{Zn} (^{19}\text{F}, p2n)^{82}\text{Sr}$

The schemes suggested by other authors are presented in Figure 4-13. Although the relative ordering of the 876, 1005, and 694 keV transitions is suggested by both our data and that of Dewald (23), the placement of the 522.1 keV transition is a point of difference. This gamma ray has a very large relative intensity at 90° and almost no intensity at all at 0° . If one is viewing the reaction at $\pm 90^\circ$ as Higo et al. (19) and Fields et al. (18), did in their coincidence measurements, the 522.1 keV gamma ray appears much stronger than its integrated intensity indicates. Figures 4-14 and 4-15 illustrate the degree of anisotropy of the 522.1 keV transition. Figure 4-14 shows the summed ground-state band gates (573-755-901-1013-1107) set on the 0° detector and on the 90° detector. Although there is no evidence of a 522.1 keV gamma ray at 0° , there is a strong peak at that energy in the 90° gate. The ratio of the intensities of the gamma rays at 0° to 90° taken from the angular distribution measurements is plotted in Figure 4-15 for several transitions in ^{82}Sr . The stretched E2 transitions of the ground-state band have ratios greater than one as expected. The E1 transition from 5^- to 4^+ has a ratio slightly less than one. The 522.1 keV transition has a ratio of one-tenth. No other gamma ray in this study exhibits such a strong anisotropy.

It was suspected that the 522 keV transition fed the 11^- state when the relationships of the TAC spectra for the negative parity band transitions were studied. Gating on pairs of transitions and looking at the time relationship between them indicated that the level at 5392.7 keV might have a longer lifetime than the levels below it. The TAC

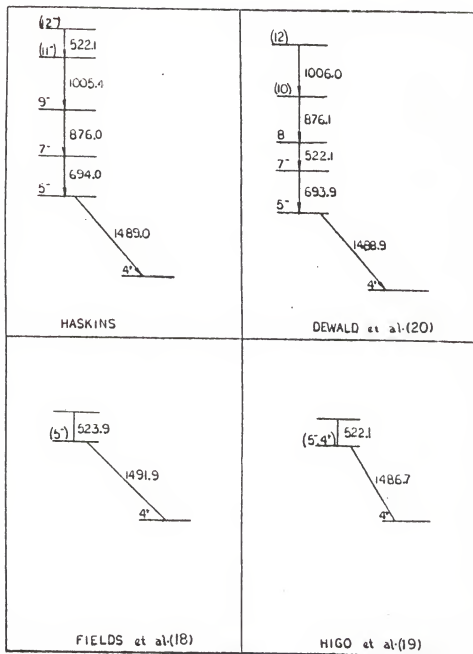


Figure 4-13. Alternative placements of the 522 keV transition.

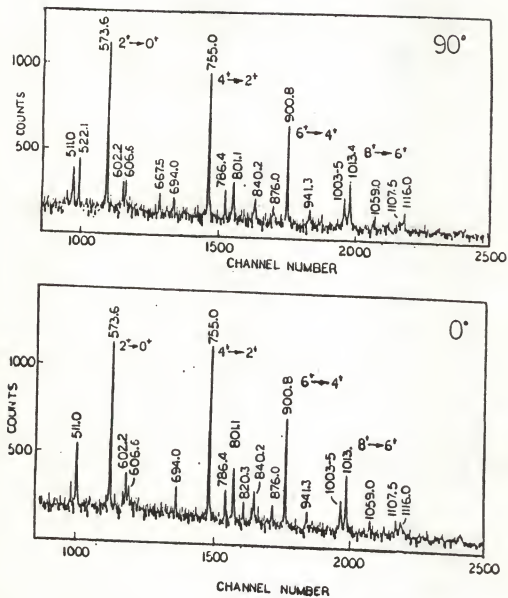


Figure 4-14. Summed ground-state band gates at 0° and 90°.

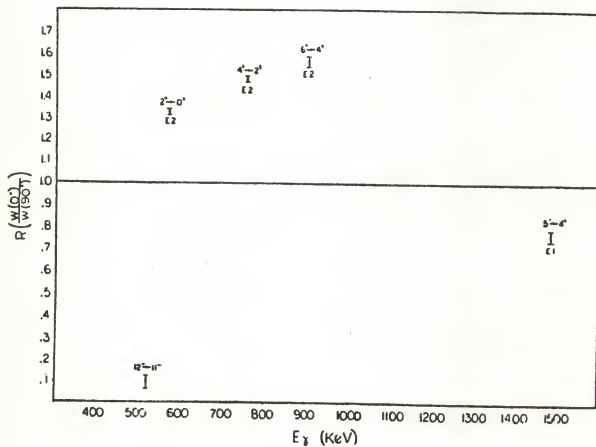


Figure 4-15. Ratio of the intensities of the gamma rays at 0° to 90° .

spectra with the 522.1 keV gamma ray as one of the gating transitions had a FWHM that was slightly broader than the TAC spectra gated on any other combination of gating transitions.

The second indication that the 522.1 keV transition is higher in the level scheme is the high degree of alignment seen in the angular distribution data. As seen in Figure 4-16, the $A_2 - A_4$ plane, the A_2 and A_4 of the 522.1 keV transition fall very close to the A^{max} lines for both $12 \rightarrow 11$ and $10 \rightarrow 11$. This indicates an α_2 of almost one. The results of the angular distribution and polarization experiments indicate a mixing ratio of $-.53$ (37) (see Chapter II). Use of this value in equation 2.12 results in an A^{max} of -1.07 and a calculated α_2 of $.97$ (07). The χ^2 calculations imply an α_2 of $.99$ (05). Based on the statistical model, such a high degree of alignment suggests a level which is at or very near an entry level state, i.e. one that is fed directly from the continuum. A level that is fed through a cascade of yrast-like gamma rays becomes less aligned (see the discussion of the statistical model in Chapter II). A plot of the experimental α_2 vs. I [Figure 4-17 (a)] shows the expected behavior of high alignment at the entry levels decreasing to smaller alignments for the lower spin states. The Dewald (20) placement, on the other hand [Figure 4-17 (b)], indicates a gain of alignment as the spin falls.

Additional support for our ordering of the negative parity band comes from the systematics of the $N = 44$ isotones (Refs. 6, 33, 55, and 57). The negative parity bands of ^{78}Se and ^{80}Kr follow the same spacing as we suggest in ^{82}Sr up to 9^- . In ^{84}Zr the states match up to 11^- (Figure 4-18).

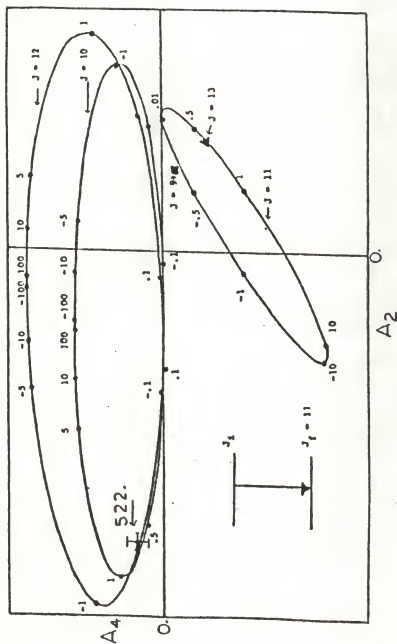


Figure 4-16. A_2 - A_4 plane for transitions feeding a state with spin $I = 11$.

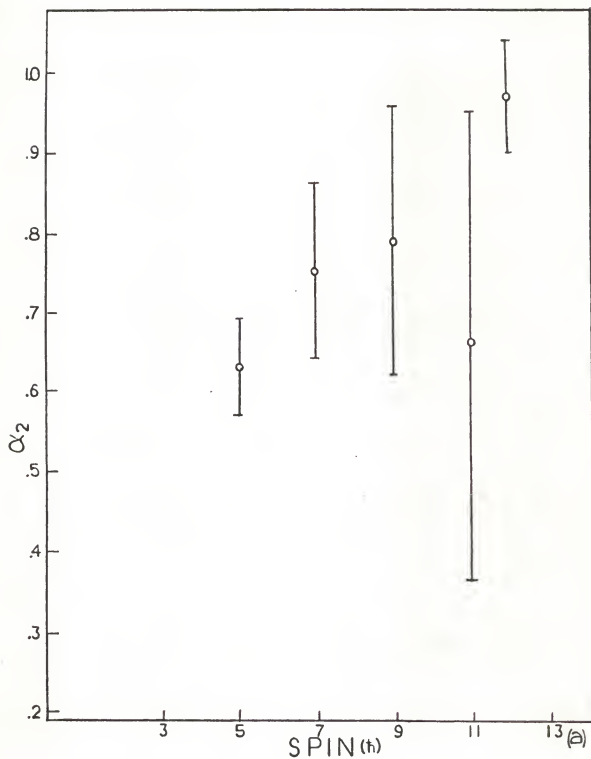
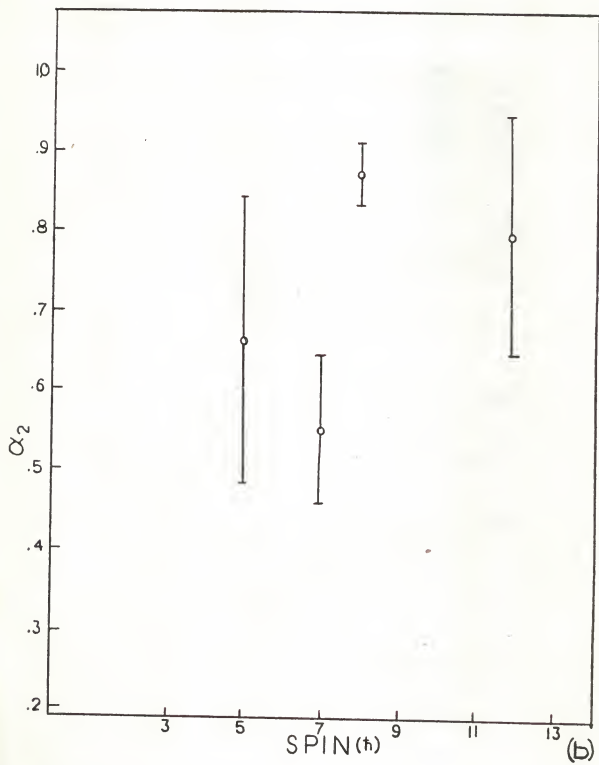
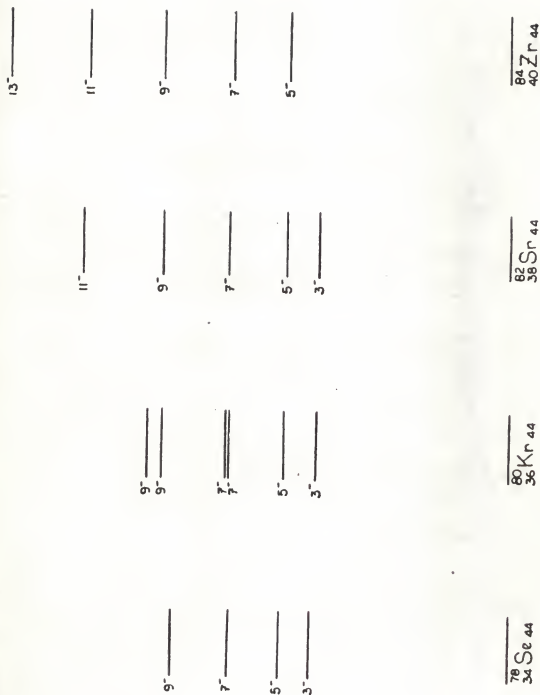


Figure 4-17. Attenuation coefficient vs. spin for the negative parity band from (a) Haskins and (b) Dewald (23).



Figure 4-18. Negative parity bands of the $N = 44$ isotones.

Systematics

In the section of the present work on the Level Scheme frequent reference was made to 'systematics' as an argument for spin and parity assignments. This argument refers to the fact that nuclei with the same number of protons or neutrons frequently exhibit evidence of similar structures. This is particularly true for the $N = 44$ isotones; ^{76}Ge , ^{78}Se , ^{80}Kr , ^{82}Sr , and ^{84}Zr . The similarity of their negative parity bands as shown in Figure 4-18 has been used as an argument for the placement of the 522.1 keV transition.

The ground state bands of these nuclei are given in Figure 4-19 (6, 33, 55, 57, 61). Again there is great similarity of level spacing. Another way of looking at this similarity is to graph the ratios, $R_I = E_1/E_2$ as seen in Figure 4-20. The closest agreement at low spin is between the nuclei with $Z = 38 \pm 2$. This agreement is probably due to the influence of the deformed shell gap at $Z = 38$ (62). At higher spins ($I > 8$) the differences arise from the effect of the quasiparticle excitations on the level spacings.

The positive parity bands exhibit the sharpest difference in structure (Figure 4-21 (6,33,55,57,61)). This may be due to the anticorrelation of $V_{\gamma-s}$ with proton number suggested by Funke et al. (5). The positive parity quasiparticle band seems to interact most strongly with the quasigamma band at $Z = 38$ (^{82}Sr) and with the ground state band at $Z = 36$ or 42 (^{80}Kr , ^{84}Zr) (see Figure 4-11). Why this occurs and whether it is a more general phenomenon is a topic for further study. The effect is illustrated in Figure 4-22 in which the moment of inertia is plotted with respect to the rotational frequency (based on the rotational model). In the left-hand graph the ground-state bands for the $N = 44$ isotones are compared.

$14^+ \text{---} 6300.3$
 $12^+ \text{---} 5439.8$
 $12^+ \text{---} 5134.5$
 $10^+ \text{---} 4622.2 \text{---} 10^+ \text{---} 4379.5 \text{---} 10^+ \text{---} 4350.0 \text{---} 10^+ \text{---} 4067.4$
 $8^+ \text{---} 3583.8 \text{---} 8^+ \text{---} 3411.5 \text{---} 8^+ \text{---} 3242.0 \text{---} 8^+ \text{---} 3068.2$
 $6^+ \text{---} 2545.4 \text{---} 6^+ \text{---} 2393.2 \text{---} 6^+ \text{---} 2229.0 \text{---} 6^+ \text{---} 2136.2$
 $4^+ \text{---} 1410.1 \text{---} 4^+ \text{---} 1501.8 \text{---} 4^+ \text{---} 1436.8 \text{---} 4^+ \text{---} 1328.0 \text{---} 4^+ \text{---} 1263.0$
 $2^+ \text{---} 562.9 \text{---} 2^+ \text{---} 613.4 \text{---} 2^+ \text{---} 617.0 \text{---} 2^+ \text{---} 573.6 \text{---} 2^+ \text{---} 540.0$
 $^{76}_{32}\text{Ge}_{44}$
 $^{78}_{34}\text{Se}_{44}$
 $^{80}_{36}\text{Kr}_{44}$
 $^{82}_{38}\text{Sr}_{44}$
 $^{84}_{40}\text{Zr}_{44}$

Figure 4-19. Ground-state bands of the $N = 44$ isotones.

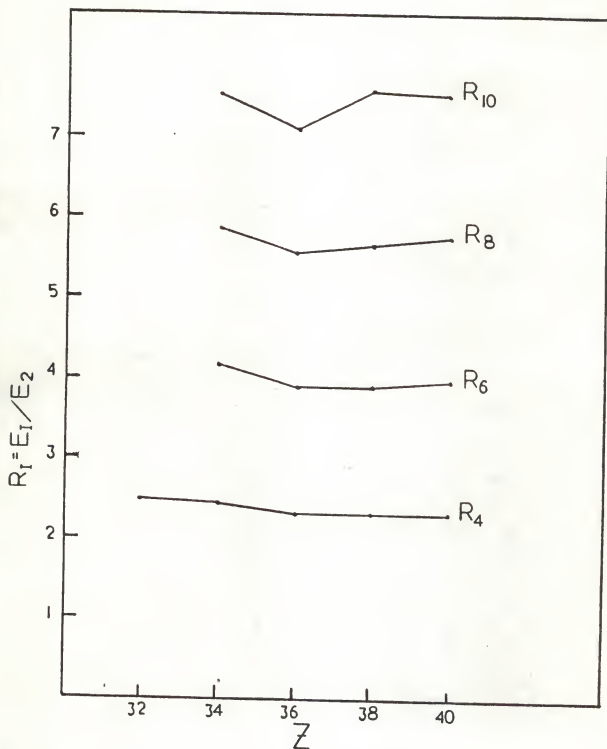


Figure 4-20. $R_I = E_I / E_2$ for $I = 4, 6, 8, 10$ in the $N = 44$ isotones.

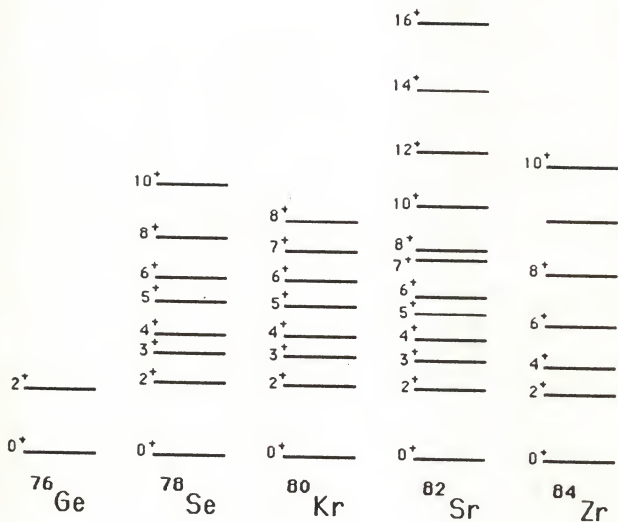


Figure 4-21. Positive parity bands of the N = 44 isotones.

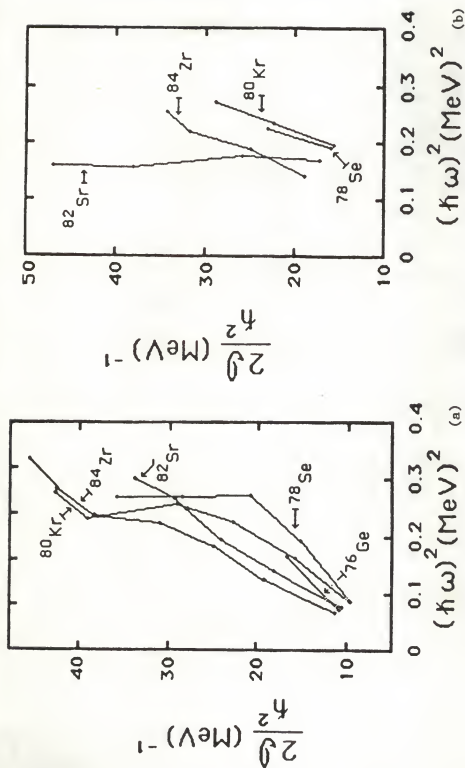


Figure 4-22. Moment of inertia plots for (a) ground-state bands and (b) positive parity bands in the $N = 44$ isotones.

It can be seen that all of these nuclei except ^{82}Sr and ^{76}Ge (for which data are lacking) exhibit the type of backbending which is expected from the crossing of a quasiparticle band. The right-hand graph compares the positive parity bands for these nuclei. Here only ^{82}Sr exhibits the backbending (although sufficient data are not available for one to say anything conclusive about ^{76}Ge or ^{78}Se).

The collective behavior of the $N = 44$ isotones seems to be very similar. The differences in energy levels in these nuclei seem to be caused by differences in the quasiparticle excitations; in particular, in the crossing of the positive parity quasiparticle band with the collective ground state and/or quasigamma bands.

The $Z=38$ isotopes, on the other hand, show a systematic compression of the ground state band energies as successive pairs of neutrons are removed in going from $N=50$ to $N=40$ (Figure 4-23) (4,63,64). This would indicate that the difference in structure of these medium mass nuclei at the spins studied so far ($I \leq 16$) seem to be related to the neutron shell structure. In particular the behavior changes seem related to the filling of the $g_{9/2}$ neutron shell. As the shell is closed, the behavior of the ground-state band becomes less collective.

The ground-state bands of the neutron deficient strontium nuclei can be described by the VMI model. The fits are seen in Figure 4-24. The values used to fit each nucleus are listed in Table IV-4. Although the fits for the other strontium nuclei are not so good as that for ^{82}Sr , the trend in the fitting parameters can indicate structural differences among the isotopes.

As neutrons are removed and the nucleus becomes more deformed, the moment of inertia becomes larger and σ becomes smaller, indicating that the nucleus is becoming more rigid. The change of sign of β between

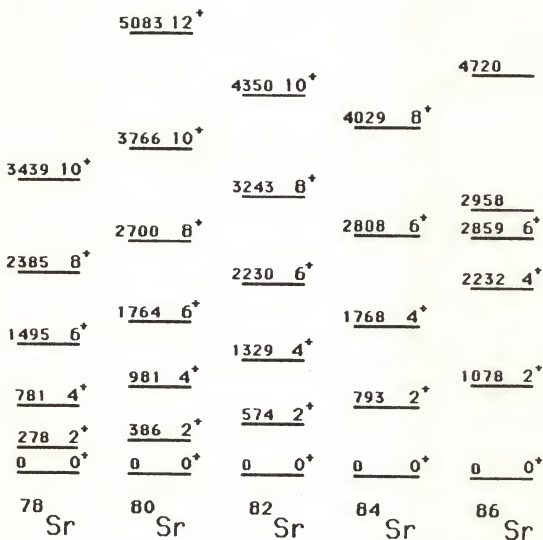


Figure 4-23. Ground-state bands of the strontium isotopes.

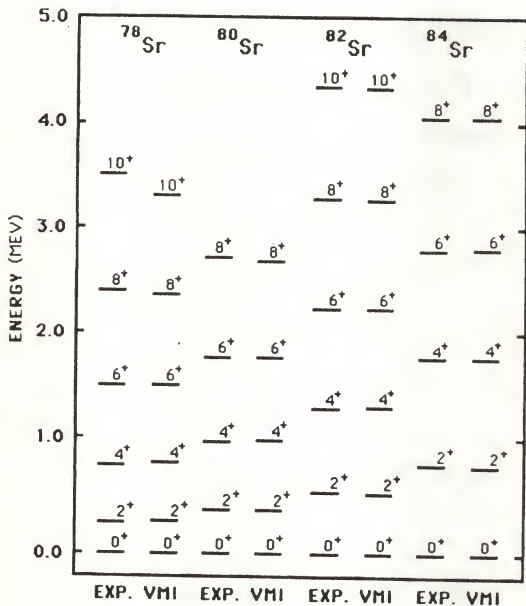


Figure 4-24. VMI fits to the ground-state band levels in the neutron deficient strontium isotopes.

TABLE IV-4
Parameters from VMI Fit to Sr Nuclei[†]

Nucleus	C	β_0	σ
^{84}Sr	1.48×10^7	$-.02 \times 10^{-2}$	2614.0
^{82}Sr	$.92 \times 10^7$	$.14 \times 10^{-2}$	19.39
^{80}Sr	$.84 \times 10^7$	$.56 \times 10^{-2}$.36
^{78}Sr	1.07×10^7	$.99 \times 10^{-2}$.05

[†]Parameters are defined in equations 3.6 and 3.7

^{84}Sr and ^{82}Sr indicates a discontinuity in $\partial \mathcal{J}_{I=0} / \partial \mathcal{J}_0$ that might suggest a second order phase transition (65). The negative value of \mathcal{J}_0 can be associated with an "increased resistance to departure from spherical symmetry" (65).

There seems to be a fundamental change in structure between ^{84}Sr and ^{82}Sr , both lying in the middle of the $g_{9/2}$ neutron shell. The ^{84}Sr nucleus appears rather soft with a nearly spherical ground state (27), whereas the level energies and transition strengths in ^{82}Sr would seem to indicate a more deformed ground state.

A calculation of potential energy surfaces (PES) was made by Bucurescu et al. (27). They used an intrinsic state formalism (66) which enables one to use an IBM Hamiltonian to generate the potential energy surface in the deformation variables, β and γ . The PES gives the equilibrium shape of the ground state of the nucleus. The results are shown in Figure 4-25. The top row is the result of calculations based on the IBM-II Hamiltonian, the bottom row is based on the IBM-I Hamiltonian. The calculations reproduce both the sign of the deformation and the trend of increased deformation with decreased N . Here again is an indication of a nearly spherical ground state for ^{84}Sr and a deformed ground state for ^{82}Sr .

In (p,t) reactions, strong transitions are taken to indicate that both initial and final states have very similar structures. This would imply that the 0^+ state in ^{82}Sr is "spherical" since the $^{84}\text{Sr}(p,t)^{82}\text{Sr}$ $0^+ \rightarrow 0^+$ transition is rather strong. If this is so, then there may be a shape coexistence in ^{82}Sr (27).

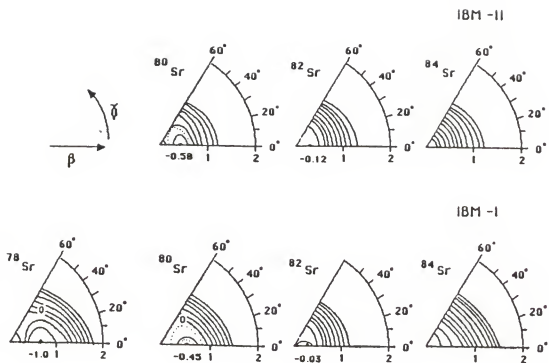


Figure 4-25. Potential energy surfaces for the strontium isotopes calculated with (a) IBM-II and (b) IBM-I. (27).

Unidentified Nucleus

There is evidence in the present study of a reaction product which cannot be identified at this time. In the coincidence gates there are suggestions of band structure that are characteristic of that seen in odd-odd nuclei. The bands are rotational, but there are some low-energy, high-intensity transitions which appear to be low-spin members of these bands. The cross section for production of this nucleus suggests that it is probably produced in a three-particle or four-particle channel. Most of the nuclei produced in those channels can be identified and therefore eliminated as candidates. The most likely candidates for this nucleus is ^{82}Y , produced by $^{70}\text{Ge} (^{16}\text{O}, p3n)^{82}\text{Y}$. Evidence that ^{82}Y is produced in the $^{70}\text{Ge} + ^{16}\text{O}$ reaction is found in the gates set on the annihilation radiation peak (511. keV). There one can observe the decay products from ^{82}Y (53,54). One of the particularly strong band structures is shown in Figure 4-26. Further investigation of the identity of this nucleus can be made with neutron-gamma coincidence measurements and a velocity filter for isotope identification.

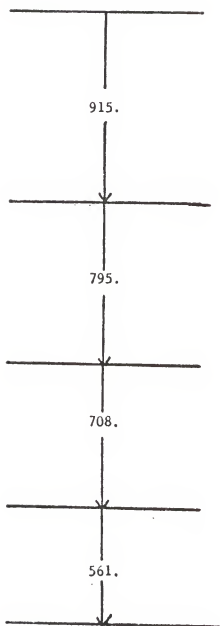


Figure 4-26. Band structure in an unidentified nucleus.

CHAPTER 5 SUMMARY

In-beam gamma-ray spectroscopy techniques have been used in a study of the nucleus ^{82}Sr . Experiments were performed on the Florida State University FN Tandem Van de Graaff accelerator. The reaction used was $^{70}\text{Ge}(^{16}\text{O}, 2p2n)^{82}\text{Sr}$ with an oxygen beam energy of 80 MeV. Excitation functions were used to select a beam energy which maximized the cross section for the production of ^{82}Sr . The energy levels were established with γ - γ -t coincidence measurements and the angular distribution and polarization data were used to assign spins and parities to the levels.

Much new information has been contributed about ^{82}Sr . Six new levels have been placed in the level scheme at 2683.7, 3609.0, 4367.5, 5308.7, 6364.8, and 7827.8 keV. A possible new band has been identified with a bandhead at 3526.3 keV. Seventeen gamma rays that were previously unplaced have been associated with transitions in this nucleus. The transitions in the negative parity band have been reordered to 694-876-1005-522 keV. The new ordering is supported by quasiparticle-plus-rotor calculations (58), the large attenuation coefficient of the highest member of the sequence, and systematics. Polarization measurements used to assign parities to the levels also yielded information about mixing ratios and attenuation coefficients; in some cases they helped resolve ambiguous spin assignments as well.

The experimental data on ^{82}Sr have been compared with several nuclear models. The complexity of its level scheme implies that this is a transitional nucleus. The level spacings for $I < 4^+$ are

characteristic of those expected in a vibrational nucleus. However, in the ground state band, the increasing level spacing with spin suggests rotational behavior. Application of the variable moment of inertia model to the ground state band indicates that the moment of inertia changes with spin and therefore the structure can be assumed to change with spin. Thus the nucleus can be considered soft, i.e., it changes shape with spin.

The presence of a second excited 2^+ state below the first excited 4^+ state is an indication that this nucleus is not axially symmetric (45-46). One can say that ^{82}Sr is a gamma-soft nucleus or that it is a triaxial rotor, both terms referring to a tendency towards deformation with respect to the γ degree of freedom (away from axial symmetry), the first being a dynamic condition, the second a static condition.

The large transition probabilities connecting the lower ($I < 8$) spin states and transition energies which are lower than those expected for single particle transitions are indications of collective behavior. The ground state band and first excited positive parity bands up to spin 8^+ are both examples of collective excitations of the ground state configuration. A collective model such as the IBM fits these levels well. Above that spin, noncollective or intrinsic excitations begin to influence the structure.

These intrinsic quasiparticle excitations have rotational bands built upon them. There are three such bands identified so far in this nucleus. One is a positive parity band, one is a negative parity band and one is, so far, of unknown parity. Two-quasiparticle-plus-rotor calculations have suggested that the negative parity band is based on a ($g_{9/2}, f_{5/2}$) two-quasiproton configuration (58). The positive parity

quasiparticle band is assumed to be a two- $g_{9/2}$ -quasiproton configuration (5). The character of the third quasiparticle band is not yet known.

If one were choosing a nucleus to study, ^{82}Sr would not appear very interesting at first glance. The ground state band exhibits no backbending; there are the "standard" positive parity and negative parity side-bands. However, it is just these side bands that make this an intriguing nucleus to study. The positive parity band exhibits behavior that can be interpreted as a vibrational excitation which makes an abrupt change to a rotational excitation. The usual moment of inertia graph indicates that the nucleus may suddenly become a rigid rotor above $I = 10^+$. An alternative explanation involves the crossing of the quasigamma band by a two-quasiparticle band. If this alternative be the correct one, the interaction between the quasigamma band and the quasiparticle band will be the strongest such interaction known in this area of the nuclear chart.

The negative parity band is fed by a transition that has a high degree of anisotropy. The polarization and angular distribution data imply that it is an $E2/M1$ transition with a mixing ratio of $-.53(37)$. The experimental attenuation coefficient is $.97(07)$. This implies that the (12^-) state at 5914.8 keV may be fed directly from the continuum, unusual since transitions from states of higher spin $(13, 14^+)$ do not appear to have such large attenuation coefficients.

This transitional nucleus, ^{82}Sr , exhibits behavior that indicates that there is an interplay of several degrees of freedom such as collective rotational and vibrational excitations, single-particle excitations, and core deformations. This interplay results in a complex level scheme. Further microscopic calculations can relate the

experimental data to theoretical concepts. More precise transition probabilities $[(B(E\lambda)'s)]$ are needed to understand the collective aspects of the structure. Polarization measurements with better resolution can clear up some remaining uncertainties about parity assignments.

In terms of systematics, the data contained in the present work contribute to the understanding of the change in structure as particles are added to, or removed from, the valence shell. In particular, the neutron-deficient strontium isotopes appear to evolve from spherical to highly deformed as neutrons are removed. Because ^{82}Sr is located in the center of this evolution, understanding its behavior can lead to an understanding of how and why the evolution occurs.

BIBLIOGRAPHY

1. R. M. Diamond and F. S. Stephens, *Ann. Rev. Nucl. Part. Sci.* 30, 85 (1980).
2. F. S. Stephens and R. S. Simon, *Nucl. Phys.* A183, 257 (1972).
3. M. Sakai, Quasi-Bands (Institute for Nuclear Study, Tokyo, 1982).
4. C. J. Lister, B. J. Varley, H. G. Price, and J. W. Olness, *Phys. Rev. Lett.* 49, 308 (1982).
5. L. Funke, J. Doring, S. Frauendorf, P. Kemnitz, F. R. May, E. Will, and G. Winter, *Phys. Lett.* 108B, 243, (1982).
6. H. G. Price, C. J. Lister, B. J. Varley, W. Gelletly, and J. W. Olness, *Phys. Rev. Lett.* 51, 1842, (1983).
7. A. C. Rester, private communication, 1982.
8. W. Lourens, Delft University of Technology (unpublished), 1980.
9. J. D. Cole, Delft University of Technology (unpublished), 1980.
10. H. Morinaga and T. Yamazaki, In-Beam Gamma-Ray Spectroscopy (North-Holland, New York, 1976).
11. T. Yamazaki, *Nucl. Data* A3, 1 (1967).
12. R. W. Smart, M.S. Thesis, University of Florida, 1983.
13. O. Klein and Y. Nishina, *Z. Phys.* 52, 853 (1929).
14. L. W. Fagg and S. S. Hanna, *Rev. Mod. Phys.* 31, 711 (1959).
15. K. S. Krane and R. M. Steffen, *Phys. Rev. C* 2, 724 (1970).
16. D. C. Stromswald, Ph.D. Dissertation, Johns Hopkins University, 1976.
17. J. B. Ball, J. J. Pinajian, J. S. Larsen, and A. C. Rester, *Phys. Rev. C* 8, 1438 (1973).
18. C. A. Fields, F. W. N. de Boer, E. Sugarbaker, and P. M. Walker, *Nucl. Phys.* A363, 352 (1981).
19. T. Higo, S. Matsuki, and T. Yanabu, *Nucl. Phys.* A393, 224 (1983)..

20. A. Dewald, Ph.D. Dissertation, University of Cologne, 1982.
21. R. L. Coldwell, J. Quant. Spectrosc. Radiat. Transfer (in press).
22. A. C. Rester, Ph.D. Dissertation, Vanderbilt University, 1969.
23. R. L. Coldwell, private communication, 1980.
24. K. Kumar and M. Baranger, Nucl. Phys. A92, 608 (1967).
25. M. Goeppert-Mayer and J. H. D. Jensen, in Alpha, Beta, and Gamma-Ray Spectroscopy, edited by Kai Siegbahn (North-Holland, Amsterdam, 1965), Vol. 1.
26. A. Bohr and B. R. Mottelson, Nuclear Structure (W. A. Benjamin, Inc., New York, 1969), Vol. 2.
27. D. Bucurescu, G. Cata, D. Cutoiu, G. Constantinescu, M. Ivascu, and N. V. Zamfir, Nucl. Phys. A401, 22 (1983).
28. K. Heyde, J. Moreau, and M. Waroquier, Phys. Rev. C 29, 1859 (1984).
29. C. Flaum and D. Cline, Phys. Rev. C 14, 1224 (1976).
30. M. A. J. Mariscotti, G. Scharff-Goldhaber, and B. Buck, Phys. Rev. 178, 178 (1969).
31. S. G. Nilsson, Dan. Mat. Fys. Medd. 29, 1 (1955).
32. R. Bengtsson and S. Frauendorf, Nucl. Phys. A314, 27 (1979); Nucl. Phys. A327, 139 (1979).
33. L. Funke, J. Doring, F. Dubbers, P. Kemnitz, E. Will, G. Winter, V. G. Kiptilij, M. F. Kudojarov, I. Kh. Lemberg, A. A. Pasternak, A. S. Mishin, L. Hildingsson, A. Johnson and Th. Lindblad, Nucl. Phys. A355, 228 (1981).
34. J. E. Kitching, W. G. Davies, W. J. Darcey, W. McLatchie, and J. Morton, Nucl. Phys. A177, 433 (1971).
35. K. Ogawa, Phys. Lett. 45B 214 (1973).
36. W. P. Alford, R. E. Anderson, P. A. Batay-Csorba, R. A. Emigh, D. A. Lind, P. A. Smith and C. D. Zafiratos, Nucl. Phys. A330, 77 (1979).
37. J. M. Eisenberg and W. Greiner, Nuclear Models (North-Holland, Amsterdam, 1970).
38. J. P. Davidson, Rev. Mod. Phys. 37, 105 (1965).
39. M. E. Rose, Elementary Theory of Angular Momentum (John Wiley, New York, 1957).

40. M. A. Preston and R. K. Bhaduri, Structure of the Nucleus (Addison-Wesley, Reading, Mass., 1975).
41. B. Mottelson, Proceedings of the Rehoveth Conference on Nuclear Structure, edited by H. J. Lipkin (North Holland, Amsterdam, 1958).
42. D. R. Inglis, Phys. Rev. 96, 1059 (1954).
43. S. M. Harris, Phys. Rev. Lett. 13, 663 (1964).
44. D. Bonatsos and A. Klein, At. Data Nucl. Data Tables 30, 27 (1984).
45. A. S. Davydov and G. F. Filippov, Nucl. Phys. 8, 237 (1958).
46. A. S. Davydov and A. A. Chaban, Nucl. Phys. 20, 499 (1960).
47. A. Arima and F. Iachello, Phys. Rev. Lett. 35, 1069 (1975).
48. A. Arima and F. Iachello, Ann. Rev. Nucl. Part. Sci. 31, 75 (1981).
49. E. Majorana, Z. Phys. 82, 137 (1933).
50. A. Faessler, Rep. Prog. Phys. 45, 653 (1982).
51. B. R. Mottelson and J. G. Valatin, Phys. Rev. Letters 5, 511 (1960).
52. J. Bardeen, L. N. Cooper, and J. R. Schrieffer, Phys. Rev. 108, 1175 (1957).
53. C. J. Lister, P. E. Hausstein, D. E. Alburger, and J. W. Olness, Phys. Rev. C 24, 260 (1981).
54. S. Della Negra, H. Gauvin, D. Jacquet, and Y. Le Beyec, Z. Phys. A 307, 305 (1982).
55. D. L. Sastry, A. Ahmed, A. V. Ramayya, R. B. Piercey, H. Kawakami, R. Soundranayagam, J. H. Hamilton, C. F. Maguire, A. P. de Lima, S. Ramavataram, R. L. Robinson, H. J. Kim, and J. C. Wells, Phys Rev. C 23, 2086 (1981).
56. S. Matsuki, K. Ogina, Y. Kadota, N. Sakamoto, T. Tanabe, M. Yasue, A. Yokomizo, S. Kobono, and Y. Okuma, Phys. Letts. 113B, 21 (1982).
57. T. Matsuzaki and H. Taketani, Nucl. Phys. A390, 413 (1982).
58. R. Soundranayagam, private communication, 1984.
59. WAVEFN.FOR, written by C. Flaum and D. Elmore and modified by R. Soundranayagam, Vanderbilt University Physics Computer Library.
60. COREMX.FOR, C. Flaum and D. Elmore, modified by R. Soundranayagam, Vanderbilt University Physics Computer Library.

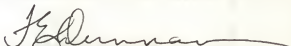
61. R. Lecomte, M. Irshad, S. Landsberger, G. Kajrys, P. Paradis, and S. Monaro, Phys. Rev. C 22, 2420 (1980).
62. J. H. Hamilton, A. V. Ramayya, C. F. Maguire, R. B. Piercey, R. Bengtsson, P. Möller, J. R. Nix, J.-Y. Zhang, R. L. Robinson, S. Frauendorf, J. Phys. G 10, L87 (1984).
63. A. Dewald, U. Kaup, W. Gast, A. Gelberg, H.-W. Schuh, K. O. Zell, and P. von Brentano, Phys. Rev. C 25, 226 (1982).
64. S. E. Arnell, A. Nilsson, and O. Stankiewicz, Nucl. Phys. A241, 109 (1975).
65. G. Scharff-Goldhaber, C. B. Dover, and A. L. Goodman, Ann. Rev. Nucl. Sci. 26, 1 (1976).
66. J. Ginocchio and M. W. Kirson, Nucl. Phys. A350, 31 (1980).

BIOGRAPHICAL SKETCH

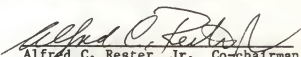
I was born in Macon, Georgia in 1944. My father was a pilot in the Air Force so I spent most of my youth moving from place to place. I attended ten different schools in my first twelve years of schooling, finally graduating from Greenville Senior High School, Greenville, South Carolina, in 1962. I attended the University of Florida for three trimesters and transferred to North Carolina State University where I received a B.S. degree in applied mathematics in January 1967. I minored in physics, taking three courses in nuclear physics. I had decided that the first chance I got I would return to school for an advanced degree in physics. That chance came when we moved to Gainesville, Florida in the fall of 1976. I enrolled in graduate school at the University of Florida in January, 1977.

I have been married to Bernard R. Haskins for over twenty-one years. We have two daughters, Jennifer, aged 20, and Stephanie, aged 17.

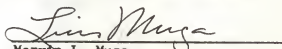
I certify that I have read this study and that in my opinion it conforms to acceptable standards of scholarly presentation and is fully adequate, in scope and quality, as a dissertation for the degree of Doctor of Philosophy.


Francis E. Dunnam, Chairman
Professor of Physics and Astronomy

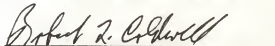
I certify that I have read this study and that in my opinion it conforms to acceptable standards of scholarly presentation and is fully adequate, in scope and quality, as a dissertation for the degree of Doctor of Philosophy.


Alfred C. Rester, Jr., Co-chairman
Associate Professor of Astronomy

I certify that I have read this study and that in my opinion it conforms to acceptable standards of scholarly presentation and is fully adequate, in scope and quality, as a dissertation for the degree of Doctor of Philosophy.


Marvin L. Muga
Professor of Chemistry

I certify that I have read this study and that in my opinion it conforms to acceptable standards of scholarly presentation and is fully adequate, in scope and quality, as a dissertation for the degree of Doctor of Philosophy.


Robert L. Coldwell
Assistant Professor of
Physics

This dissertation was submitted to the Graduate Faculty of the Department of Physics in the College of Liberal Arts and Sciences and to the Graduate School, and was accepted as partial fulfillment of the requirements for the degree of Doctor of Philosophy.

December 1984

Dean for Graduate Studies
and Research